Hybrid Josephson junction-based quantum devices in magnetic field

Uilhoorn, W.

DOI
10.4233/uuid:dd3c8524-413c-405b-98f2-9dba974965db

Publication date
2021

Document Version
Final published version

Citation (APA)
Uilhoorn, W. (2021). *Hybrid Josephson junction-based quantum devices in magnetic field*. [Dissertation (TU Delft), Delft University of Technology]. https://doi.org/10.4233/uuid:dd3c8524-413c-405b-98f2-9dba974965db

Hybrid Josephson junction-based quantum devices in magnetic field

Hybrid Josephson junction-based quantum devices in magnetic field

Proefschrift

ter verkrijging van de graad van doctor
aan de Technische Universiteit Delft,
op gezag van de Rector Magnificus Prof.dr.ir. T.H.J.J. van der Hagen,
voorzitter van het College voor Promoties,
in het openbaar te verdedigen op vrijdag 28 mei 2021 om 15:00 uur

door

Willemijntje Uilhoorn

Natuurkundig ingenieur, Technische Universiteit Delft, Nederland,
geboren te Naarden, Nederland.

Dit proefschrift is goedgekeurd door de promotoren.

Samenstelling promotiecommissie:

Rector Magnificus,	voorzitter
Prof.dr.ir. L.P. Kouwenhoven	Technische Universiteit Delft, promotor
Prof.dr. L. DiCarlo	Technische Universiteit Delft, promotor
Onafhankelijke leden:	
Prof.dr. G.A. Steele	Technische Universiteit Delft
Prof.dr. A.F. Otte	Technische Universiteit Delft
Prof.dr.ir. T.H. Oosterkamp	Universiteit Leiden
Prof.dr. F. Hassler	RWTH Aachen University, Duitsland
Overige leden:	
Dr. M.C. Cassidy	Microsoft Quantum Sydney, Australië

Printed by: Gildeprint

Front & Back: Artistic impression of a device architecture studied in this thesis.

ISBN 978-90-8593-477-6

An electronic version of this dissertation is available at
`http://repository.tudelft.nl/`.

Contents

Summary

The technology of quantum computing is believed to solve certain computational problems significantly faster than classical computers, enabling classically inaccessible problems. However, the technology is still in its infancy and it is still too early to conclude which physical system(s) will form the basis of tomorrow's quantum computer. Small-scale quantum processors, built on the superconducting transmon qubit, demonstrated already the anticipated quantum speed-up. Despite this tremendous milestone, scaling up to a full-fledged quantum computer is far from trivial: with these qubits, the flux-control causes crosstalk between qubits and heating, the room-temperature microwave control is hardly scalable and comes with high energetic radiation, and most importantly, the loss of quantum information in time leads to computational errors.

Recent advances in various hybrid semiconductor materials enabled novel voltage-controlled transmons, gatemons, which are less susceptible to heating and crosstalk. Even more exciting, gatemons can be designed to host Majorana zero modes in a way that renders the qubit inherently protected against decoherence. In order to induce Majorana zero modes in such nanowire systems strong magnetic fields are required. Problematically, magnetic fields destroy the superconductivity that these microwave circuits rely on.

In this thesis we integrate three types of hybrid Josephson junctions in magnetic field compatible microwave devices. Chapter 4 demonstrates the first graphene-based transmon. Due to the mono-atomic thickness of graphene in combination with magnetic field resilient coplanar waveguide resonators, we are able to operate the transmon circuit at an in-plane magnetic field of 1 T. Chapter 5 embeds an InAs-Al semiconducting nanowire Josephson junction in a high quality factor superconducting transmission line resonator, demonstrating on-chip microwave generation. The gate-controllable semiconducting platform lends itself for fast pulse control, providing a perspective for the coherent on-chip manipulation of artificial two-level systems, in particular superconducting qubits such as transmons. Chapter 6 continues the development of InAs-Al nanowire transmons. The offset-charge-sensitive regime, additional plunger gates and magnetic field compatibility prepares the platform for the detection of coherent coupling between Majorana zero modes, a phenomena which unfortunately still remains unobserved. Additionally, we realise the first InSb-Al gatemon. The higher spin-orbit coupling makes InSb to be a preferred material in the search for Majorana signatures. Chapter 7 reports on the dynamics of quasiparticle tunneling events in real-time across the InAs-Al nanowire junction in a transmon architecture. The magnetic field compatibility of our device up to 1 T together with in-situ voltage-controlled quasiparticle trap engineering, allows us to measure the survival of the charge-parity lifetime up to strong magnetic fields. A result which is extremely important in the research field of topological quantum computing, where the qubit space is defined in the charge-parity.

Samenvatting

De kwantumcomputertechnologie belooft bepaalde berekeningen te kunnen oplossen die buiten het bereik liggen van klassieke computers. Deze kwantumtechnologie staat echter nog in de kinderschoenen, en het is nog te vroeg om te concluderen welk fysiek systeem de basis zal vormen van de kwantumcomputer van morgen. Kleinschalige kwantumprocessors, gebouwd op supergeleidende transmon-qubits, toonden al de voorspelde kwantumversnelling. Ondanks deze enorme mijlpaal is de opschaling naar een volwaardige kwantumcomputer verre van triviaal: de fluxregeling veroorzaakt ongewenste koppeling tussen qubits en warmte, de microgolfregeling op kamertemperatuur is moeilijk schaalbaar en komt gepaard met hoogenergetische straling, bovendien, het verlies van kwantuminformatie met het verloop van de tijd leidt tot rekenfouten.

Recente vooruitgang in hybride halfgeleidermaterialen hebben spanningsgestuurde transmons, gatemons, mogelijk gemaakt. Deze zijn minder gevoelig voor parasitaire koppeling en geven minder warmte af. Bovendien kunnen gatemons ontworpen worden om Majorana toestanden te huizen, zodanig dat de qubit inherent beschermd is tegen decoherentie. Echter, het is problematisch dat de sterke magnetische velden, die nodig zijn om Majorana toestanden in dergelijke nanodraadsystemen te induceren, afbreuk doen aan de supergeleiding waarop deze microgolfcircuits werken.

In dit proefschrift integreren we hybride Josephson juncties in microgolfcircuits, om zodanig microgolfsystemen te vervaardigen die operationeel zijn in magnetische velden. Hoofdstuk 4 demonstreert de eerste op grafeen gebaseerde transmon. Vanwege de mono-atomaire dikte van grafeen en de magnetisch veld compatibele coplanaire golfgeleiderresonatoren, zijn we in staat om het transmoncircuit te laten werken in een magnetisch veld van 1 T. Hoofdstuk 5 integreert een InAs-Al nanodraad met Josephson junctie in een hoogwaardige supergeleidende transmissielijnresonator, waarmee on-chip coherente microgolfgeneratie wordt aangetoond. Het elektrisch aanstuurbare halfgeleiderplatform leent zich bij uitstek voor snelle pulsbesturing en biedt perspectief voor de coherente on-chip manipulatie van qubits, in het bijzonder supergeleidende qubits. Hoofdstuk 6 gaat in op de doorontwikkeling van InAs-Al nanodraadtransmons. De besturing in het ladingsgevoelige regime, extra electrodes en compatibiliteit met magnetische velden bereidt het platform voor op de detectie van Majorana toestanden, een fenomeen dat helaas nog steeds niet is waargenomen. Daarnaast realiseren we de eerste InSb-Al gatemon. Door de hogere spin-baan-koppeling wordt de voorkeur gegeven aan InSb als halfgeleider in de zoektocht naar Majorana toestanden. Hoofdstuk 7 rapporteert over de dynamiek van het tunnelen van energetische excitaties door de InAs-Al nanodraad-junctie in een transmonarchitectuur. De compatibiliteit met magnetische velden tot en met 1 T stelt ons in staat de tijdschaal van dit tunnelingsfenomeen te meten in sterke magnetische velden. Wij laten zien dit tunnelen te kunnen bedwingen met in-situ veldgestuurde vallen. Een resultaat dat van uiterst belang is op het gebied van de topologische qubit, waar de qubitruimte wordt gebroken door tunnelingen.

1

Introduction

It always seems impossible until it's done.

Nelson Mandela

1.1. The era of Computing

In our modern age electronic devices have become indispensable. The growing demand for personal electronics is a tangible example of how we have come to rely on computers, and portrays the continuously increasing demand of computing power whilst simultaneously demanding smaller devices. Less obvious are the many ways in which our everyday life is affected by high performance computing, made possible by supercomputers. For example, supercomputers allow us to design and simulate new drugs, control epidemics, design more aerodynamic and safer cars and airplanes and forecast the weather more accurately and earlier in advance. Even though supercomputers enabled many technological advances, many simulations are still out of reach or require (over)simplifications to be solved in a reasonable amount of time. To access these simulations more computing power is required.

Increasing computational power is achieved by increasing the number of electronic elements that carry out the computation together. In the current computers this electronic building block is a transistor, which can be combined to form a logic gate. The absence or presence of a current through the transistors and with that through the logic gate encodes a binary digit, called bit. In the absence of a current the state of the bit is said to take the value ″0″, and the value ″1″ when a current is conducted. The increase in computing power when the number of transistors is increased depends on the specific computational problem, the algorithm used and the overhead time linked to the interconnections of the bits. Generally it can be approximated by a linear trend; meaning that in order to double the computational power the number of bits also need to be doubled.

Over time the miniaturization of transistors played an essential role in managing the supercomputer's footprint in this upscaling process.

1.2. The battle of computers

The approach of miniaturization has a physical limit, as the laws of classical mechanics do not apply at the microscopic level. Here quantum mechanics takes over instead. A new form of computing was proposed based on the principles of quantum mechanics: quantum computing [1, 2] built out of so-called quantum bits (qubits). Qubits can be encoded in systems as small as single particles. But the actual strength of quantum computing comes from the superior non-linear scaling of the computational power upon increasing the number of qubits. This speed-up of computational power predicts a *quantum speed-up* for problems such as optimization problems, searching through large data sets and integer factorisation. Which promises great advances over a wide range of fields including encryption and cybersecurity, financial models, supply chain logistics, data categorization and chemical simulations.

To showcase the promise of quantum computing, we consider the well-defined problem of integer factorisation[1]. The problem underlies the current encryption method to secure data transmission. It is one of the most challenging computations in the history of conventional computer science. However, the designed quantum algorithm for this problem, Shor's algorithm, is predicted to be very efficient. The supremacy of quantum computing can be expressed in the estimated computational time required to factor an n-bit number [3]. Figure 1.1 illustrates that the development of conventional supercomputers progresses very slowly over years in comparison to the speed-up that a quantum algorithm promises. Ultimately, classic computing is constraint by the steep increase in computation time for large bit numbers, as shown by the extrapolated curves from records set in 2003 [4] and 2019 [5] . The current records require computation times on the order of months, but could be accomplished in mere seconds on a quantum computer. Because of this scaling quantum computers are believed to be able to quickly solve certain problems that no classical computer could solve in any feasible amount of time, a threshold called *quantum supremacy*. It should be noted that quantum supremacy does not require any useful task and is subject to a sliding baseline as classical computing algorithms continue to develop over time. Because of this, quantum supremacy holds no immediate bearing for the viability of useful, large-scale quantum computing, but is still recognised as an important proof of concept to which the first claims have been done [6, 7].

---

[1] Integer factorisation is the decomposition of a number into the product of several integer prime numbers. For example, 3 × 5 is the factorisation of 15.

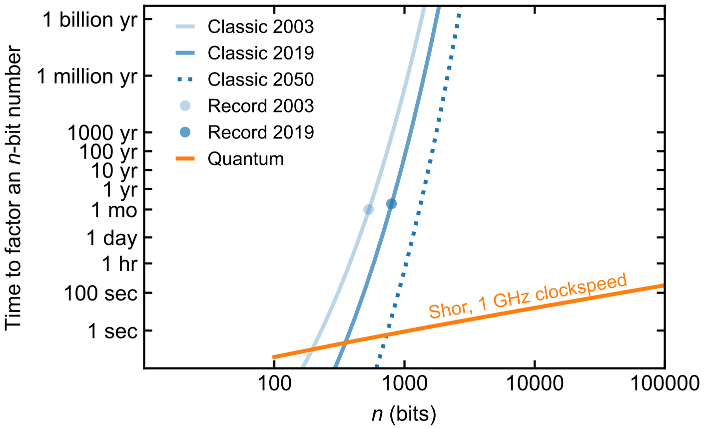

Figure 1.1: **Quantum speed-up** Comparison of the predicted time required to crack n-bit number factorisation, the principle behind current data encryption methods. The orange line shows the predicted computation time for a quantum computer, while the blue curves show the extrapolated classical computation times based on records. The dotted blue curve shows the predicted ability of classical computers in 2050, according to Moore's law. The classical speed-up over the years shown by the progression of the blue curves is insignificant in comparison to the quantum speed-up. Graph based on [3].

1.3. Quantum computing

A quantum computer finds its advantage through the quantum mechanical properties of superposition and entanglement. Where a classical bit is a true binary digit that can take on the value ”0” or ”1”, as depicted in Figure 1.2a on the left in blue, a qubit can be in a superposition of two states, as represented by the spherical surface on the right in orange. Even though the state space is continuous, it has a remarkable different meaning than a continuous scale between 0 and 1 in the classical sense. A classical binary system like a light bulb can either be off (”0”) or on (”1”). In the case of a continuous classical scale one could image the light bulb's light intensity to be adjustable via a dimmer. However, in the quantum mechanical picture the continuous scale indicates the light bulb is simultaneously on and off, each with their own probabilities. A phenomenon that we don't find an analogue for in classical mechanics, and one of the powers of quantum mechanics. The second quantum mechanical principle that is crucial in quantum computing is the entanglement of the states of different qubits. Via entangling the qubits are not individual states but act as an inseparable whole. This means that all the qubits collapse onto a particular state simultaneously and dependently of the other, enabling quantum computations. It is through the superposition of each qubit and the entanglement of different qubits that a quantum computer can speed up its search for a given task, as it can simultaneously verify all permutations of a certain computation. Figure 1.2b illustrates this difference between classical and quantum computing, where in the quantum case the entangled system collapses probabilistically onto the solution. Statistics will reveal the most probable outcome; the solution to the problem. In this way, entangling one additional qubit will double the computational space that can be checked simultaneously.

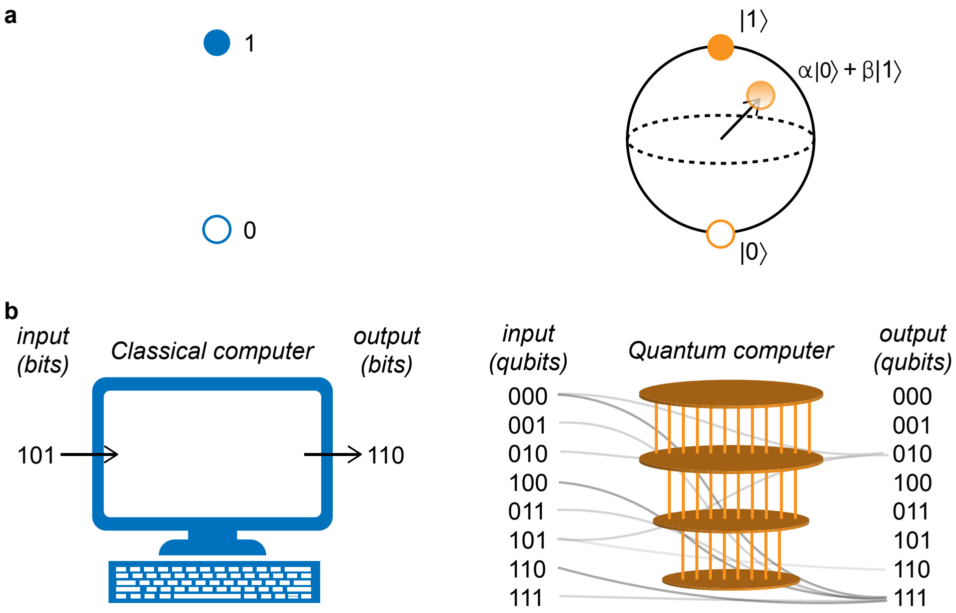

Figure 1.2: **Conventional versus quantum computing a** A conventional bit (left) can either take on the value "0" or "1". On the contrary, a quantum bit (right) can take any superposition of the two states, as depicted by the surface of a sphere, called the Bloch sphere. **b** A classical computer computes (blue, left) in a deterministic fashion, where it needs to iterate over the inputs to find the desired outcome. Contrarily, a quantum computer (orange, right) will be able to explore the entire computational input space at once, after which it probabilistically collapses onto an output. Statistics will then reveal the outcome that is searched for.

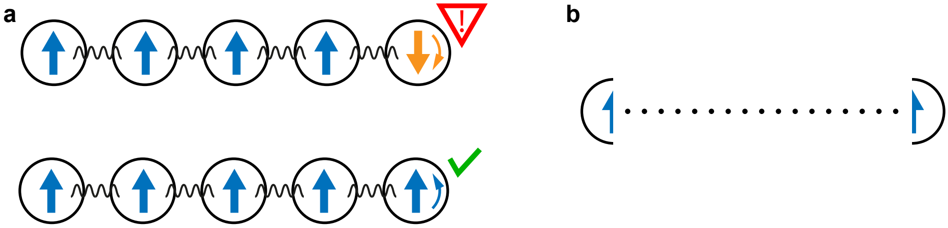

Figure 1.3: **Battling quantum errors.** **a** Quantum error correction schemes use a collection of qubits to preserve the quantum state longer. In this way decoherence can be detected and corrected. **b** Topological quantum computing protects the quantum state from decohering by storing the quantum information non-local in comparison to the perturbations from the environment.

The principles of quantum computing rely on the most fundamental properties of quantum mechanics, and hence qubits can be formed in every branch; atomic physics, quantum optics, nuclear and electron magnetic resonance spectroscopy, superconducting electronics, quantum-dot physics, and condensed matter physics. Each platform has its individual benefits and disadvantages. The most common and important challenge being the timescale over which a quantum state can be stored, called the coherence time. Generally the quantum state of a qubit is lost over time through unwanted coupling to its noisy and uncontrolled environment. When qubits lose their quantum state during a calculation quantum errors can occur, making the calculation unreliable. So in a perfect situation, a qubit is completely isolated from its environment, while it is quickly addressable at the same time for computations with other qubits. These two opposing requirements need to be optimized. A popular solution to this optimization problem is to add qubits which have the sole purpose to preserve the qubits quantum state by correcting each others decoherence. The working principle of such error correction mechanisms lies in the distribution of the to quantum state over multiple entangled qubits. As illustrated in Figure 1.3a, in this way the decoherence of one of the qubits can be detected and corrected. In this error correction scheme the additional qubits only reduce the error rates, and do not aid in increasing the overall computing power.

1.4. Topological quantum computing

A different approach to battle the decoherence of the quantum state is to design a qubit that is inherently protected against coupling environmental noise sources. This inherent protection is highly unusual, but predicted to be achievable in a collective state of many electrons. Under specific conditions the collective state can be described mathematically as two particle-like states, *quasiparticles*, residing at opposing boundaries of the material. These quasiparticles are equal superpositions of half an electron and half a hole, making them their own antiparticles. Because of this they are called Majorana quasiparticles, named after the class of elementary fermionic particles that are their own antiparticles. Figure 1.3b illustrates the spatial separation of the storage of the quantum information. In this way, both Majorana quasiparticles experience different perturbations from the environment. However, the collective origin of the quasiparticles prevents them to decohere. This mechanism that allows the storage of quantum information over a very long

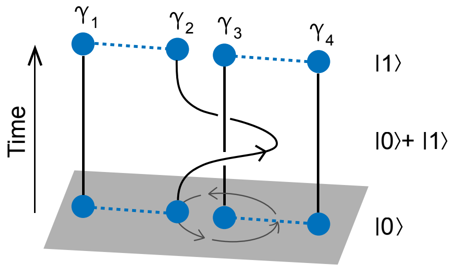

Figure 1.4: **A topological qubit** encodes its state in the braiding history of Majoranas of different pairs. A Majorana qubit at least has to consist of four Majoranas to be able to exchange an electron between the two many-body systems.

time is called topological protection. Majorana quasiparticles can be utilized as qubits, where the qubit's state is defined in the superposition of the electron state ("1") and hole state ("0"). Quantum computing based on such Majorana qubits is called topological quantum computing. Due to the exotic exchange statistics the electron-hole superposition can be manipulated when spatially moving Majorana quasiparticles around each other that belong to different Majorana pairs. In this manner electrons can be exchanged between the different many-body systems. A Majorana qubit therefore consists at least of four Majoranas, as depicted in Figure 1.4. This process of encoding the quantum state is called braiding, as the memory of the exchanges can be visualised by the braiding of strings. To collapse the quantum superposition onto a measurement outcome is done by fusing the Majoranas after the braid, either resulting in an electron or vacuum.

Most, unfortunately not all, logic gate operations are possible without the need to fuse Majorana's, making also the logic gate operations topologically protected. This inherent protection against quantum information loss is the great promise of topological quantum computing, even though the field is less developed with respect to other qubit platforms.

1.5. Hybrid quantum devices in magnetic field

Among the most promising platforms for engineering Majoranas are those based on semiconductor-superconductor nanowires in the presence of strong magnetic fields. Measurements showing features that are in agreement with Majoranas in such nanowires are mounting [8–18]. However, additional evidence is still needed to unambiguously show the existence of such engineered excitations.

In this thesis we develop microwave quantum circuit devices based on hybrid Josephson junctions that are able to operate in strong magnetic fields. With this research we aim to probe the fundamental physics of semiconductor Josephson junctions at high-bandwidth and to develop magnetic field resilient microwave technologies in order to study previously unexplored magnetic field performance of superconducting devices. These technological advances pave the way for novel high-bandwidth Majorana signatures and possible future Majorana qubit architectures. More generally, these advances can also find purpose in the development magnetic-field-compatible and voltage-tunable cavities, qubits and quantum-limited parametric amplifiers. Here the gate-tunability can help in mitigating problems such as on-chip heating, crosstalk and fast-control in superconducting circuits where SQUIDs are used as tuning elements. Furthermore, magnetic-field compatibility relieves the requirements for expensive magnetic field shielding of the devices, and opens up applications based on magnetic field induced phenomena such as spin ensembles through magnetic field polarization.

Chapter 2 provides a brief overview of some theoretical concepts that underlie the working principles of the quantum devices in this thesis. **Chapter** 3 details some unconventional fabrication techniques and setup specifications that are crucial to the measurement of the devices. **Chapter** 4 describes the first integration of graphene Josephson junctions into a microwave frequency superconducting circuit to create a graphene transmon. This platform showcases the magnetic field compatibility of hybrid Josephson junctions at magnetic fields strong enough for topological superconducting qubits. **Chapter** 5 integrates a semiconducting nanowire in high quality factor superconducting resonators, and demonstrates on-chip generation of coherent microwave radiation. The semiconductor platform allows for fast voltage control to generate pulses that could find a broad application in quantum computing schemes. **Chapter** 6 demonstrates the fabrication and measurements of magnetic field compatible semiconductor nanowire transmons, both based on InAs and InSb. Materials in which signatures of Majorana modes have been observed at magnetic field values that are accessible in our transmons. **Chapter** 7 investigates the quasiparticle poisoning evolution in magnetic fields high enough for Majorana physics at high bandwidth. The device demonstrates the importance of engineered quasiparticle traps to mitigate this disastrous phenomenon. Finally **Chapter** 8 suggests possible future research directions building up upon the findings of this thesis.

References

[1] Manin, Y. I. *Computable and Uncomputable (in Russian)* (Sov.Radio., 1980).

[2] Feynman, R. P. Simulating physics with computers. *International Journal of Theoretical Physics* **21**, 467–488 (1982).

[3] van Meter, R., Itoh, K. M. & Ladd, T. D. Architecture-dependent execution time of shor's algorithm. In *MS+S 2006 Controllable Quantum States*, 183–188 (World Scientific Publishing Cp. Pte Ltd, 2008).

[4] Franke, J. *et al.* Rsa576. URL `https://members.loria.fr/PZimmermann/records/rsa576`.

[5] Boudot, F. *et al.* Comparing the difficulty of factorization and discrete logarithm: A 240-digit experiment. In Micciancio, D. & Ristenpart, T. (eds.) *Advances in Cryptology – CRYPTO 2020*, 62–91 (Springer International Publishing, 2020).

[6] Arute, F. *et al.* Quantum supremacy using a programmable superconducting processor. *Nature* **574**, 505–510 (2019).

[7] Zhong, H.-S. *et al.* Quantum computational advantage using photons. *Science* **370**, 1460–1463 (2020).

[8] Mourik, V. *et al.* Signatures of Majorana Fermions in Hybrid Superconductor-Semiconductor Nanowire Devices. *Science* **336**, 1003–1007 (2012).

[9] Rokhinson, L. P., Liu, X. & Furdyna, J. K. The fractional a.c. Josephson effect in a semiconductor–superconductor nanowire as a signature of Majorana particles. *Nature Physics* **8**, 795–799 (2012).

[10] Deng, M. T. *et al.* Anomalous Zero-Bias Conductance Peak in a Nb–InSb Nanowire–Nb Hybrid Device. *Nano Letters* **12**, 6414–6419 (2012).

[11] Das, A. *et al.* Zero-bias peaks and splitting in an Al–InAs nanowire topological superconductor as a signature of Majorana fermions. *Nature Physics* **8**, 887–895 (2012).

[12] Churchill, H. O. H. *et al.* Superconductor-nanowire devices from tunneling to the multichannel regime: Zero-bias oscillations and magnetoconductance crossover. *Phys. Rev. B* **87**, 241401 (2013).

[13] Finck, A. D. K., Van Harlingen, D. J., Mohseni, P. K., Jung, K. & Li, X. Anomalous Modulation of a Zero-Bias Peak in a Hybrid Nanowire-Superconductor Device. *Phys. Rev. Lett.* **110**, 126406 (2013).

[14] Albrecht, S. M. *et al.* Exponential protection of zero modes in Majorana islands. *Nature* **531**, 206–209 (2016).

[15] Deng, M. T. *et al.* Majorana bound state in a coupled quantum-dot hybrid-nanowire system. *Science* **354**, 1557–1562 (2016).

[16] Chen, J. *et al.* Experimental phase diagram of zero-bias conductance peaks in superconductor/semiconductor nanowire devices. *Science Advances* **3** (2017).

[17] Nichele, F. *et al.* Scaling of Majorana Zero-Bias Conductance Peaks. *Phys. Rev. Lett.* **119**, 136803 (2017).

[18] Gül, Ö. *et al.* Ballistic Majorana nanowire devices. *Nature Nanotechnology* **13**, 192–197 (2018).

2

Theory

This thesis deals with the integration of hybrid materials in superconducting circuits to pave the way for creating exotic bound states in microwave quantum devices. For this, the devices are required to endure strong magnetic fields. To support the understanding of this research, this chapter provides some theoretical background. We begin each subject by introducing the conventional case and work our way towards the more unconventional applications that are of interest to this dissertation.

We start with a brief introduction on superconductivity and its behaviour in magnetic field. From there we describe the phenomenon of non-trivial superconductivity, which can be induced in proximity-induced semiconductor systems. The non-trivial state gives rise to the aforementioned exotic bound states.

We continue with some applications of superconductivity. First we discuss Josephson junctions, a superconducting electrical element that is formed by bringing two superconductors in close proximity. In the different subsections we compare the conventional junctions, hybrid junctions and finally the topological junction. We proceed with reviewing superconducting coplanar waveguides. Finally we combine the Josephson junction element with superconducting microwave resonators and summarize some device architectures, concluding with the hypothesised Majorana transmon.

2.1. Superconductivity

In 1911 H. Kamerlingh Onnes discovered superconductivity when he observed the sudden disappearance of electrical resistance upon immersing mercury in liquid helium [1]. He realised the impact of dissipationless electric transport, but the vanishing of the resistance was attributed to the purity of the metal, even though this did not explain the observed sudden drop. It took until 1957 before the first microscopic theory was proposed to explain this phenomenon; the Bardeen-Cooper-Schrieffer (BCS) theory [2].

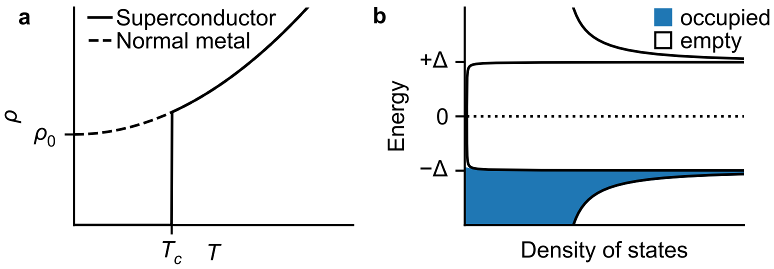

Figure 2.1: **Superconducting properties a** Resistivity vanishes for a superconductor below the critical temperature $T = T_C$. **b** Electrons near the Fermi surface condense into Cooper pairs at the Fermi level μ, leaving a gapped density of states that separates the occupied from the unoccupied electron states.

2.1.1. BCS theory of superconductivity

The BCS theory describes superconductivity as a microscopic effect caused by the condensation of electrons near the Fermi surface into so-called Cooper pairs. Here two electrons with opposite spin and momentum bind together through the attractive potential created by phonon mediated electron-lattice interactions. At a certain critical temperature T_c, thermal phonons will interfere with these electron-lattice interactions, suddenly destroying the superconductivity. Figure 2.1a illustrates this trend. The weak attractive binding potential results in dissipationless electron transport, as observed by the zero-resistance measurement by H. Kamerlingh Onnes [1]. This makes these materials particularly useful for low-loss electronic applications at cryogenic temperatures. Normally the resistance of metals saturates for low temperatures due to the temperature independent scattering by impurities (Figure 2.1a). With the condensation into bosonic Cooper pairs at the Fermi level, a gap of 2Δ in the electron density of states is left behind separating the occupied from the unoccupied states (Figure 2.1b). Unlike the energy bandgap in insulators, electron transport is still possible by the superconducting condensate. The resulting superconducting gap is temperature dependent through the interplay with thermal phonons breaking Cooper pairs and creating excited states just below the gap edge, reducing the effective gap. An important figure is the characteristic length scale over which electrons can condense into Cooper pairs [3]:

$$\xi = \frac{\hbar v_\mathrm{F}}{\pi\Delta} \tag{2.1}$$

where $\hbar$ is the reduced Planck constant and v_F the Fermi velocity.

2.1.2. Superconductivity in magnetic fields

Nowadays, the absence of resistance is not taken as the definition of superconductivity anymore, but rather the demonstration of magnetic flux expulsion, the Meissner-Ochsenfeld effect (Figure 2.2a).

When placed in a magnetic field, the magnetic field penetrates the superconductor over a length λ_s before it is expelled. This length scale is called the London penetration depth and in the simplest case is given by [3]:

$$\lambda_\mathrm{s} = \sqrt{\frac{mc^2}{4\pi ne^2}} \tag{2.2}$$

where m is the mass of the charge carrier, c the speed of light, n the number density of the charge carriers and e the electron charge. Ginzburg-Landau theory provides a macroscopic model that very accurately describes the behaviour of superconductors in larger magnetic fields. Superconductors can be categorised in two types based on how they expel magnetic fields upon increasing the field strength. Type I superconductors transition immediately from complete expulsion of the magnetic field to the normal metallic state. The threshold value for this transition is called the critical magnetic field, B_c. Generally superconductors are of type II, where the transition to the normal state occurs via a so-called mixed state. In the mixed state the magnetic flux perforates the bulk and creates normal cores of radius $\sim\xi$ that are encircled by a supercurrent with outer radius $\sim\lambda_\mathrm{s}$; Abrikosov vortex states. This transition order is defined by the lower critical field B_c1, where the superconductor transitions from the Meissner state to the mixed state, and the upper critical field B_c2, where mixed state transitions to the normal state. Ginzburg-Landau theory can theoretically predict the classification of superconducting materials. The theory determines the sign of the free-energy at the superconductor-boundary which determines whether the formation of vortices is energetically favourable. When the free-energy at the boundary of the superconductor is negative, increasing the superconductor-boundary will lower the energy and therefore invites vortices. The classification can be captured by:

$$\kappa_\mathrm{GL} = \lambda_\mathrm{s}/\xi = \begin{cases} < \frac{1}{\sqrt{2}}, \text{type I} \\ > \frac{1}{\sqrt{2}}, \text{type II} \end{cases} \tag{2.3}$$

Furthermore, Ginzburg-Landau calculations also predict the spatial distribution of vortices, which in de many-vortex regime leads to a hexagonal flux lattice [4].

The destruction of the superconducting state by the magnetic field makes it challenging to utilize superconducting material in significant magnetic fields. Apart from exploiting materials with high critical fields, generally type II superconductors, tricks can be applied in order to engineer magnetic field compatible devices. In this dissertation we obtain magnetic field compatibility by minimizing superconducting film thicknesses, which enhances the superconducting gap [5] and makes it energetically favourable for the magnetic field lines to bend around the film instead [6]. The devices used in this research use readout and control circuitry based on microwave signals. The oscillatory forces exerted on the vortices by the microwave frequencies cause the vortices to migrate, a dissipative process causing microwave losses [7, 8]. The vortex dynamics are determined by the ratio of the viscous force and the pinning forces. We increase the pinning forces by applying a (hexagonal) grid of lithographically defined defects, pinning the magnetic vortices.

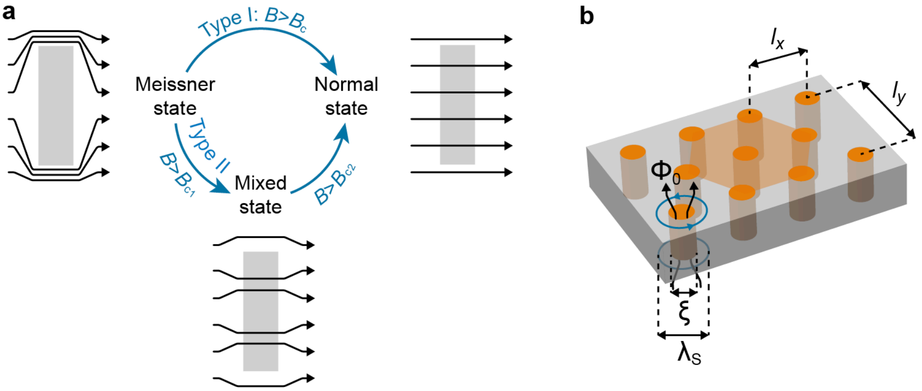

Figure 2.2: **Superconductors in magnetic field. a** The Meissner-Ochsenfeld effect describes how a small magnetic field gets expelled by a superconductor. At increased fields, either the metal collapses into the normal metallic state, or first enters an intermediate mixed states before the normal state is reached. **b** In the mixed state magnetic flux penetrates the superconductor through the creation of Abrikosov vortices, illustrated by the orange cylinders, where flux is focussed through normal state vortex cores. The vortices have normal core radius of $\sim\xi$ which are encircled by a supercurrent with outer radius $\sim\lambda_S$. The vortices repel each other, resulting in a hexagonal packing lattice.

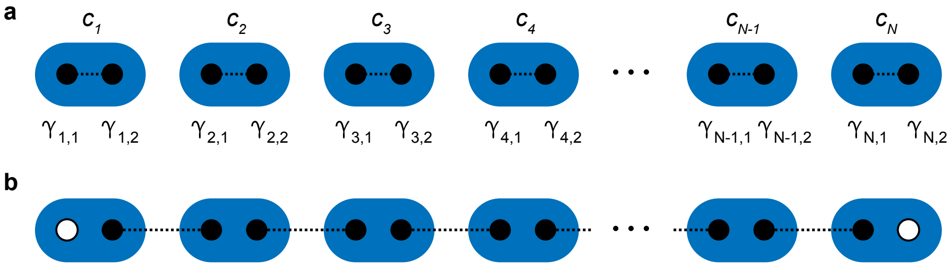

Figure 2.3: **Toy model of topological superconductivity a** One-dimensional electron chain consisting of N electron sites that can either be empty or occupied. The fermionic wavefunction consisting of a real and imaginairy part according to Diracs formulation, as depicted by the two dots within each electron site. **b** Unconventional pairing of the fermionic wavefunctions leads to two spatially separated states at the ends with zero energy that are their own antiparticle; Majorana bound states.

2.1.3. Non-trivial superconductivity

One motive to strive for magnetic field compatible superconducting structures is the promise of topological quantum computing. Here the state of the qubit is encoded by bound states that obey non-Abelian exchange statistics, so-called Majorana bound states (MBSs), that are found in non-trivial superconductors [9]. This type of superconducting state was first theorized by A. Kitaev in 2001 [10], where he describes a toy model of a one-dimensional chain of spinless superconducting electron sites, as schematically depicted in Figure 2.3a. The Hamiltonian captures the kinetic and potential energies, and written in creation ($\hat{c}_n^\dagger$) and annihilation ($\hat{c}_n$) operators for fermionic electron states reads:

$$\hat{H} = -\mu \sum_n \hat{c}_n^\dagger \hat{c}_n - t \sum_n \left(\hat{c}_{n+1}^\dagger \hat{c}_n + \text{h.c.} \right) + \Delta \sum_n \left(\hat{c}_n \hat{c}_{n+1}^\dagger + \text{h.c.} \right) \tag{2.4}$$

Here the first term adds the energy of an electron occupying a site n with an on-site chemical potential μ. The second term accounts for the hopping of electrons between sites, governed by the hopping strength t. And the last term adds spinless superconducting pairing between adjacent electrons with a strength set by the superconducting gap Δ. Note that electron sites can only be occupied by a single electron as the spin degeneracy is lifted in this spinless toy model. Figure 2.3a depicts a schematic representation of this trivial pairing. In the simple case of $\mu = 0, t = \Delta$, the Hamiltonian can be rewritten using the following transformation in operators:

$$\hat{c}_n = \frac{1}{2} \left(\hat{\gamma}_{n,1} + i \hat{\gamma}_{n,2} \right) \tag{2.5}$$

$$\hat{c}_n^\dagger = \frac{1}{2} \left(\hat{\gamma}_{n,1} - i \hat{\gamma}_{n,2} \right) \tag{2.6}$$

The operators $\hat{\gamma}_{n,1}$ and $\hat{\gamma}_{n,2}$ are called Majorana operators as they are their own hermitian conjugate because of their purely real wave function:

$$\hat{\gamma}_{n,1} = \hat{c}_n^\dagger + \hat{c}_n \tag{2.7}$$

$$\hat{\gamma}_{n,2} = \left(\hat{c}_n^\dagger - \hat{c}_n \right) \tag{2.8}$$

An isolated MBS can thus be viewed as an equal superposition of an electron and hole excitation, a Bogoliubov quasiparticle. The rewritten Hamiltonian is then:

$$\hat{H} = -it \sum_{n=1}^{N-1} \hat{\gamma}_{n,2} \hat{\gamma}_{n+1,1} \tag{2.9}$$

Surprisingly, the first and last Majorana site vanished from the Hamiltonian, meaning these states do not contribute to the total energy and hence exist as simultaneous zero-energy states (Figure 2.3b). The ground state of this system is now degenerate since the occupation of these Majorana bound states (MBSs) does not cost energy. Even though the previous derivation was done for $\mu = 0$ these isolated MBSs persist for $\mu < |2t|$. At this point the higher-energy bulk states originally separated by an energy gap of $2t$ approach zero energy and close the gap. The importance of these zero-energy modes lies in the fact that the states are spatially removed while also being isolated from each other through the inverted superconducting bandgap (Figure 2.3c). This ensures inherent protection against local perturbations through non-local information storage, making these quasiparticles theoretically an ideal platform for quantum computing.

However, the prerequisites for the above derivations are demanding and raise questions about the feasibility of such MBSs in practice. Figure 2.4 shows the translation of the theoretical requirements to the experimental implementation. The one-dimensional system is approached by nanostructures that are confined in two directions, as depicted by the nanowire in Figure 2.4a. According to the toy model such a nanowire should be made out of a spinless superconducting material. However, naturally occurring superconductors are almost all s-wave superconductors with spin-singlet pairing. Fortunately, by connecting a superconductor with a second material superconductivity can be induced via the proximity effect. Here the wavefunction of a Cooper pair extends into the other material picking up properties of the proximitized material. Using this trick the spins of Cooper pairs can be manipulated. Figure 2.4b-e illustrates the different steps to mimic spinless superconductivity on-chip. As long as the energy spectrum is non-degenerate, meaning that for every momentum there is only a single spin-state available, the system can be viewed as effectively spinless. To achieve non-degeneracy two symmetries have to be broken; bulk inversion symmetry, $E_{\uparrow,\downarrow}(k) = E_{\uparrow,\downarrow}(-k)$, and time-reversal symmetry, $E_{\uparrow}(k) = E_{\downarrow}(-k)$. Inversion symmetry is broken by a momentum-dependent splitting of the two spin bands when electrons experience an asymmetric potential landscape. In our system we choose the material to have an asymmetric crystal lattice through which the material obtains a spin-orbit interaction (SOI), see Figure 2.4b. An electrostatic gate controls the chemical potential μ within the nanowire, as indicated in the dispersion diagram. Following the order of the fabrication process, Figure 2.4c adds a superconducting shell to the semiconducting nanowire, proximitizing the nanowire as described previously. The electronic band structure now includes hole bands which are mirrored around the Fermi energy and open up an energy gap, the superconducting gap Δ. At this point the spin states are still degenerate at $k = 0$. Figure 2.4d shows this issue is solved by applying an external magnetic field to break time-reversal symmetry. The associated Zeeman-splitting lifts the Kramers degeneracy at $k = 0$ and opens up a gap of $E_{\mathrm{Z}} = \frac{1}{2} g \mu_{\mathrm{B}} B$. One should note that this trick is only available because of the earlier separation of the two spin bands. Increasing the applied magnetic field decreases, closes and finally reopens the superconducting gap. Upon reopening the electron and hole bands are inverted; creating a topological gap with MBSs at the ends. Now that we understand the electronic band structure we can plot the energy gaps at $k = 0$ and $k = k_{\mathrm{SO}}$, to determine the topological phase transition, see Figure 2.5a. Figure 2.5b shows the topological phase diagram for μ, where we can easily conclude $E_{\mathrm{Z}} > \sqrt{\Delta^2 + \mu^2}$.

In summary, to induce MBSs in nanowire structures one requires: **s-wave superconductivity** induced in a **nanowire** made from a semiconductor with large **SOI** placed in a **magnetic field** with electric field control to tune the topological phase.

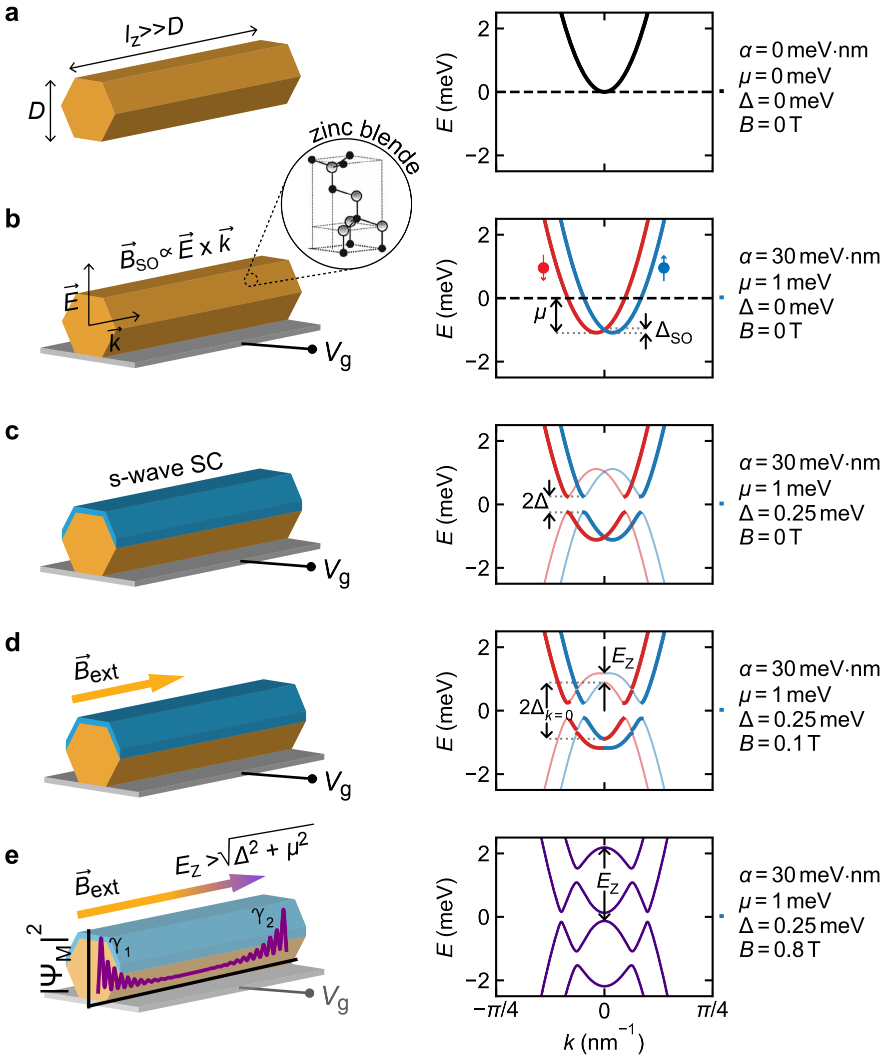

Figure 2.4: **Example of experimental realisation of Majorana bound states.** **a** The one-dimensional character is approached by using a nanowire structure that confines the electrons in two dimensions. The corresponding energy spectrum is a two-fold degenerate parabolic function due to Kramers degeneracy. **b** The nanowire is made from semiconducting material with high spin-orbit interaction, leading to a momentum-dependent splitting of the spin bands. The chemical potential μ is controlled via an electrostatic gate with voltage V_g. **c** An s-wave superconducting shell induces superconductivity in the nanowire through the proximity effect. This introduces particle-hole symmetry, where hole-like states occur that are mirrored around the Fermi level. The coupling between the electron and hole bands, creating Cooper pairs, opens up a superconducting gap. The superconducting gap is determined by the minimum gap between the electron and hole-like bands. **d** A magnetic field is applied to lift the spin-degeneracy at $k = 0$. **e** At sufficient magnetic field strength a band inversion at $k = 0$ occurs, turning the superconducting gap topological with MBSs occuring at the ends. Dispersion diagrams calculated using [11].

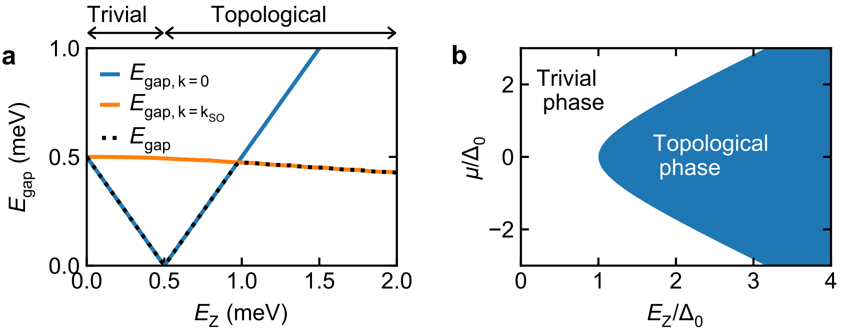

Figure 2.5: **Topological phase. a** The evolution of the energy gap with increasing B around the Fermi level at $k = k_{\mathrm{SO}}$ (orange) and $k = 0$ (blue), and the overall energy gap (dotted black) for $\mu = 0$. The closing of the gap at $k = 0$ inverts the gap, giving rise the topological phase. **b**. Phase diagram as function of the normalised chemical potential and normalised Zeeman splitting, with Δ_0 the proximity-induced pairing gap in the wire.

2.2. The Josephson effect

Only a few years after the BCS theory was published B. Josephson predicted the effect of the tunnelling of Cooper pairs between two superconductors in close proximity, which gives rise to a dissipationless current called the supercurrent [12]. The first experimental observation followed quickly [13] and nowadays the Josephson junction (JJ) is indispensable in superconducting quantum circuits due to it non-linear nature.

2.2.1. Tunnel junctions

The most common JJ consists of two superconductors that are separated by a thin layer of insulating material, a superconductor-insulator-superconductor (SIS) JJ. The tunnelling probability of a Cooper pair tunnelling from one superconducting condensate to another through an insulating barrier decays exponentially with thickness. This quantum mechanical process is dissipationless and results in a supercurrent. The supercurrent follows a current-phase relation that is determined by the phase difference between the two coherent many-body condensate wavefunctions:

$$I\left(\phi\right) = I_{\mathrm{c}}\sin\left(\phi\right) \tag{2.10}$$

where $\phi = \phi_{\mathrm{L}} - \phi_{\mathrm{R}}$ and I_{c} is the critical current, the maximum value the supercurrent can attain and depends on junction parameters like material, dimensions and defects. This phenomenon is called the d.c. Josephson effect and holds for currents $I < I_{\mathrm{c}}$. For larger drive currents a voltage drop V is built across the JJ, creating a potential offset between the condensates. Tunnelling through the barrier can take place only as a virtual process, giving rise to an oscillating current with a steadily increasing phase difference with time; the a.c. Josephson effect:

$$I\left(\phi\right) = I_{\mathrm{c}}\sin\left(\phi(0) + \frac{2eV}{h}t\right) \tag{2.11}$$

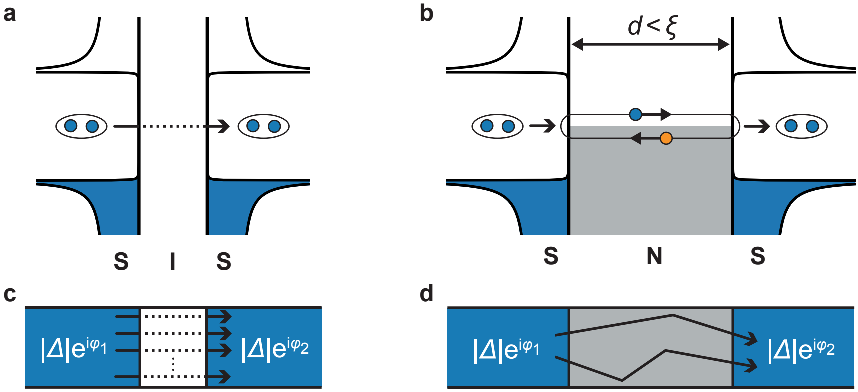

Figure 2.6: **Josephson effect in weak-links a** Density of states of a SIS JJ. Cooper pairs can tunnel coherently from one condensate to the other with no resistance, adding up to the supercurrent. **b** Density of states of a SNS JJ where at each interface the incoming electron is retroflected as a hole, and vice versa, constituting an Andreev bound state that carries the supercurrent. **c** Schematic illustration of a conventional SIS JJ where the total supercurrent is the accumulative result of many low transmitting channels. **d** Schematic illustration of a SNS JJ, where only a few highly transmitting ABS modes constitute the total supercurrent.

where $f_\mathrm{J} = \frac{2eV}{h}$ is the Josephson frequency and is bound by the superconducting gap.

Because of the non-linear current-phase relation the JJ is indispensable in superconducting quantum circuits and is exploited for introducing non-equidistant eigenstates enabling individual addressable states in superconducting qubits and for its non-linearity in gain mediums for voltage-to-frequency conversion. The simplest application can be made by arranging two JJs in parallel in a superconducting ring, a Superconducting Quantum Interference Device (SQUID), where the current in the ring depends on the interference of both JJs. This results in a flux-tunable supercurrent and its sensitivity makes it very suitable for accurate magnetic field measurements.

When embedding a JJ in a superconducting circuit the behaviour is determined by the ratio of the energy scales associated with different elements. The energy stored by the Josephson coupling is determined by the critical current and scales with the magnetic flux quantum Φ_0:

$$E_\mathrm{J} = \frac{\Phi_0 I_\mathrm{c}}{2\pi} \tag{2.12}$$

2.2.2. Andreev bound states

Similarly, the d.c. and a.c. Josephson effects occur when the superconducting leads are separated by a normal metal or semiconductor, referred to as hybrid SNS JJs. In this case the conduction mechanism does not originate from tunnelling events but from the process of Andreev reflection at the interface between the normal metal and superconductor. A free electron with energy within the superconducting gap that incidents on the superconductor can reflect on the interface, or it can propagate into the superconductor by combining with another electron to form a Cooper pair. The conservation of charge, momentum and spin prescribe that the formation of a Cooper pair requires the creation of a hole with opposite momentum and spin to the incoming electron. In a SNS JJ, where a normal metal is sandwiched between two superconductors, the incident hole gets retroflected again as an electron at the opposing interface. The resulting perpetual reflection process between the two NS-interfaces is called an Andreev bound state (ABS). This process allows coherent transfer of Cooper pairs between the two condensates, again resulting in the Josephson effects but this time mediated by the retroflection of charge carriers.

In the short junction regime, where the junction length d is smaller than the superconducting coherence length ζ, only a single particle-hole pair lies below the gap with a 4π-periodic energy dispersion relation of [14, 15]:

$$E_{\mathrm{ABS},\pm}(\phi) = \pm\Delta\cos(\phi/2) \tag{2.13}$$

However, realistically even in the short junction regime such junctions are not ballistic and some scattering centers are present. The addition of a scattering center lowers the transmission D and makes the energy of an ABS transmission dependent:

$$E_{\mathrm{ABS},\pm}(\phi) = \pm\Delta\sqrt{1 - D\sin^2(\phi/2)} \tag{2.14}$$

where the two signs corresponding to current flow in opposite directions and T is the transmission of the conduction channel. For lower transparencies the two opposite current flows mix since a scattering event alters the direction of the charge carrier coupling it to the other current flow. This coupling opens up an avoided crossing at $\phi = \pi$ between the energy levels of magnitude $2\Delta\sqrt{1-D}$, where increased scattering (lower transparency) shows stronger coupling (Figure 2.7a). Therefore the energy shows less strong dependent on the superconducting phase difference, agreeing with the destruction coherent transport through the coupling of the phases of the condensates. The splitting of the energy spectrum into two bands creates the notion of a ground state and excited state. For $T = 20\,\mathrm{mK}$, the base temperature of our dilution refrigerator, we assume that only the ground states of the ABSs are occupied. However, in the case of a very high transparency channel ($D \rightarrow 1$) or non-adiabatic driving of ϕ allowing for Landau-Zener tunnelling between the two branches, a population of the excited state needs to be taken into account. The total energy stored is described by the collection of all occupied ABSs:

$$E_{\mathrm{J}}(\phi) = \sum_i E_{\mathrm{ABS},i} = \Delta\sum_i \sqrt{1 - D_i\sin^2(\phi)} \tag{2.15}$$

From which the supercurrent can be derived [16]:

$$I_{\mathrm{ABS}}(\phi) = \frac{e\Delta}{2\hbar}\sum_i \frac{D_i\sin(\phi)}{\sqrt{1 - D_i\sin^2(\phi/2)}} \tag{2.16}$$

The corresponding current-phase relations for the different transparencies are shown in Figure 2.7b. In the limit where $D = 1$, the current-phase relation is discontinuous at $\phi = \pi$. Here the discontinuity is caused by the connection the ABS provides between

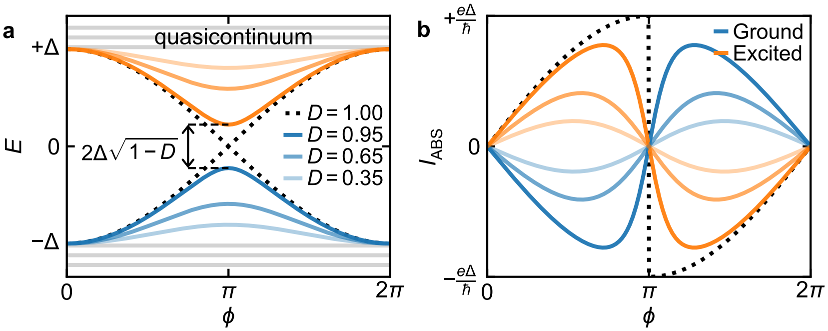

Figure 2.7: **ABSs dependence on transparency a** ABSs energy dispersion dependence on transparency with respect to perfect transmission (dotted line). Scattering, $D < 1$, causes mixing of opposite propagating ABSs opening up a gap resulting in a ground (solid blue) and excited state (solid red). Lower D pushes the ABSs into the quasicontinuum. **b** Current-phase relation dependence on D, showing sinusoidal behaviour at low D, but highly skewed behaviour at high D.

the two quasicontinuums. For high transparencies, $D \to 1$, the current-phase relation approaches this limit, resulting in a highly skewed current-phase relation. However at low transparencies, when the system resembles more and more a tunnelling junction as the ABSs are pressed into the continuum, the sinusoidal form returns. Mathematically Equation (2.16) indeed approaches Equation (2.10) in the many-channel regime with low transparencies.

2.2.3. Topological Josephson junction

According to section 2.1.3, fabricating a SNS JJ from a proximitized semiconducting nanowire with spin-orbit coupling allows us to induce MBSs at either side of the junction when subjected to a sufficiently large magnetic field (Figure 2.8a). At relatively short JJs the inner Majorana zero modes (MZMs), both originating from a different MBS, overlap. This interaction, defined as the Majorana energy E_M, has never been recorded and its order of magnitude is unknown but is of importance for designing a topological qubit.

Despite being neutrally charged quasiparticles by themselves, the hybridization into a fermionic state allows for phase-coherent single electron tunnelling through the junction [18, 19]. Similar to the d.c. Josephson effect the resulting supercurrent is dependent on ϕ, however now with an anomalous periodicity of 4π [10]:

$$I_\mathrm{MBS}(\phi) \propto \sin(\phi/2) \tag{2.17}$$

This fractional Josephson current can be understood by the fact that the transfer of a single electron excites the superconducting condensates and therefore there has to be a protected crossing at $\phi = \pi$ with perfect population inversion. In other words, the system cannot remain in the ground state as ϕ evolves from 0 to 2π adiabatically. Unlike for ABSs, where the back-reflected hole ensures the fermion parity.

The coherent transfer of a single electron mediated by the MZMs also gives rise to a fractional a.c. Josephson effect. This fractional analogy of the a.c. Josephson effect owes

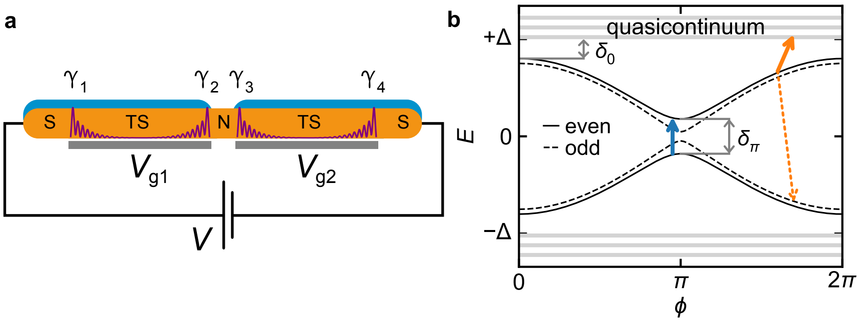

Figure 2.8: **Topological Josephson junction.** **a** MBSs, γ_i, appear at the ends of the topological superconducting (TS) regions, as illustrated by the purple wavefunctions. When γ_2 and γ_3 overlap sufficiently, they can mediate coherent single-electron transport across the JJ. **b** The energy dispersion resembles an ABS state with perfect transparency through the coupling of γ_2 and γ_3, leading to a 4π-periodic dispersion relation. Taking into account a finite length of the TS regions shows the 4π-periodicity is lifted by the avoided crossing due to the residual coupling between γ_1 and γ_4. LZ-tunnelling events (blue arrow) can overcome this, but can at the same time obstruct the observation of a 4π-periodic dispersion relation by stimulating LZ-tunneling into the quasicontinuum (orange arrows). Sufficiently long TS regions are thus a necessity for observing this phenomenon. Figure adapted from [17].

its name to the single electron charge that is transferred, cutting the frequency in half:

$$f_{\mathrm{MBS}} = eV/h \tag{2.18}$$

The two MZMs hybridize into eigenstates of opposite fermion parity which are dependent on the effective induced topological gap Δ_T and the channel transparency according to:

$$E_{\mathrm{MBS},\pm}(\phi) \propto \pm\Delta_\mathrm{T}\sqrt{D}\cos(\phi/2) \tag{2.19}$$

Up until now we have neglected the accompanying MZMs at the wire ends. Just like the ”inner” MZMs, these ”outer” MZMs also show overlap for finite wire length and thus hybridize. Taking this into account will add two energy eigenstates to the system, one corresponding to the even parity and one to the odd parity state [17]. Equal parity states can now interact, leading to anti-crossings at $\phi = \pi$ and breaking the 4π-periodicity. The resulting dispersion diagram is now indistinguishable from the trivial 2π periodic ABS signal. Fortunately with well-targeted driving Landau-Zener transitions can restore the 4π-periodicity while keeping parity-mixing excitations into the quasicontiuum (quasiparticle poisoning) negligible.

The observation of the fractional Josephson effect in this semi-adiabatic limit would provide strong evidence for the realisation of Majorana fermions. The coherent nature distinguishes this signature from dissipative quasiparticle excitation tunnelling events.

2.3. Circuit quantum electrodynamics

The application of superconducting coplanar waveguide resonators initiated the research field of circuit quantum electrodynamics (circuit QED), the superconducting electronic circuit analogue of cavity quantum electrodynamics (cavity QED). The field of cavity QED

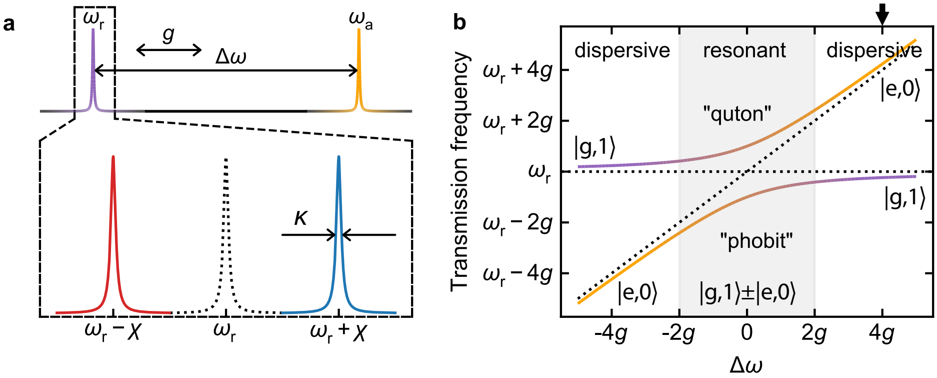

Figure 2.9: **Dispersive regime a** Frequency spectrum showing the resonator at resonance frequency ω_r and artificial atom at ω_a in the dispersive regime where $\Delta\omega \gg g$. Zooming in on the resonator response shows a state dependent frequency response with dispersive shifts $-\chi$ for the excited state and $+\chi$ for the ground state of the atom. **b** Coupling of the resonator and artificial atom for $n = 1$ excitation in the system, resulting in an avoided crossing of size $2g$. In the resonant limit (grey shaded area) the two systems lose their individual character. Upper arrow indicates the linecut depicted in (a)

studies the fundamental quantum mechanical coupling between light and matter. Here light is confined in a reflective three-dimensional cavity that acts as a harmonic oscillator whose excited states are photons. To reach the quantum regime, the number of photons needs to be a well-defined quantum number. To this end the non-linear character of atoms is exploited where through exciting the atom a single photon is emitted during the decay process. While the atom can be isolated to maintain its coherence exquisitely long, the interaction time between the atom and photon is quite small making it difficult to observe the back-action on one another. Unlike in cavity QED the coupling strength is the main asset in circuit QED, where the interaction between light and matter is studied on-chip in the microwave regime using engineered atoms. The cavity is now substituted by a one-dimensional dissipationless superconducting resonator and the artificial atoms are mesoscopic devices with an anharmonic (unevenly spaced) energy spectrum. For a one-dimensional transmission line cavity, where two dimensions are much smaller than a wavelength, the energy density is increased more than 6 orders of magnitude with respect to the conventional three-dimensional cavities [20]. Together with the fact that the effective dipole moment of a many-atom system can be engineered to be 10 times higher than even a Rydberg atom, this allows for strong coherent coupling despite of the larger decoherence to its solid state environment. Due to the great flexibility of the design and the in-situ manipulation of the artificial atoms, circuit QED is a promising candidate for future quantum computation [21] and owes it success to quantum non-demolition (QND) readout by dispersive readout using a coplanar waveguide.

Dispersive readout

The resonator-*atom* system is described by the Jaynes-Cummings Hamiltonian where a two-level system interacts via a dipole interaction with a harmonic oscillator [22]:

$$\hat{H}_{\mathrm{JC}} = \hbar\omega_{\mathrm{r}}\left(\hat{a}^{\dagger}\hat{a} + \frac{1}{2}\right) + \frac{\hbar\omega_{\mathrm{a}}}{2}\hat{\sigma}_{\mathrm{z}} + \hbar g\left(\hat{a}^{\dagger}\hat{\sigma}^{-} + \hat{a}\hat{\sigma}^{+}\right) \tag{2.20}$$

where the first term represents the energy of the quantized bosonic electromagnetic field stored in the cavity with each photon adding an energy $\hbar\omega_{\mathrm{r}}$. The second term represents a fermionic two-level system with excitation energy $\hbar\omega_{\mathrm{a}}$. The last term describes the interaction between the two; the absorption of a photon excites the two-level system, $\hat{a}\hat{\sigma}^{+}$, and the decay of the two-level system emits a photon into the electromagnetic field $\hat{a}^{\dagger}\hat{\sigma}^{-}$, both governed by the coupling rate $g/2\pi$. When the coupling rate g is much bigger than the lifetime κ of the cavity and the decay rate γ of the coupled system; $g \gg \kappa, \gamma$, the system is said to be in the strongly coupled regime. The decay rate of the total system is determined by both κ and γ. When $\kappa \gg \gamma$ the decay of the cavity modes dominate and accelerate the decay of the coupled system, known as the Purcell effect [23].

Another way of controlling the degree of hybridization of both systems, besides the coupling rate g which is set during fabrication, is by detuning the atom and cavity in frequency; $\Delta\omega = \omega_{\mathrm{a}} - \omega_{\mathrm{r}}$. In the resonant limit where $\Delta\omega \ll g$, the two systems inherit each others properties to such an extend that they lose their individual character. This leads to interference of the quantum state of the two-level system via the Purcell effect. To preserve the state of the coupled two-level system it is preferable to work in the dispersive limit. Here the detuning between the qubit transition frequency and the resonator frequency is much larger than the interaction strength, $\Delta\omega \gg g$, leading to the approximate effective Hamiltonian [21]:

$$\hat{H}_{\mathrm{eff}} \approx \hbar\left(\omega_{\mathrm{r}} + \frac{g^{2}}{\Delta\omega}\hat{\sigma}_{\mathrm{z}}\right)\left(\hat{a}^{\dagger}\hat{a} + \frac{1}{2}\right) + \frac{\hbar\omega_{\mathrm{a}}}{2}\hat{\sigma}_{\mathrm{z}} \tag{2.21}$$

where indeed the last term representing the two-level system is unchanged, however the first term now includes both the electromagnetic field and the interaction term. This yields a dispersive frequency shift $\chi = \frac{g^{2}}{\Delta\omega}$ of the electromagnetic field resulting in a shifted resonance frequency $\omega_{\mathrm{r}}' = \omega_{\mathrm{r}} + \chi$. The renormalised resonance frequency is dependent on the state of the atom and enables quantum non-demolition (QND) measurements. The back-action of the resonator on the coupled two-level system can be understood by rewriting that same expression into:

$$\hat{H}_{\mathrm{eff}} \approx \hbar\omega_{\mathrm{r}}\left(\hat{a}^{\dagger}\hat{a} + \frac{1}{2}\right) + \frac{\hbar\hat{\sigma}_{\mathrm{z}}}{2}\left(\omega_{\mathrm{a}} + \frac{2g^{2}}{\Delta\omega}\hat{a}^{\dagger}\hat{a} + \frac{g^{2}}{\Delta\omega}\right) \tag{2.22}$$

where we now can recognise the photon number dependent Stark shift $\frac{2ng^{2}}{\Delta\omega}$ and vacuum noise Lamb shift $\frac{g^{2}}{\Delta\omega}$. Combining the requirements for the coupling and the energy decay of both elements in the dispersive regime yields $\chi = \frac{g^{2}}{\Delta\omega} > \gamma, \kappa$ for reaching the strongly coupled dispersive regime.

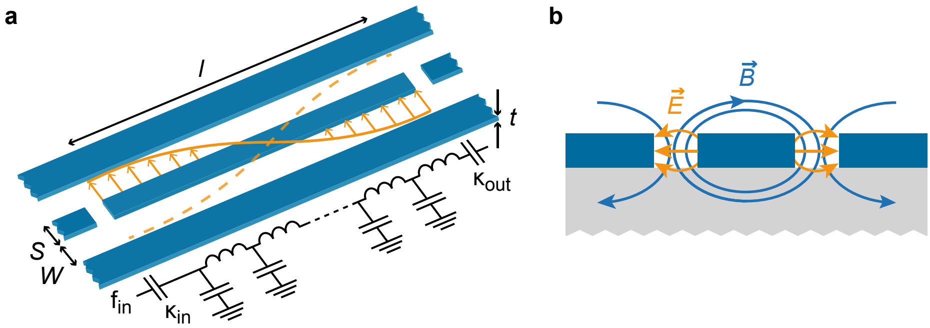

Figure 2.10: **Coplanar waveguide resonator.** **a** Schematic of a $\lambda/2$ CPW of length l, center conductor width S, ground plane gap W, and thickness t, capacitively coupled to the input and output ports with coupling rates κ_{in} and κ_{out} respectively. The fundamental mode of the electric field is indicated in orange, showing antinodes at the ends of the center conducting strip. The equivalent lumped element circuit is shown below. **b** Cross-sectional view of the CPW, showing a schematic representation of the low-loss coplanar transverse electromagnetic mode (TEM). Figure adapted from [24].

2.3.1. Superconducting microwave resonators

For the control and readout of our circuit QED devices we use superconducting transmission coplanar waveguide (CPW) resonators. Figure 2.10a illustrates the dimensions that define the systems properties; a central conductor of width S, length l and thickness t which is separated from the ground plane by a gap of width W. In close resemblance to a coaxial cable, the electromagnetic field is stored in the gap and is perpendicular to the direction of propagation. Galvanic connection of the two ground planes ensures that there is no potential difference giving rise to the low-loss coplanar transverse electromagnetic mode (TEM), as shown in Figure 2.10b. Two gap capacitors at either end of the cavity act as mirrors for the microwave photons with a transparency defined by the in- and output coupling rates κ_{in} and κ_{out}. Figure 2.10a shows the electric field anti-nodes at the ends of the CPW as a result of the reflection at the gap capacitors, making the fundamental mode half a wavelength ($2l = \lambda_0$). Capacitive coupling of a two-level system to the resonators electric field can be achieved by placing the system at the ends of the resonator. The fundamental mode of the magnetic field, being orthogonal to the electric field, shows a antinode in the middle of the resonator. Therefore for inductive coupling the two-level system should be placed in the center. The interaction between the resonator and coupled system depends on the intensity of the EM-field and is therefore highly dependent on the gap W. In a similar way quarter wavelength ($4l = \lambda_0$) CPWs can be constructed by capacitively coupling one end to a so-called feedline while terminating the other end by a metallic connection to ground; creating an electric field anti-node at the gap capacitor and electric field node at the grounded end. By splitting the total bandwidth into non-overlapping frequency bands, called multiplexing, one can integrate multiple $\lambda/4$-resonators on a single chip that can each be addressed individually and simultaneously. This technique is well-known from the telecom industry and allows for easy upscaling of the number of devices per chip.

The strength of circuit QED devices lies in the strong coupling between resonator and the coupled system, which can be targetted the capactive (or inductive) coupling strength and the frequency detuning. In a solid state CPW the resonance frequency depends on the length l, but also on the geometrically defined capacitance C and kinetic inductance L [25]:

$$\omega_\mathrm{r} = \frac{2\pi}{2l\sqrt{L_\mathrm{l}C_\mathrm{l}}} \tag{2.23}$$

where L_l and C_l are the inductance and capacitance per unit length. Where

$$L_\mathrm{l}C_\mathrm{l} = \mu_0\epsilon_0\epsilon_\mathrm{eff} \tag{2.24}$$

where μ_0 and ϵ_0 are the permeability and permittivity in vacuum respectively, and ϵ_eff the effective dielectric constant which is a function of the waveguide parameters S, W and t, the film thickness, and the relative permittivies of the substrate materials [25]. For magnetic field compatible devices, as designed in this research, we minimized the film thickness t. The reduced film thickness can sufficiently lower the electron density such that the internal kinetic inductance significantly increases. In designing our CPW resonators we need to account for this, as described by [26]. Not only are L_l and C_l important to target the resonance frequency, their ratio also dictates the impedance of the resonator, $Z_0 = \sqrt{L_\mathrm{l}/C_\mathrm{l}}$. The impedance needs to be matched to the impedance of the external circuit, with characteristic impedance of $Z_0 = 50\,\Omega$, to minimize undesirable reflections that cause signal distortions.

The capacitance needs to be designed such that the lifetime κ of the cavity allows for strong coupling, while still allowing for fast control and readout via the in- and output port capacitors. The average lifetime of a photon in the cavity is proportional to the energy loss per cycle, called the quality factor Q:

$$Q = \frac{\omega E}{P} \tag{2.25}$$

where E is the maximum stored energy and P is the power loss. When the resonator is coupled to a readout circuit the loaded quality factor Q_l can be measured. The loss channels can be divided in two factors: the coupling quality factor that accounts for the photons that exit the cavity to readout circuit, defined by Q_c, and the intrinsic quality factor which captures the internal loss channels. Together the overall loaded quality factor Q_l is then described by:

$$\frac{1}{Q_\mathrm{l}} = \frac{1}{Q_\mathrm{c}} + \frac{1}{Q_\mathrm{i}} \tag{2.26}$$

Intrinsic loss mechanisms should be minimized as they do not add to the signal readout. Common sources are sheet resistance, radiative losses and dielectric losses. Utilizing superconducting materials reduces sheet resistance induced losses and proper packaging and shielding of the set-up minimizes radiative losses. Dielectric material should be minimized in the device design, especially at places where the electric/magnetic field density are high. If necessary, materials with lower dielectric loss tangent should be favoured.

2.4. Artificial atoms

Artificial atoms for superconducting electronics can be engineered by combining capacitors, inductors and the JJ. Of these the JJ is the only non-dissipative, strongly non-linear circuit element available at low temperature [27] and therefore the key element of all artificial atoms. As mentioned, the solid state circuitry makes a lossy environment, to which each system has different susceptibilities depending on the controlled quantum variable and its conjugate. Below we discuss a few charge-based superconducting architectures for quantum computing that are important to the understanding of this dissertation.

2.4.1. Josephson laser

The simplest artificial atom is a single JJ. When coupling a JJ to a cavity one can enable the exchange of photons between the Cooper pair tunneling process across the JJ and the photons within the cavity. The process of Cooper pair tunneling under exchange of photons is called the a.c. Josephson effect, and the photons generated is referred to as Josephson radiation. The frequency of the Josephson radiation is set by the cavities resonance frequency.

The system can be mathematically understood as a damped and driven oscillators [28–30]. The oscillators describe the multimode transmission line cavity, which is driven by the JJ:

$$\ddot{\varphi}_n + \frac{\omega_n}{Q_n}\dot{\varphi}_n + \omega_n^2\varphi_n = -\alpha_n \frac{E_\mathrm{J}}{\Phi_0^2 C}\cos\sum_n \alpha_n\varphi_n + \omega_\mathrm{J} t \tag{2.27}$$

here the left part of the equation describes the oscillator modes with phase φ_n, frequency ω_n and quality factor Q_n, belonging to the n^{th} excitation mode. The right side of the equation describes the driving term, also called the forcing function, and its coupling α_n. The forcing function depends on the total capacitance C, the Josephson energy E_J, the Josephson frequency $\omega_\mathrm{J} = \frac{2eV}{\hbar}$ and time t, and $\Phi_0 = \frac{h}{2e}$ is the magnetic flux quantum. Generally the capacitance C is set by the device design, leaving E_J as the single tuning knob in the experiment.

Two different regimes can be distinguished, which are best understood when defining $\lambda = \frac{E_\mathrm{J}}{m\omega_0^2}$ as the forcing strength with $m = \Phi_0 C$ as the effective mass. For $\lambda \ll 1$, where E_J is small in comparison to C, the process is dominated by spontaneous emission, meaning that there is no non-linear interaction with JJ upon a cavity round-trip. This regime is called the linear regime. The non-linear regime, where $\lambda > 1$ corresponding to large E_J in comparison to C, the process is governed by stimulated emission. In this case, photons interact with the JJ every round-trip in the low-loss cavity, subsequently stimulating new emission. Through the junction-cavity back-action this process results in coherent amplification of the electromagnetic field in the cavity, known as lasing. Such Josephson lasing has been experimentally shown by [31].

In Chapter 5 we implemented a semiconductor JJ paving the way to fast electrostatically controlled on-chip microwave generation at low-temperatures.

2.4.2. Cooper Pair Box

The most straightforward charge qubit is the Cooper pair box (CPB). The CPB consists of a mesoscopic superconducting island connected to a large reservoir via a JJ with Josephson energy E_J and capacitance C_J. The island has a total capacitance to ground $C_\Sigma = C_\mathrm{g} + C_\mathrm{J}$ where C_g is the gate induced capacitance polarizing the system and attracting or repulsing excess island charges. The confinement of the island quantizes the excess

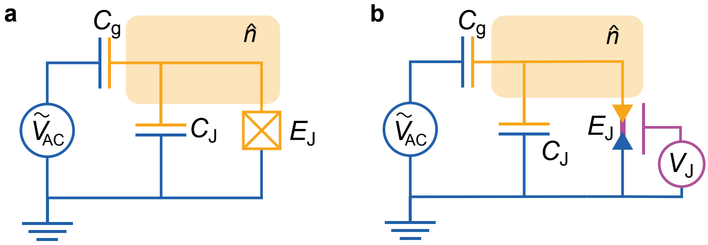

Figure 2.11: **Circuit diagram Cooper Pair Box** for **a** a single SIS junction and **b** a SNS junction equivalent that allows for electrostatic gating of E_J through the voltage V_J. The shaded boxes represent the CPB island hosting $\hat{n}$ excess electrons.

charge to an integer number. Experimentally the charge frustration can be tuned via a gate voltage V_g, setting the excess charge to $n_g = Q_{env}/2e + C_g V_g/e$ with Q_{env} representing the environment induced offset charge. The Hamiltonian of the total CPB is described by:

$$\hat{H}_{CPB} = 4E_C\left(\hat{n} - n_g\right)^2 + E_J \cos\hat{\phi} \tag{2.28}$$

where the first term describes the excess charges $\hat{n}$ on the island with Coulomb charging energy $E_C = \frac{e^2}{2C_\Sigma}$ and the second term represents the Josephson coupling between the two superconductors governed by the phase difference $\hat{\phi}$. Figure 2.11 shows the circuit diagram representation both for a conventional SIS JJ and a semiconducting SNS junction that allows for electrostatic control of E_J.

The ratio of the Josephson with respect to the charging energy determines the ease with which charge can be exchanged with the environment and thus the degree of charge localization. The CPB regime is the regime where charge is quantized with a corresponding ratio of $E_J/E_C \sim 1$. Figure 2.13a shows the eigenstates of the CPB Hamiltonian. The charge parabolas belonging to different number of excess charges couple via the Josephson coupling and open up avoided crossings. The mixing of the charge parabolas separates the spectrum in different energy bands that dispers with charge. The qubit transition frequencies, the energy difference between consecutive energybands, are therefore offset charge dependent. It is crucial to the operation of a qubit that these transition frequencies are all different such that the fundamental qubit transition frequency that excites the qubit from the ground state to the first excited state is unique. This ensures that this fundamental transition can be addressed individually to reduce the many-level system to a qubit. The charge dispersion guarantees this requirement. Near the avoided crossings, at $n_g = m + \frac{1}{2}$ where m is an integer, the energy bands for the ground and first excited state are flattest, resulting in a qubit frequency that is least sensitive to charge perturbations. Hence utilizing the qubit at this point in charge space leads to increased coherence times and is called the sweet spot. The fundamental qubit frequency at the sweet spot is set by the size of the avoided crossing resulting in $\omega_{01} \simeq E_J/\hbar$.

Well-defined charge makes the system susceptible to the environmental offset charge and thus also to charge noise. Charge noise can originate from charge traps in the environment, but can also finds its origin from within the superconductor. Even though the

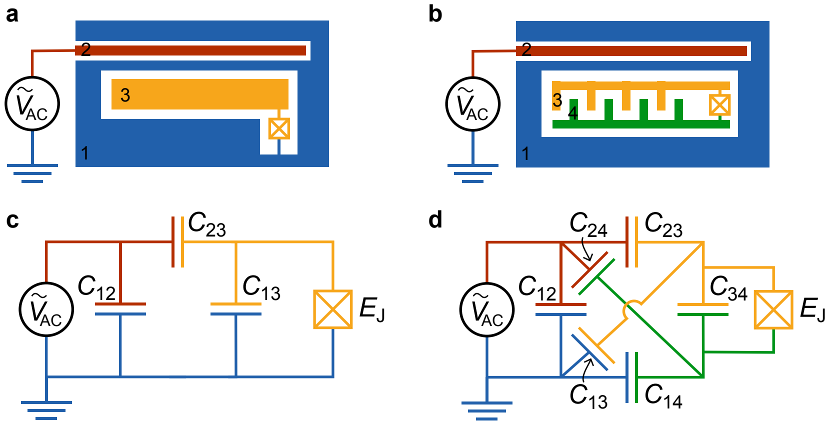

Figure 2.12: **Circuit diagram transmon qubits a** Schematic diagram visualising the single island geometry utilized in Chapter 6 and **b** the double island geometry used in Chapter 4. **c-d** show the equivalent circuit diagrams taking into account all cross-capacitances. Partially reproduced from [26].

electrons in a superconductor are mostly condensed into Cooper pairs of charge $2e$, single quasiparticle excitations of charge e are still present. The tunnelling of such a quasiparticle poisons the island and causes total dephasing of the qubit state.

2.4.3. Transmon

A transmission-line shunted plasma oscillation qubit, abbreviated to transmon, is in its design very similar to the CPB qubit. The qubit differs only by having a large shunt capacitor reducing the Coulomb charging energy E_C and therefore allows for easy capacitive readout by a transmission-line. In this thesis both single island (Figure 2.12a) and double island (Figure 2.12b) designs have been exploited. The circuit diagrams are closely related to the CPB (Figure 2.12c-d), especially for the single island transmon the qubit is identical. However, the shunt capacitor C_{13} (C_{34}) in the single (double) island geometry is now determined by the large shunt capacitor with $C_\mathrm{shunt} \gg C_\mathrm{J}$.

The effective Hamiltonian of the system can be reduced to the Hamiltonian of the CPB in equation 2.28, where the energy band structure now depends on the ratio E_J/E_C. By increasing this ratio the eigenenergies lower due to the renormalisation of E_C while the avoided crossings grows in magnitude, flattening the charge dispersion as the charge delocalises (Figure 2.13). The eigenenergies ar now defined by [32]:

$$E_m\left(n_\mathrm{g}\right) = E_C a_{2\left(n_\mathrm{g}+k\left(m,n_\mathrm{g}\right)\right)}\left(-E_\mathrm{J}/2E_C\right) \tag{2.29}$$

$$k\left(m,n_\mathrm{g}\right) = \sum_{l=\pm1}\left(\mathrm{int}(2n_\mathrm{g}+l/2) \bmod 2\right) \times \left(\mathrm{int}\left(n_\mathrm{g}\right) + l\left(-1\right)^m\left(m+1\right)\ \mathrm{div}\ 2\right) \tag{2.30}$$

where $a_{⊠}\left(q\right)$ is the Mathieu characteristic value describing the eigenvalues of an elliptical drum with periodic boundary conditions. The function $k\left(m,n_\mathrm{g}\right)$ assigns the eigenenergy values to the right energyband as it keeps track of the integer number of cycles, where mod is the modulo operator and a div b the integer division of $\frac{a}{b}$. In the limit of large E_J/E_C the energy levels can be approximated by a cosine:

$$E_m \simeq E_m\left(n_\mathrm{g} = 1/4\right) - \frac{\delta_m}{2}\cos\left(2\pi n_\mathrm{g}\right) \tag{2.31}$$

where δ_m is the charge dispersion and is defined as:

$$\delta_m \equiv E_m\left(n_\mathrm{g} = 1/2\right) - E_m\left(n_\mathrm{g} = 0\right) \tag{2.32}$$

which for $E_\mathrm{J}/E_C \gg 1$ approaches the semi-classical WKB solution:

$$\delta_m = (-1)^m E_C \frac{2^{4m+5}}{m!}\sqrt{\frac{2}{\pi}}\left(\frac{E_\mathrm{J}}{2E_C}\right)^{\frac{m}{2}+\frac{3}{4}} e^{-\sqrt{8E_J/E_C}} \tag{2.33}$$

For $E_\mathrm{J}/E_C > 50$, the transmon regime, the energy bands are flattened to an extend that renders the device practically charge insensitive. And the fundamental qubit frequency has become E_C-dependent following $\omega_{01} \simeq \sqrt{8E_\mathrm{J}E_C}/\hbar$. The increase of the charge-noise insensitivity comes at the cost of a loss in anharmonicity, quantified as $\alpha \equiv E_{12} - E_{01}$ with $E_{ij} \equiv E_j - E_i$. However α only reduces with a weak algebraic power law while the charge dispersion δ_m decreases exponentially in E_J/E_C. Consequently, the transmon can be operated with greatly reduced charge sensitivity while retaining sufficient anharmonicity. The flat energy bands eliminate the concept of a sweet spot in charge space and therefore electrostatic gating of the island in this geometry is redundant.

Due to the reduced anharmonicity the transmon can not be considered a pure two-level system anymore and virtual transitions through excited transmon states need to be taken into account. Remarkably, the transmon behaves conceptually like a CPB in the dispersive regime (Section 2.3) with additional renormalisations due to the interactions. The renormalised resonance frequency of the cavity ω_r' and the fundamental qubit transition frequency ω_{01}' yield:

$$\omega_\mathrm{r}' = \omega_\mathrm{r} - \chi_{12}/2 \tag{2.34}$$

$$\omega_{01}' = \omega_{01} + \chi_{01} \tag{2.35}$$

where the partial dispersive shift χ_{ij} is given by:

$$\chi_{ij} \equiv \frac{g_{ij}^2}{\omega_{ij} - \omega_\mathrm{r}} \tag{2.36}$$

where $\omega_{ij} = \omega_i - \omega_j$ and g_{ij} is energylevel dependent coupling. Combining the renormalisation results in a total effective dispersive shift of:

$$\chi = \chi_{01} - \chi_{12}/2 \tag{2.37}$$

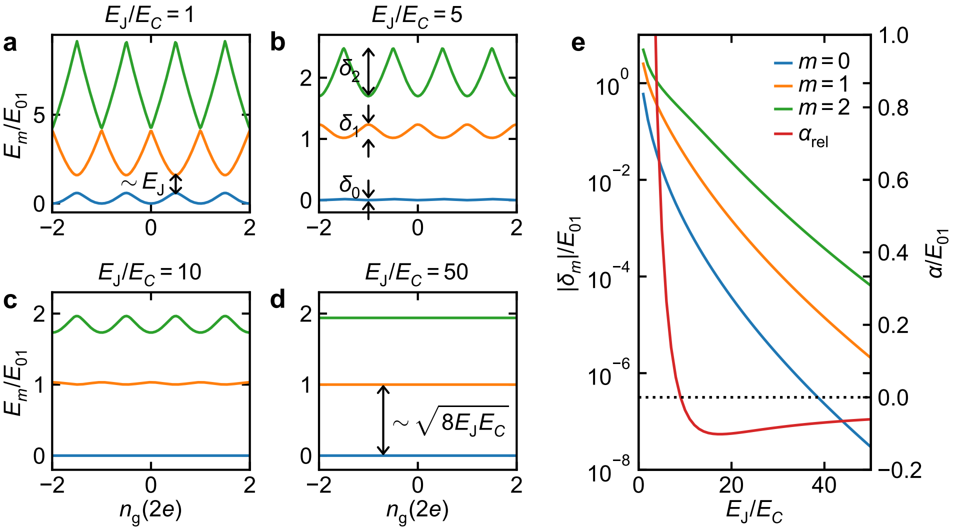

Figure 2.13: **Energy spectrum of superconducting island charge qubits** with **a** $E_J/E_C = 1$, the CPB regime, **b** $E_J/E_C = 5$, **c** $E_J/E_C = 10$ and **d** $E_J/E_C = 50$, the transmon regime. **a-d** demonstrate the flattening of the charge dispersion and the decrease in anharmonicity due to charge delocalisation with increasing E_J/E_C. The fundamental qubit transition energy at the sweet point ($n_g = m + 1/2$ with m an integer) starts as $\sim E_J$ and evolves to be E_C-dependent with increasing E_J/E_C to $\sim \sqrt{8E_JE_C}$. **e** Charge dispersion $|\delta_m|$ for the first 3 levels plotted together with the relative anharmonicity αrel $= \alpha/E_{01}$ at $n_g = 1/2$ as function of E_J/E_C. δ_m follow a rapid exponential decreasing trend while α shows only a slow trend towards zero (the ”anharmonicity barrier”) for $E_J/E_C > 20$. Adapted from [32].

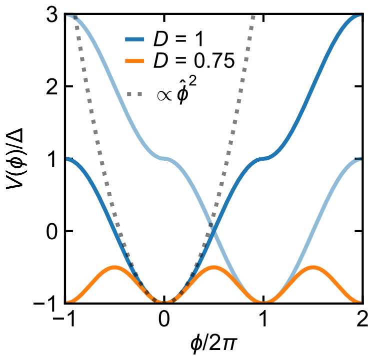

Figure 2.14: **Josephson potential in a ballistic SNS JJ with transparency $D = 1$.** Through the expense of quasiparticles the phase across the junction can exceed 2π, counteracting the formation of Bloch bands and the associated Coulomb blockade. The Josephson potential to a first approximation even be viewed as a harmonic potential. Adapted from [33].

2.4.4. Gatemon

Nowadays the fabrication of conventional in-situ double angle evaporated tunnel junctions allows for reliably targeted Josephson couplings. When more freedom or more precise targetting is needed the JJ can be replaced by a split JJ, a SQUID. Making the qubit frequency flux tunable, but it introduces flux noise. Another approach to realise on-chip qubit frequency control is to utilize semiconductor JJs that allow for electrostatic control of the Josephson coupling via nearby gates. Hence such transmons are dubbed gatemons. As described in Section 2.2.2, the mechanisms mediating the supercurrent in SIS and SNS structures are of different origin. Where the SIS JJ can be described as many tunnelling channels with low transparencies, the SNS JJ generally consists of a few Andreev bound states that can be highly transparent. In ballistic JJs where $D \to 1$, high coupling to the reservoir is reached at relatively low E_J. The quantum fluctuations of the free moving charges break down charge quantization and suppress the associated Coulomb blockade. Consequently this leads to the suppression of charge dispersion, the manifestation of Coulomb blockade in a transmon configuration, and a suppression of the anharmonicity.

For a more thorough understanding beyond this phenomenological intuition we need to consider the impact of the Josephson potential describing ABS modes. For the extreme case where $D = 1$ the system is fully ballistic and due to the lack of a scattering center there is no coupling between opposite moving branches. The phase difference ϕ between the two condensates is 4π-periodic and the phase is bound between 0 and 2π. However, at the expense of creating quasiparticles in the leads ϕ can increase beyond $\phi = 2\pi m$ where m being an integer. This breaks the periodicity in the energy spectrum (Figure 2.14) and prevents the formation of Bloch bands that give rise to Coulomb blockade, and thus the charge dispersion is completely suppressed. The aperiodic Josephson potential shows similarity with a harmonic potential, hence suppressing also the anharmonicity. The following paragraphs quantify these effects in the limit $D \to 1$.

Charge dispersion suppression

The slightest coupling between the two opposing branches opens up an avoided crossing at $\phi = \pi m$ with m being an integer, restoring the Bloch band structure and its periodicity. The magnitude of the avoided crossing scales according to $2\Delta\sqrt{1-D}$ (Section 2.2.2). When $D \simeq 1$ Landau-Zener (LZ) transitions can excite the ABS counteracting the periodic nature. Even though the phase is not externally driven, the probability of LZ-tunnelling into the excited ABS branch becomes significant at very high D, making the 4π LZ-tunnelling dominant over the dissipative 2π LZ-tunnelling. Hence the amplitude of the Coulomb blockade oscillations depends on the probability p of staying in the ground state periodic branch of the Josephson potential energy. In the regime $\Delta \gg E_C, k_{\mathrm{B}}T$ given by [33]:

$$p = \frac{1}{\Gamma(\lambda)}\sqrt{\frac{2\pi}{\lambda}}\left(\frac{\lambda}{e}\right)^{\lambda}, \quad \lambda \equiv \frac{1-D}{2}\sqrt{\frac{\Delta}{E_C}} \tag{2.38}$$

where Γ is the Gamma function. The charge dispersion is proportional to the Coulomb blockade amplitude and thus proportional to p. For the fundamental energy level the charge dispersion is given by:

$$\delta_0^{\mathrm{ABS}} = \Delta b D p \left(\frac{E_C}{2\pi^2\Delta D}\right)^{\frac{1}{4}} e^{-a\sqrt{\Delta D/E_C}} \tag{2.39}$$

where the numerical factors a and b are dependent on the transparency where for $D \ll 1$: $a = 2\sqrt{2}$ and $b = 4$ and for $D \to 1$: $a = 8\left(\sqrt{2}-1\right) + (1-D)\ln\sqrt{1-D}$ and $b = 8\left(\sqrt{2}-1\right)$. Resulting in a steadily decrease of the charge dispersion for the intermediate regime followed by a rapid suppression for $D \simeq 1$. Recent advances in the fabrication of ballistic nanowire SNS JJs enabled the measurement of this rapid charge dispersion suppression demonstrating the very high D regime [34].

Anharmonicity suppression

To quantify the anharmonicity suppression for $D \to 1$ we need to replace the sinusoidal Josephson potential energy, $V_{\mathrm{SIS}}\left(\hat{\phi}\right) = -E_{\mathrm{J}}\cos\hat{\phi}$, by the Josephson potential describing the collection of i Andreev bound states in the ground state:

$$V_{\mathrm{SNS}}\left(\hat{\phi}\right) = -\Delta\sum_i\sqrt{1 - D_i\sin^2\left(\hat{\phi}/2\right)} \tag{2.40}$$

Expanding $V_{\mathrm{SNS}}\left(\hat{\phi}\right)$ in $\hat{\phi}$ to the forth order leads to the approximation [35]:

$$V_{\mathrm{SNS}}\left(\hat{\phi}\right) \approx \frac{\Delta}{4}\sum_i\left(\frac{D_i}{2}\hat{\phi}^2 + \frac{D_i}{24}\left(1 - \frac{3}{4}D_i\right)\hat{\phi}^4\right) \tag{2.41}$$

$$= E_{\mathrm{J}}\frac{\hat{\phi}^2}{2} - E_{\mathrm{J}}\left(1 - \frac{3\sum_i D_i^2}{4\sum_i D_i}\right)\frac{\hat{\phi}^4}{24} \tag{2.42}$$

where the constant term has been omitted and $E_\mathrm{J} = \frac{\Delta}{4}\sum_i D_i$. The first term can be recognised as the contribution of an harmonic oscillator and the second term can be viewed as a perturbation such that the full Hamiltonian is described by:

$$\hat{H}_\mathrm{ABS} \approx 4E_C\left(\hat{n} - n_\mathrm{g}\right)^2 + V_0\left(\hat{\phi}\right) + V_0'\left(\hat{\phi}\right) \tag{2.43}$$

with $V_0\left(\hat{\phi}\right) = E_\mathrm{J}\frac{\hat{\phi}^2}{2}$ followed by the pertubative term $V_0'\left(\hat{\phi}\right) = -E_\mathrm{J}\left(1 - \frac{3\sum_i D_i^2}{4\sum_i D_i}\right)\frac{\hat{\phi}^4}{24}$. The pertubation matrix elements $\langle i|V_0'\left(\hat{\phi}\right)|i\rangle$ give:

$$\alpha \approx -E_C\left(1 - \frac{3\sum_i D_i^2}{4\sum_i D_i}\right) \tag{2.44}$$

In the SIS limit where $D_i \to 0$ for all i, we see the anharmonicity approaches $\alpha \approx -E_C$ as described in [32]. In the SNS limit finite D_i reduces the anharmonicity as observed experimentally [35] with a maximal suppression of $\alpha \simeq -E_C/4$ for $D_i = 1$.

2.4.5. Majorana Transmon

As described in Section 2.1.3, a semiconducting NW JJ with spin-orbit coupling can be driven into the topological regime by applying an external magnetic field. In a NW transmon architecture this results in a NW transmon with a topological junction. The quantum description of such a circuit should now include the fermionic state arising from the hybridization of the MZMs localized near the junction. As depicted in Figure 2.15a, the JJ in the resulting equivalent circuit diagram is not only shunted by a capacitive coupling but also shunted by a topological coupling through this hybridization.

To inspect the effect on relevant device parameters we study the energy band structure. For this we make two simplifications in the Hamiltonian. First we neglect the effect of V_SNS and assume the validity of V_SIS, which is proven to be justified up to a first order approximation in Section 2.4.4. Secondly we assume the couplings between the distant outer MZMs to be negligible. Which is a valid approximation when the topological segment length L_T is much longer than the topological phase coherence length ξ_T as couplings are suppressed exponentially in $\xi_\mathrm{T}/L_\mathrm{T}$. The topological phase coherence length is predicted to be $\xi_\mathrm{T} \simeq 500\,\mathrm{nm}$ [36], validating the simplification for the transmon in Chapter 6 where $L_\mathrm{T} \equiv 2\,\mu\mathrm{m}$, as defined by the plunger gates.

The Hamiltonian to be considered is then of the form $\hat{H} = \hat{H}_\mathrm{T} + \hat{H}_\mathrm{M}$ and consists of the standard transmon Hamiltonian based on V_SIS and an additional term that describes the coupling between the inner MZMs [37]:

$$\hat{H} = 4E_C\left(\hat{n} - n_\mathrm{g}\right)^2 - E_\mathrm{J}\cos\left(\hat{\phi}\right) + E_\mathrm{M} i\hat{\gamma}_2\hat{\gamma}_3\cos\left(\hat{\phi}/2\right) \tag{2.45}$$

where $\hat{\gamma}_2$ and $\hat{\gamma}_3$ are the MZMs at either side of the JJ as represented in Figure 2.15a and $E_\mathrm{M} = \Delta_\mathrm{T}\sqrt{D}$ is the coupling between the Majorana excitations, set by the topological superconducting gap Δ_T and the transparency D of the channel previously to turning topological.

Previously coherent transfer across the JJ was only allowed in the form of Cooper pairs guaranteeing that the charge parity, the total number of charges in the system,

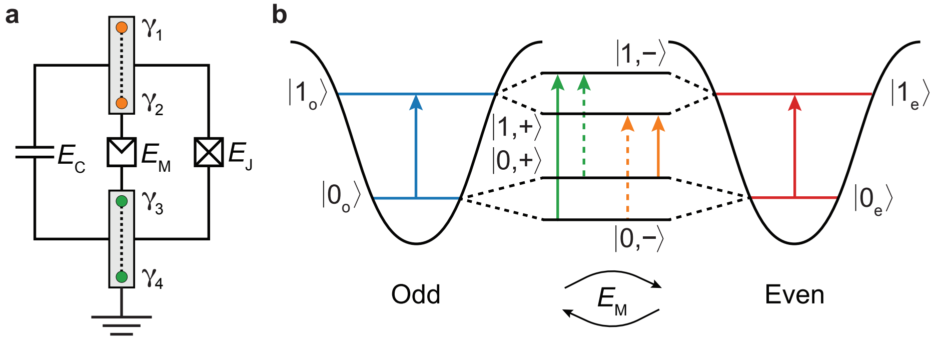

Figure 2.15: **Schematic representation Majorana transmon a** Equivalent circuit diagram of the Majorana transmon, where the JJ is replaced by a topological JJ. MZMs (γ_i) are introduced at the end of the topologically non-trivial sections. The hybridization of γ_2 and γ_3 add a coupling E_M between island and ground. **b** The ″odd″ (left) and ″even″ (right) charge parity potential wells are coherently coupled through E_M (middle). This allows for previously forbidden parity non-preserving transitions between the energy doublets (dashed arrows) on top of the parity preserving transitions (solid arrows). Adapted from [37].

to remain an even or odd number. In the standard transmon model the even and odd parity branch are two independent solutions of the Hamiltonian, differing only by half a period in n_g. The allowed transitions in this system can then be denoted as $|0_o\rangle \rightarrow |1_o\rangle$ and $|0_e\rangle \rightarrow |1_e\rangle$, where $|0,1\rangle$ are the transmon eigenstates and the subscripts o and e denote the parity of the superconducting island. In the non-trivial topological transmon case coherent single-electron transfer across the junction is facilitated by the hybridized fermionic state, coupling the two charge parity solutions. Figure 2.15b depicts schematically the two different charge parity potential wells; ″odd″ (left) and ″even″ (right) and the newly introduced transitions (middle). The coherent mixing of the two wells, through the E_M-coupling term, creates energy doublets with four allowed transitions; $|0,-\rangle \rightarrow |1,-\rangle$, $|0,+\rangle \rightarrow |1,+\rangle$ and the previously forbidden parity non-preserving transitions $|0,-\rangle \rightarrow |1,+\rangle$ and $|0,+\rangle \rightarrow |1,-\rangle$ where $|-,+\rangle$ denotes the state of the Majorana parity qubit. Like any qubit the Majorana transmon is encoded in the two lowest energy levels. Which now originate from the two independent ground state solutions of the trivial transmon counterpart. However, because there is no direct transition between the states of the same energy doublet this Majorana parity qubit can not be operated separately from the transmon eigenstates. Meaning that even though the system contains a topological junction the Majorana transmon is a non-topological qubit because of its non-topological operations. The importance of this design lies in the unique spectroscopic signatures of the charge-neutral Majorana states that are provided by the additional transitions. The spectroscopic features allow for quantification of E_M and demonstrate the coherent and tunable control over the parity state.

To investigate the parameter space over which these unique signatures are measurable we study the energy level spectra and the corresponding transition frequency spectra for $E_\mathrm{J} = 4\,\mathrm{GHz}$, $E_C = 0.8\,\mathrm{GHz}$ with increasing E_M. E_J is chosen to be representative at finite magnetic fields and conform with previous recordings in literature [38]. E_C is matched accordingly for a plasma oscillation frequency around 4 GHz. Figure 2.16a-c

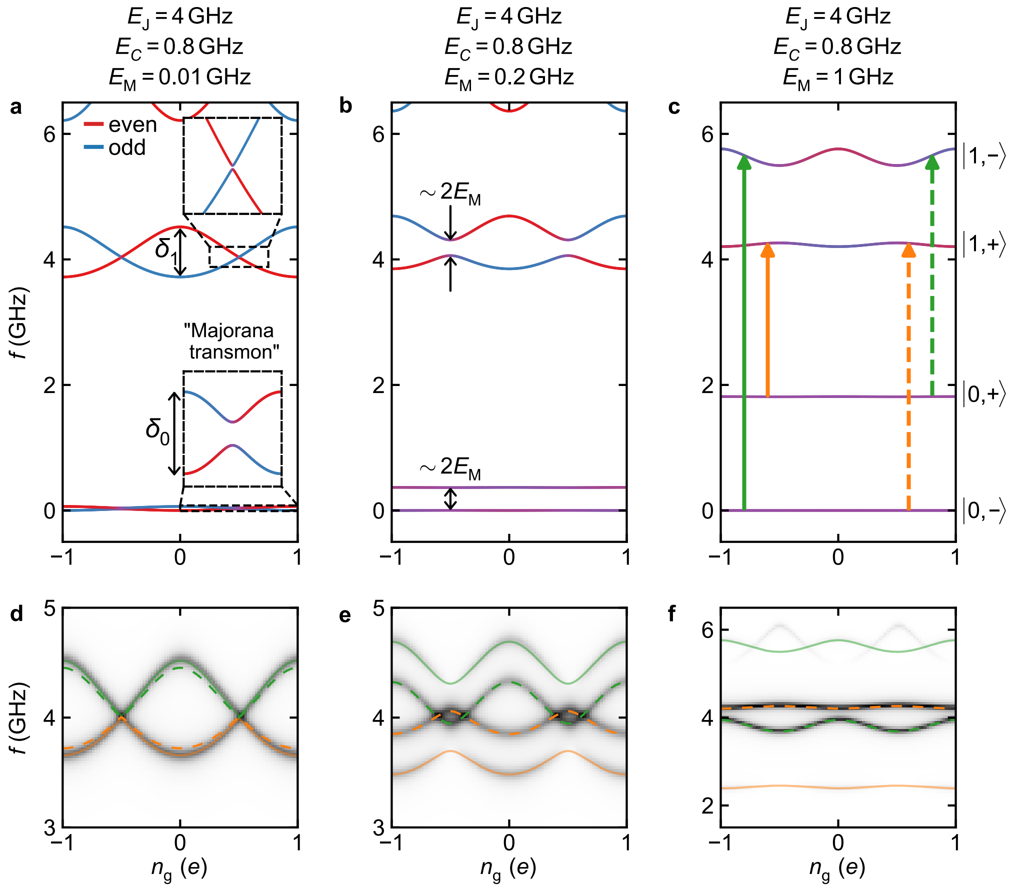

Figure 2.16: **Majorana transmon energy and spectroscopic spectra** for $E_J = 4$ GHz, $E_C = 0.8$ GHz with increasing E_M. **a-c** Energy spectrum for three different E_M-coupling strengths (**a** $E_M = 0.01$ GHz, **b** $E_M = 0.2$ GHz and **c** $E_M = 1$ GHz) show the coupling between the "even" (red) and "odd" (green) parity branches. The avoided crossings are of the order $\sim 2E_M$ and split the former non-topological transmon levels in energy doublets, of which the ground state doublet can now be used as so-called Majorana transmon. The energy doublets flatten with increasing E_M, rendering the Majorana transmon charge insensitive when $2E_M > \delta_m$. Panel **c** shows the parity conserving (solid arrows) and parity non-preserving transitions (dashed arrows), corresponding to the schematic representation in Figure 2.15b. **d-f** The corresponding spectroscopic features are shown in grey, where the intensity indicates the relative strength of each transition through its dipole matrix element with a fixed Lorentzian lineshape with a fixed linewidth set to $\kappa = 0.1$ GHz. To emphasise and clarify the unique patterns the four transitions indicated in panel (c) are shown by the corresponding line styles. Increasing E_M increases the splitting between the parity preserving and non-preserving counterpart. At the same time the strength of the parity non-preserving transition increases when a larger E_M make these more probable.

show the energy spectra for $E_\mathrm{M} = 0.01, 0.2$ and 1 GHz, showing the effect of the $\sim 2E_\mathrm{M}$ avoided crossing in three different regimes; $2E_\mathrm{M} < \delta_0$, $\delta_0 \leq 2E_\mathrm{M} \leq \delta_1$ and $2E_\mathrm{M} \geq \delta_1$. The Majorana transmon is highly anharmonic when E_M is smaller than the plasma oscillation frequency $\sqrt{8E_\mathrm{J}E_C}$, which gives now the separation between the first and the second excited state. Increasing E_M reduces the anharmonicity and suppresses charge dispersion through the charge delocalisation, similar to how increasing E_J suppresses charge dispersion. Again this charge dispersion suppression is seen from the flattening of the energy levels, especially when $2E_\mathrm{M} > \delta_m$ such that the eigenstates are not good parity eigenstates anymore even away from half-integer n_g. The eigenstates have become superpositions of the even and odd parity, rendering the transmon insensitive to charge noise.

To inspect the effect of E_M on the experimentally observable transition frequency spectrum, the corresponding spectroscopic patterns are shown in Figure 2.16d-f, where the line styles correspond to the transitions depicted in Figure 2.15b and Figure 2.16c. For a more representative simulation the transitions are plotted to have a Lorentzian lineshape with linewidth $\kappa = 0.1$ GHz where the height, visualised by the grey color scale, denotes the relative transition probability based on the dipole matrix element $\langle i| N |j\rangle^2$. In the limit of $E_\mathrm{M} = 0$ GHz, we indeed recover the standard transmon spectroscopic pattern with both parity branches present. In the regime $2E_\mathrm{M} < \delta_0$, we see the parity non-preserving transitions split off from the regular pattern. However, as the grey colormap shows, the minimum E_M that can be resolved is set by κ and the visibility $\langle i| N |j\rangle^2$ of these transitions. For $\delta_0 \leq 2E_\mathrm{M} \leq \delta_1$ this splitting increases while the charge dispersion is almost unaffected, since it is predominantly set by the charge dispersion of the $|1, +\rangle$ and $|1, -\rangle$ levels. For this E_J all transitions have similar visibilty in this regime. When $2E_\mathrm{M} \geq \delta_1$ the Majorana imposed parity splitting keeps on increasing, but now the flattening of the charge dispersion becomes apparent in the spectroscopic features. Especially at higher $E_\mathrm{M}/E_\mathrm{J}$ ratios the tunable intensities with E_M become visible as the large splitting reveals the reduced invisibility of the parity preserving transitions.

Finite size effects

The topological phase coherence length has not been experimentally confirmed, and therefore it is important to study the finite size effect on the spectroscopic features. From Section 2.2.3 we know that the coupling between the two most outer MZMs, γ_1 and γ_4, destroys the 4π-periodic current phase relation, thereby destroying any topological features. However the limit of $E_\mathrm{M}^{1,4} \simeq 0$ does not exclude on-island non-zero coupling terms $E_\mathrm{M}^{1,2}$ and $E_\mathrm{M}^{3,4}$. The Hamiltonian incorporating the Majorana physics in such a case becomes [39]:

$$\hat{H}_\mathrm{M} = E_\mathrm{M}^{1,2} i\hat{\gamma}_1\hat{\gamma}_2 + E_\mathrm{M}^{3,4} i\hat{\gamma}_3\hat{\gamma}_4 + E_\mathrm{M}^{2,3} i\hat{\gamma}_2\hat{\gamma}_3 \cos\left(\hat{\phi}/2\right) \tag{2.46}$$

where $E_\mathrm{M}^{1,2}$ and $E_\mathrm{M}^{3,4}$ are the couplings between MZMs originating from the same pair and $E_\mathrm{M}^{2,3} = E_\mathrm{M}$ as previously discussed. Figure 2.17 shows the effect of on-island coupling in the case of $E_{=}4$ GHz, $E_C = 0.8$ GHz and $E_\mathrm{M}^{2,3} = 0.2$ GHz for $E_\mathrm{M}^{1,2} = E_\mathrm{M}^{3,4}$. The regime where $0 < E_\mathrm{M}^{1,2} < E_\mathrm{M}^{2,3}$ results in a skewed and $2e$-periodic spectra and only when $E_\mathrm{M}^{1,2} \geq E_\mathrm{M}^{2,3}$ the spectrum is indistinguishable from the standard transmon spectrum with parity jumps even though the origin of the transitions differ. This result stresses the need for maximizing the topological NW segments, it also demonstrates that the intermediate

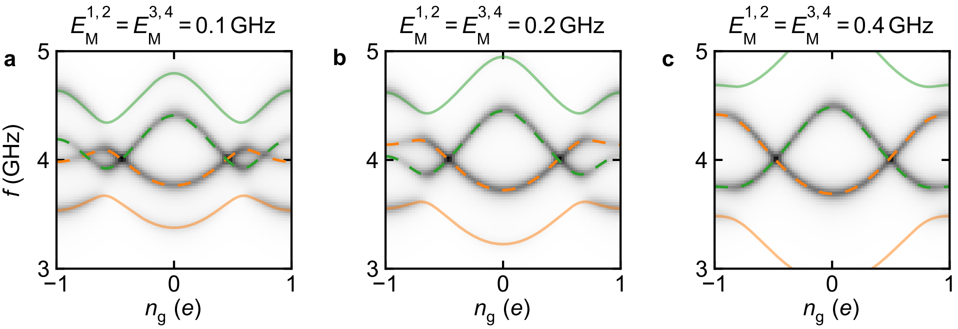

Figure 2.17: **Finite size effects in spectroscopic spectra** for E_J = 4 GHz, E_C = 0.8 GHz, $E_M^{2,3}$ = 0.2 GHz and **a** $E_M^{1,2} = E_M^{3,4}$ = 0.1 GHz, **b** $E_M^{1,2} = E_M^{3,4}$ = 0.2 GHz and **c** $E_M^{1,2} = E_M^{3,4}$ = 0.4 GHz. Where the spectroscopic spectrum becomes indistinguishable

regime still shows unique MZM features that can be used for solidifying the evidence for the presence of MZMs and the associated energy scales.

References

[1] Kamerlingh Onnes, H. Further experiments with liquid helium. c. on the change of electric resistance of pure metals at very low temperatures etc. iv. the resistance of pure mercury at helium temperatures. *Koninklijke Nederlandsche Akademie van Wetenschappen Proceedings* **13**, 1274–1276 (1911).

[2] Bardeen, J., Cooper, L. N. & Schrieffer, J. R. Theory of Superconductivity. *Phys. Rev.* **108**, 1175–1204 (1957).

[3] Tinkham, M. *Introduction to superconductivity* (Courier Corporation, 2004).

[4] Abrikosov, A. The magnetic properties of superconducting alloys. *Journal of Physics and Chemistry of Solids* **2**, 199–208 (1957).

[5] Court, N. A., Ferguson, A. J. & Clar, R. G. Energy gap measurement of nanostructured aluminium thin films for single Cooper-pair devices. *Superconductor Science and Technology* **21**, 015013 (2007).

[6] Meservey, R. & Tedrow, P. M. Properties of Very Thin Aluminum Films. *Journal of Applied Physics* **42**, 51–53 (1971).

[7] Coffey, M. W. & Clem, J. R. Unified theory of effects of vortex pinning and flux creep upon the rf surface impedance of type-II superconductors. *Phys. Rev. Lett.* **67**, 386–389 (1991).

[8] Brandt, E. H. Penetration of magnetic ac fields into type-II superconductors. *Phys. Rev. Lett.* **67**, 2219–2222 (1991).

[9] Mourik, V. *et al.* Signatures of Majorana Fermions in Hybrid Superconductor-Semiconductor Nanowire Devices. *Science* **336**, 1003–1007 (2012).

[10] Kitaev, A. Y. Unpaired Majorana fermions in quantum wires. *Physics-Uspekhi* **44**, 131–136 (2001).

[11] Nijholt, B. & Akhmerov, A. R. Orbital effect of magnetic field on the Majorana phase diagram. *Phys. Rev. B* **93**, 235434 (2016).

[12] Josephson, B. Possible new effects in superconductive tunnelling. *Physics Letters* **1**, 251–253 (1962).

[13] Anderson, P. W. & Rowell, J. M. Probable Observation of the Josephson Superconducting Tunneling Effect. *Phys. Rev. Lett.* **10**, 230–232 (1963).

[14] Beenakker, C. W. J. Universal limit of critical-current fluctuations in mesoscopic Josephson junctions. *Phys. Rev. Lett.* **67**, 3836–3839 (1991).

[15] Golubov, A. A., Kupriyanov, M. Y. & Il'ichev, E. The current-phase relation in Josephson junctions. *Rev. Mod. Phys.* **76**, 411–469 (2004).

[16] Bretheau, L. *Localized Excitations in Superconducting Atomic Contacts: PROBING THE ANDREEV DOUBLET.* Ph.D. thesis, Ecole Poly- technique X (2013). Mesoscopic Systems and Quantum Hall Effect [cond-mat.mes-hall].

[17] San-Jose, P., Prada, E. & Aguado, R. ac Josephson Effect in Finite-Length Nanowire Junctions with Majorana Modes. *Phys. Rev. Lett.* **108**, 257001 (2012).

[18] Fu, L. Electron Teleportation via Majorana Bound States in a Mesoscopic Superconductor. *Phys. Rev. Lett.* **104**, 056402 (2010).

[19] Ohm, C. & Hassler, F. Majorana fermions coupled to electromagnetic radiation. *New Journal of Physics* **16**, 015009 (2014).

[20] Schuster, D. *Circuit Quantum Electrodynamics*. Ph.D. thesis, Yale University (2007).

[21] Blais, A., Huang, R.-S., Wallraff, A., Girvin, S. M. & Schoelkopf, R. J. Cavity quantum electrodynamics for superconducting electrical circuits: An architecture for quantum computation. *Phys. Rev. A* **69**, 062320 (2004).

[22] Wallraff, A. *et al.* Strong coupling of a single photon to a superconducting qubit using circuit quantum electrodynamics. *Nature* **431**, 162–167 (2004).

[23] Anonymous. Spontaneous emission probabilities at radio frequencies. *Phys. Rev.* **69**, 674–674 (1946).

[24] Blais, A., Girvin, S. M. & Oliver, W. D. Quantum information processing and quantum optics with circuit quantum electrodynamics. *Nature Physics* **16**, 247–256 (2020).

[25] Göppl, M. *et al.* Coplanar waveguide resonators for circuit quantum electrodynamics. *Journal of Applied Physics* **104**, 113904 (2008).

[26] Kroll, J. *Magnetic field compatible hybrid circuit quantum electrodynamics*. Ph.D. thesis, Delft University of Technology (2019).

[27] devoret, M. H. & Martinis, J. M. Implementing Qubits with Superconducting Integrated Circuits. *Quantum Information Processing* **3**, 163–203 (2004).

[28] Armour, A. D., Blencowe, M. P., Brahimi, E. & Rimberg, A. J. Universal Quantum Fluctuations of a Cavity Mode Driven by a Josephson Junction. *Phys. Rev. Lett.* **111**, 247001 (2013).

[29] Meister, S. *et al.* Resonators coupled to voltage-biased Josephson junctions: From linear response to strongly driven nonlinear oscillations. *Phys. Rev. B* **92**, 174532 (2015).

[30] Simon, S. H. & Cooper, N. R. Theory of the Josephson Junction Laser. *Phys. Rev. Lett.* **121**, 027004 (2018).

[31] Cassidy, M. C. *et al.* Demonstration of an ac Josephson junction laser. *Science* **355**, 939–942 (2017).

[32] Koch, J. *et al.* Charge-insensitive qubit design derived from the Cooper pair box. *Phys. Rev. A* **76**, 042319 (2007).

[33] Averin, D. V. Coulomb Blockade in Superconducting Quantum Point Contacts. *Phys. Rev. Lett.* **82**, 3685–3688 (1999).

[34] Bargerbos, A. *et al.* Observation of Vanishing Charge Dispersion of a Nearly Open Superconducting Island. *Phys. Rev. Lett.* **124**, 246802 (2020).

[35] Kringhöj, A. *et al.* Anharmonicity of a superconducting qubit with a few-mode Josephson junction. *Phys. Rev. B* **97**, 060508 (2018).

[36] Antipov, A. E. *et al.* Effects of Gate-Induced Electric Fields on Semiconductor Majorana Nanowires. *Phys. Rev. X* **8**, 031041 (2018).

[37] Ginossar, E. & Grosfeld, E. Microwave transitions as a signature of coherent parity mixing effects in the Majorana-transmon qubit. *Nature Communications* **5**, 4772 (2014).

[38] Zuo, K. *et al.* Supercurrent Interference in Few-Mode Nanowire Josephson Junctions. *Phys. Rev. Lett.* **119**, 187704 (2017).

[39] Keselman, A., Murthy, C., van Heck, B. & Bauer, B. Spectral response of Josephson junctions with low-energy quasiparticles. *SciPost Phys.* **7**, 50 (2019).

3

Fabrication and experimental methods

The handling of high-frequency superconducting quantum structures requires purpose-built experimental methods, including nanofabrication, cooling to milliKelvin temperatures, shielding from background radiation and high-bandwidth phase locked measurement readout schemes. This chapter provides a compact overview of the most essential details of the experimental methods specific to the research in the following chapters.

3.1. Fabrication details

Experiments of quantum effects in engineered artificial atoms requires extreme high precision and clean fabrication techniques. In this thesis the focus lies on hybrid Josephson junction-based devices that combine both top-down nanofabrication processes, see Figure 3.1, together with more specialized deposition methods of bottom-up grown mate-

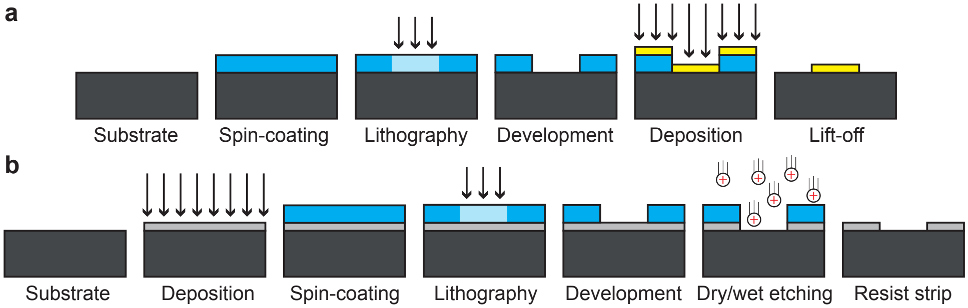

Figure 3.1: **Schematic illustration of top-down fabrication processes. a** A positive-tone polymer is used as a mask to ensure deposited material only remains at the exposed areas after lift-off. **b** A positive-tone polymer is used to transfer the inverse pattern by an etching process into the deposited material layer.

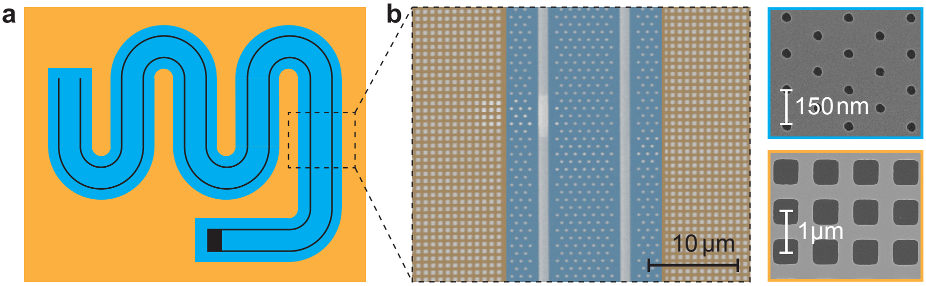

Figure 3.2: **Artificial pinning hole patterning.** **a** Sketch indicating the pattern regions, where the sensitive area is patterned with a fine hole lattice (blue) and the ground plane is patterned with a coarse hole pattern (orange) to save writing time which minimizes drifts. **b** False-colored scanning electron microscope (SEM) image of a patterned resonator and zoomed in SEMs indicating the lattice pitch of both patterns.

rials. Below we summarise highly specialised fabrication efforts and deposition techniques that are crucial to the success of the experiments in this thesis.

3.1.1. Magnetic field compatible coplanar waveguide resonators

The fabrication of coplanar waveguide (CPW) resonators is central to this thesis and follows the standard etching process steps illustrated in Figure 3.1b. First the wafer, made from intrinsic Si (Chapter 4), sapphire (Chapter 5) or Si/SiN$_x$ (Chapter 6 and 7) is cleaned with nitric acid. Subsequently, the base layer is sputtered in a high vacuum chamber ($p_{\mathrm{base}} \sim 10^{-9}$ mTorr) onto the wafer from a 3 inch 99.99% pure Nb$_{0.7}$Ti$_{0.3}$ target in an Ar/N$_2$ atmosphere. A typical 100 nm film has a critical temperature of ~ 14 K, a resistivity of ~ 123 µΩ cm and stress of ~ 400 MPa. The resonators are patterned by electron beam lithography (EBL) in the positive-tone resist CSAR 62. After development the pattern is transferred into the NbTiN layer by an reactive ion etch (RIE) process in a SF$_6$/O$_2$ atmosphere. The selectivity ensures that the pattern is only transferred into the NbTiN layer. The left-over resist is stripped thoroughly in hot photo-resist stripper. Additional circuitry is fabricated afterwards to guarantee the pristine interface of the CPW with the wafer, as dirt and residues introduce two-level systems interfering with the CPWs electromagnetic field resulting in increasing internal losses. Finally the sample is diced to the exact dimensions of the slot in the printed circuit board (PCB), in our case 2 × 7 mm. A thick photoresist is applied to protect the sample during the dicing process against the on-chip deposition of residual dicing materials. Cleaning off the protective resist finalizes the CPW fabrication and the sample can now be placed in the PCB to interface it with the experimental setup (See Section 3.2).

To make the CPW resonators magnetic field compatible they are patterned with a lithographically defined pinhole lattice that is applied simultaneously during the resonator fabrication (Figure 3.2) [1].

3.1.2. Selective hBN-encapsulated graphene transfer

The incorporation of a graphene-based Josephson junction in a superconducting microwave circuit requires circuit QED compliant methods. This means that the use of

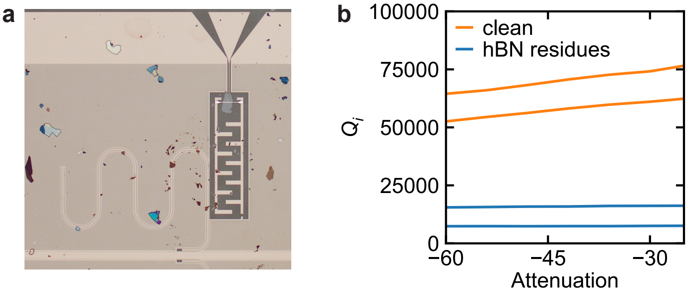

Figure 3.3: **Loss tangient measurements of hBN residues.** **a** Optical microscope image showing the excess deposited exfoliated material, primarily hBN and possibly also graphite. **b** Intrinsic quality factor measurements demonstrating the importance of a clean transfer process onto the circuit QED chip.

lossy dielectric materials needs to be minimized, residues need to be contained and loss channels need to be prevented by reducing the number of gates and electrodes. Previously ballistic graphene Josephson junctions have been realised in current annealed suspended structures and by encapsulation in hexagonal boron nitride (hBN) [2, 3]. Even though the suspended graphene junction circumvents the use of any dielectrics, the annealing process requires electrodes for current annealing rendering this technique unfavourable. Therefore the graphene Josephson junctions in Chapter 4 were made following the fabrication process of hBN encapsulation by deterministic and low-residue all-dry viscoelastic stamping [4]. hBN has shown to be an appealing substrate because of its atomically smooth surface with a lattice constant similar to that of graphite, resulting in graphene devices with increased electronic properties [5]. Furthermore the single crystal material is relatively free of dangling bonds and charge traps. Nevertheless, Figure 3.3 demonstrates that residual hBN flakes from a non-selective stack transfer cause measurable intrinsic losses. Hence we follow the fabrication process as described in [3] with the minor adjustment of using PMMA instead of an MMA/MAA copolymer and with an additional etch step enabling the transfer of only the designated heterostructure to the circuit QED chip, see Figure 3.4 and Figure 3.5. Both modifications are implemented to reduce residues of polymers and unwanted hBN and graphene flakes that adversely affect the microwave performance of our devices.

The fabrication starts with the mechanical exfoliation of both graphite and hBN crystals using blue Nitto tape onto the carrier substrates. The carrier for the bottom hBN is a Si/(285 nm)SiO_2 chip with marker field that is thoroughly cleaned in nitric acid. The carrier for graphene is a cleaved Si substrate with only 90 nm thermally grown SiO_2 that is cleaned in nitric acid. The reduced SiO_2 thickness enhances the visibility of the color tones of thin graphite flakes. The second hBN carrier is prepared from a microscope glass slide such that the flakes can be aligned optically in the pick-up/transfer process. A $1 \times 1\ \mathrm{cm}^2$ PDMS film is placed on the microscope slide that provides the right elasticity during the all-dry viscoelastic stamping. The stickiness of the PDMS does not allow for the transfer of any materials and is therefore spin-coated with a layer of PMMA. For the assembly of the van der Waals heterostructure the glass slide is mounted on an XYZ stage and the material to be picked up or transferred onto is placed on an XYθ stage that

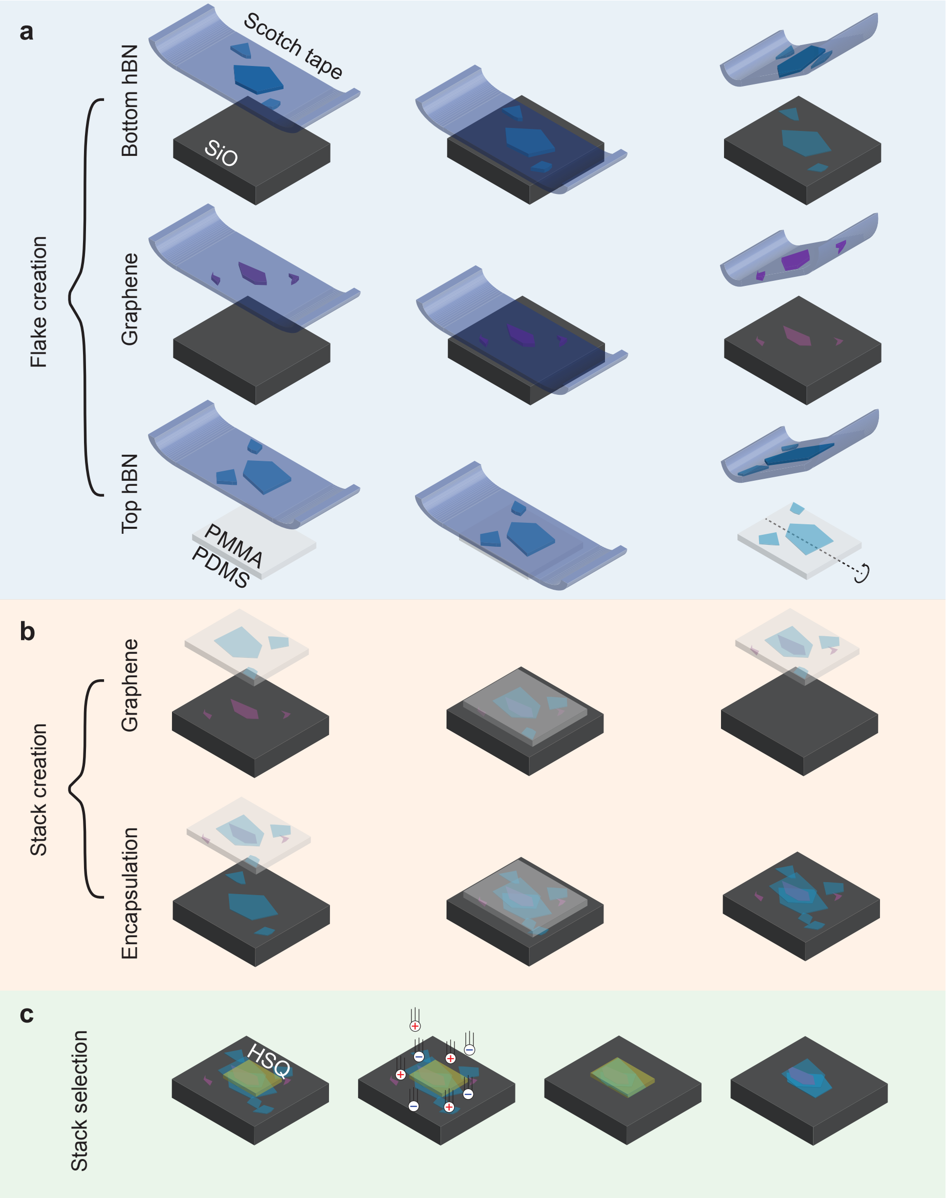

Figure 3.4: **Assembly and selection of the hexagonal boron nitride (hBN)-encapsulated superconductor-graphene-superconductor (S-G-S) Josephson junction.** **a** Exfoliated flakes of hBN and graphite are deposited either on a SiO chip or glass plate with PMMA-covered PDMS. **b** Using an optical microscope the flakes can be aligned through the transparent PMMA-covered PDMS and heterostructures can be assembled by pick-up or transfer based on the van der Waals force. **c** A selective dry reactive ion etch removes surrounding excess flakes while the stack is protected by an HSQ hard mask. The HSQ is removed with a wet-etch while the stack is still protected by a thin PMMA layer underneath the HSQ, that is finally dissolved in hot acetone. Adapted from [6].

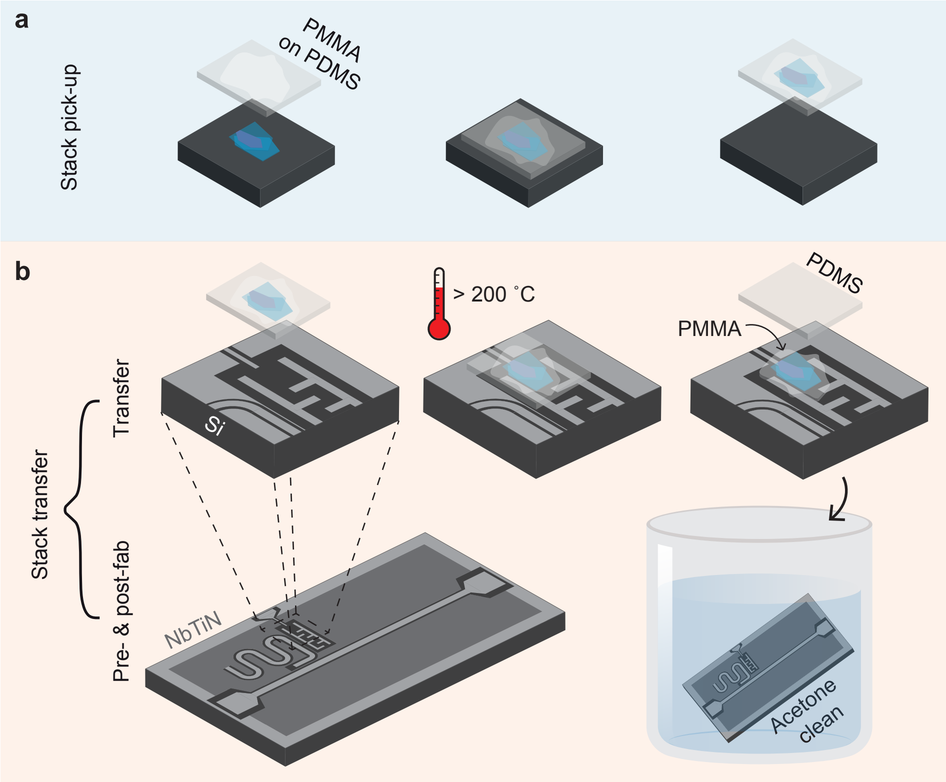

Figure 3.5: **Clean transfer of hBN-encapsulated graphene onto circuit QED chip. a** The stack is picked up using the same dry PMMA polymer-based technique. **b** The transfer however is accomplished through burning the polymer onto the chip. To enhance the adhesion of the heterostructure the chip is kept on a hot plate at 100 °C for over 30 minutes with a weight on top after which the PMMA is dissolved in hot acetone.

is equipped with a heater. Both stages allow for the alignment of the two layers through an optical microscope. The van der Waals forces between the flakes, substrate and PMMA can be modulated by the applied pressure, temperature, shear force and retraction velocity. The right combination allows for deterministic pick-up or transfer. The ability to transfer the stack to a second substrate, as desired when embedding the encapsulated graphene in a circuit QED scheme, depends on the van der Waals forces the substrate can facilitate. In our case the transfer was not possible by deterministic stamping and the stack had to be melted onto the chip with the PMMA, transferring also the surrounding flakes. Removing these flakes by a dry reactive ion etch (RIE) aftwards would harm the NbTiN circuitry and therefore an extra step was included in the fabrication removing the surrounding flakes before the transfer to the circuit QED chip, see Figure 3.4. In this step the stack is protected by thin PMMA layer with an HSQ hard mask on top. The HSQ mask is transferred into the PMMA with an O_2 RIE after which the hBN residues are etched away using an SF_6/He/O_2 RIE etch. Finally, the HSQ is removed with a 25 s 1:7 buffered HF wet etch. Dissolving the underlying PMMA in acetone reveals the now isolated heterostructure.

3.1.3. Semiconducting nanowire Josephson junctions

At the heart of the devices in Chapters 5, 6 and 7 lies a semiconductor nanowire Josephson junction made from bottom-up grown nanowires. In this thesis mainly InAs nanowires with epitaxial two-faceted Al shell are used [7]. Chapter 6 also includes some first efforts in the incorporation of InSb nanowires with epitaxial two-faceted Al shell [8]. Epitaxial InAs-Al NWs has been the standard material in this thesis because the NWs can be grown longer, yield and precision of the transfer is higher and post-transfer nanofabrication is easier. But the higher spin-orbit of InSb makes the InSb-Al material the preferred platform for topological devices, since lower external magnetic fields are required to drive the system topologically non-trivial. Table 3.1 shows a comparison of the properties of both materials.

Especially the lowered allowed processing temperature for InSb-Al demands different processing standards than the already established procedures for InAs-Al. For InSb-Al NWs that have been exposed to elevated temperatures superconductivity has been observed to disappear. Experimental and theoretical studies on the InSb-Al interface have

Material	InAs-Al	InSb-Al
$\lvert g_{\text{bulk}}\rvert$	~15 [9]	~50 [10]
$\lvert g_{\text{NW}}\rvert$	~4.1 to 34 [11]	~5.5 to 11 [12]
length	~8 µm to 12 µm	~2 µm to 4 µm
diameter	70 nm to 150 nm	70 nm to 150 nm
JJ fabrication	EBL defined wet etch	In-situ shadow evaporation
JJ minimum width	~70 nm	~70 nm
JJ placing precision	~50 nm	~500 nm
NW deposition	Optical microscope	Scanning electron microscope
Processing temperatures	$< 300\,^{\circ}$C	$< 20\,^{\circ}$C

Table 3.1: **Comparison InAs-Al versus InSb-Al material properties.**

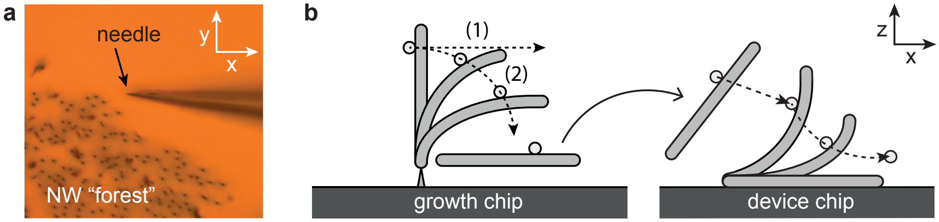

Figure 3.6: **Nanowire deposition by micromanipulation.** **a** Optical microscope image of a NW growth chip viewed from the top, where NWs are visible as black dots. The needle is used to pick up and transfer NWs. **b** Schematic illustration depicting possible trajectories for collecting (left) and depositing (right) the NW. Adapted from [16].

demonstrated that the interface is unstable and forms AlSb clusters through the temperature stimulated exchange reaction of aluminium atoms with indium atoms [13, 14], destroying the epitaxial interface and the induced superconductivity. Consequently, elevated temperatures during the post growth fabrication should be avoided. Resist hardening is attained through outgassing in vacuum, lift off an resist stripping has to be done in room temperature solutions and heating during processes should be avoided by stepwise processing interleaved with cool down times. Below the different contacting processes for InAs-Al and InSb-Al NWs are described in more detail.

Nanowire deposition

The assembly of devices incorporating bottom-up grown materials into a top-down fabrication process is not straightforward. Various methods have been developed for the deposition of semiconducting nanowires. However the high-precision control together with the low-contamination of the labour intensive micromanipulator deposition technique is unsurpassed [15]. With this deposition technique a needle that is mounted on a micromanipulator stage is used to break off one of the NWs from the growth chip, see Figure 3.6a. By pushing against the NW as sketched in Figure 3.6b (left) the NW is released. Due to the van der Waals forces the NW sticks to the tip of the needle, enabling the transfer to another chip. The NW is released onto the surface of the device chip when the van der Waals forces with the chip surface exceed the forces with the needle. This is accomplished through a smearing motion exerted along the length of the NW to ensure straight deposition. For longer NWs this technique can be applied in an optical setup, but for shorter NWs the manipulator needs to be incorporated into an SEM.

Nanowire post-growth fabrication

Implementing NWs in cQED environments requires prefabricated resonator substrates as described in Section 3.1.1. Any bottomgates can be formed simultaneously from the same NbTiN layer during the RIE process. To electrostatically isolate the bottomgates 30 nm of SiN_x is put down by plasma-enhanced chemical vapor deposition (PECVD) and excess dielectric is removed by an HF wet etch. After the NWs have been transferred from the growth chip onto the device chip the processing differs slightly for the two materials, both schematically depicted in Figure 3.7. For both processes only polymers that can be removed by acetone are used, as the use of other solvents might harm the NW.

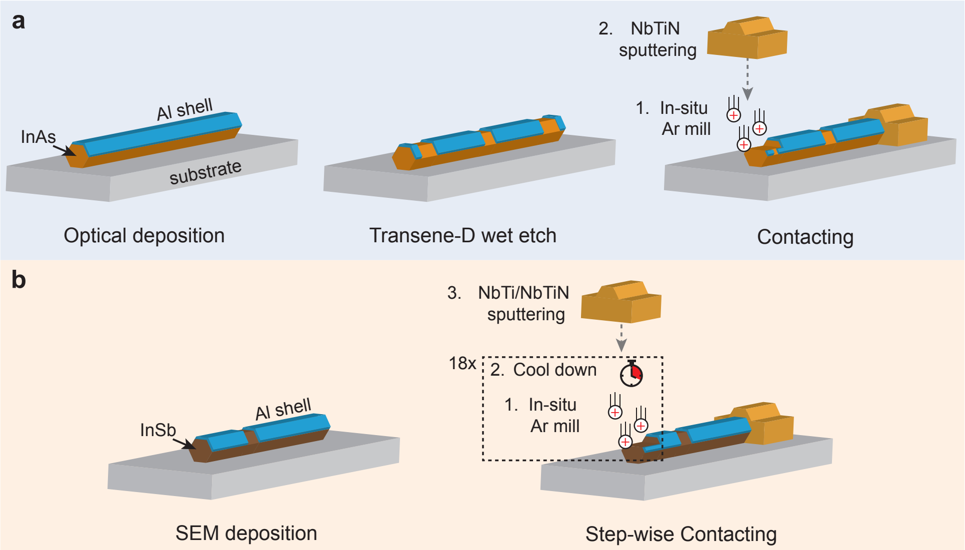

Figure 3.7: **Nanowire post-growth fabrication. a** An InAs NW with epitaxial Al shell is deposited using an optical micromanipulator setup. The Al shell is chemically removed at certain parts to either form a Josephson junction or prepare for contacting. The NW is contacted by an in-situ argon mill of the surface and subsequent metal deposition. **b** The InSb NW with epitaxial Al shell, that already has a Josephson junction due to shadow-evaporation, is placed using a micromanipulator in an SEM setup. Contacting the NW is done in steps to prevent heating of the NW, 20 s steps of argon milling are alternated with 20 s cool-down intervals. After the milling process the NW is contacted with sputtered NbTiN.

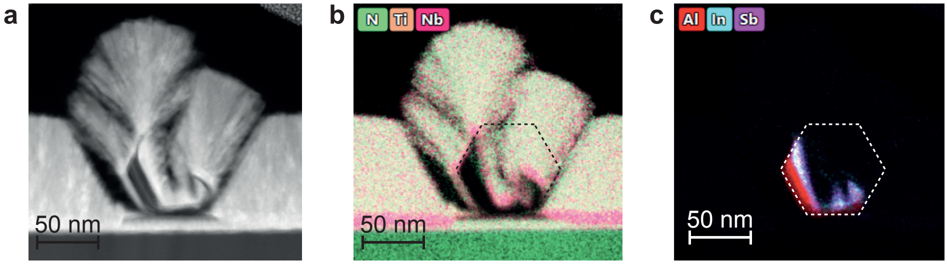

Figure 3.8: **Cross-sectional view contacts InSb nanowire.** **a** High-angle annular dark field tunnelling electron microscope image of an InSb NW contacted with NbTiN as described in the text. **b** Measurements of N, Ti and Nb concentrations across the cross-sectional. The NbTi sticking layer is recognized by the increased Nb concentration. The black dashed line is a guide to the eye illustrating the original hexagonal circumference of the NW. **c** Measurements of Al, In and Sb concentrations showing that the NW is almost completely etched by the Ar milling step. The Al shell seems to be more resilient to the Ar etch. TEMs by courtesy of Dr. E. Yücelen.

When handling InAs-Al NWs the Al shell has to be partially removed in order to form a JJ. The wet etch is done before applying contacts because of two reasons. Firstly, etching the JJ after the contacts are sputtered is less reliable as the standing edges can pierce through the polymer resulting in a leaky mask. Secondly, in this way we can already remove a part of the Al shell where the wire will be contacted to aid in a barrier free contact as the native oxide is hard to remove. The JJ and contact preparation windows are lithographically defined in PMMA resist and etched using transene-D. The etch is stopped with several baths of DI H_2O. Instead of stripping the junction mask a second coating of PMMA resist is applied on top in which a mask for the contacting step is written, to ensure that the positioning of the NW stays unaltered. The contacts are designed to be larger than the transene-D prepared areas and have overlap with the remaining Al shell. Prior to the metal deposition a 6 min in-situ on-chip Ar plasma etch is applied to open up a "fresh" part of the wire that has not been exposed to air to avoid any oxide barrier. The NW is then contacted to the prefabricated NbTiN circuitry with NbTiN by sputtering NbTi from a 99.99% pure target in an Ar/N_2 atmosphere.

For the InSb-Al case there is already a predefined JJ. Therefore the Al shell wet etch is omitted and the sample is immediately coated for contacting. The contacting windows are lithographically defined in a layer of vacuum hardened PMMA and the in-situ Ar mill is performed in 20 s steps interleaved with 40 s cool down periods to prevent heat built-up in the NW. After 18 cycles the NW is contacted first by a ~6 nm NbTi sticking layer followed by the usual NbTiN recipe. Tunnelling electron microscopy of the contacts reveals that the NWs are almost completely etched away during the argon mill, see Figure 3.8.

Additional topgates can be added. To help lifting off the dielectric and minimize the number of fabrication steps the dielectric and metal are deposited during the same lithography step using a PMMA mask. Which again is vacuum hardened at room temperature for the InSb-Al case as opposed to regular hot plate baking at 175 °C. 30 nm of SiNx is sputtered onto the sample in an Ar atmosphere, after which about 150 nm NbTiN is sputtered to form electrostatic gates. The NbTiN is once more sputtered from a 99.99% pure NbTi target in an Ar/N_2 atmosphere. The gates need to be superconducting to be compliant with cQED standards on loss channels.

Quasiparticle traps

The contacting of the InAs-Al NW in Chapter 5 was followed by a Ti/Au evaporation before lift off [17]. The Ti/Au layer on top of the superconducting NbTiN contact is expected to act as a normal metal sink to trap quasiparticles [18, 19]. A measure considered to be of particular benefit to the experiment due to the large sub-gap density of states in NbTiN.

3.2. Experimental set-up

Unless otherwise stated, all experiments were performed in an Oxford Triton dry dilution refrigerator with a base temperature of $T \simeq 20\,\mathrm{mK}$. The dilution fridges are equipped both with DC measurement lines and RF coaxial cabling enabling experiments that combine both DC transport and microwave frequency RF measurements simultaneously. Schematic overviews of the experiment specific electrical circuit at cryogenic and room temperature are provided in each chapter. The dilution refrigerators are also equipped with a fast exchange system and 3-axes vector superconducting magnets. The fast exchange system consists of a 'puck' holding the sample that can be inserted via a load lock and allows for sample exchanges at $T = 10\,\mathrm{K}$. After the puck has been attached to the mixing chamber the setup can reach base temperature overnight ($\sim$ 10 hours). The rapid exchange time is crucial for experiments on low-yield mesoscopic devices, however it complicates ESD-compliant loading methods and adversely affects radiative shielding as the puck and loading valves are not entirely light tight. On top of that, no radiative shield could be mounted colder than 700 mK to make place for the vector magnet. And the vector magnet also prevents the use of superconducting shielding right around the sample to expel stray flux.

3.2.1. Custom radiative shielding

To compensate for the missing shielding and leaky puck we enclose the sample in a milled copper box that is wrapped in non-magnetic microwrave absorbing Eccosorb-foam, copper tape and another layer of Eccosorb-foam. Lastly, the puck is coated with Aeroglaze Z306, a high thermal radiation absorbing spray paint.

References

[1] Kroll, J. *et al.* Magnetic-Field-Resilient Superconducting Coplanar-Waveguide Resonators for Hybrid Circuit Quantum Electrodynamics Experiments. *Phys. Rev. Applied* **11**, 064053 (2019).

[2] Mizuno, N., Nielsen, B. & Du, X. Ballistic-like supercurrent in suspended graphene Josephson weak links. *Nature Communications* **4**, 2716 (2013).

[3] Calado, V. E. *et al.* Ballistic Josephson junctions in edge-contacted graphene. *Nature Nanotechnology* **10**, 761–764 (2015).

[4] Castellanos-Gomez, A. *et al.* Deterministic transfer of two-dimensional materials by all-dry viscoelastic stamping. *2D Materials* **1**, 011002 (2014).

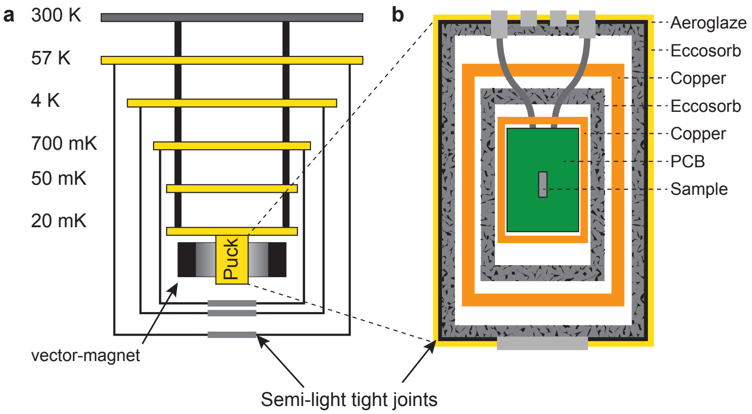

Figure 3.9: **Radiative shielding. a** Schematic of the different cold stages and radiative shielding of the Oxford Triton 400 dilution refrigerators. Due to the installed vector magnet there is no shield at the mixing chamber nor superconducting enclosures. **b** Shows the additional layers of copper and eccosorb in the nearly light-tight puck to reflect and absorb stray photons. Adapted from [6].

[5] Dean, C. R. *et al.* Boron nitride substrates for high-quality graphene electronics. *Nature Nanotechnology* **5**, 722–726 (2010).

[6] Kroll, J. *Magnetic field compatible hybrid circuit quantum electrodynamics*. Ph.D. thesis, Delft University of Technology (2019).

[7] Krogstrup, P. *et al.* Epitaxy of semiconductor-superconductor nanowires. *Nature Materials* **14**, 400–406 (2015).

[8] Gazibegovic, S. *et al.* Epitaxy of advanced nanowire quantum devices. *Nature* **548**, 434–438 (2017).

[9] Nitta, J., Lin, Y., Akazaki, T. & Koga, T. Gate-controlled electron g factor in an InAs-inserted-channel In0.53Ga0.47As/In0.52Al0.48As heterostructure. *Applied Physics Letters* **83**, 4565–4567 (2003).

[10] Qu, F. *et al.* Quantized Conductance and Large g-Factor Anisotropy in InSb Quantum Point Contacts. *Nano Letters* **16**, 7509–7513 (2016).

[11] Vaitiekėnas, S., Deng, M.-T., Nygård, J., Krogstrup, P. & Marcus, C. M. Effective g Factor of Subgap States in Hybrid Nanowires. *Phys. Rev. Lett.* **121**, 037703 (2018).

[12] de Moor, M. W. A. *et al.* Electric field tunable superconductor-semiconductor coupling in Majorana nanowires. *New Journal of Physics* **20**, 103049 (2018).

[13] Boscherini, F. *et al.* Exchange reaction, clustering, and surface segregation at the Al/InSb(110) interface. *Phys. Rev. B* **35**, 9580–9585 (1987).

[14] Sporken, R., Xhonneux, P., Caudano, R. & Delrue, J. The formation of the Al-InSb(110) interface. *Surface Science* **193**, 47 – 56 (1988).

[15] Flöhr, K. *et al.* Manipulating InAs nanowires with submicrometer precision. *Review of Scientific Instruments* **82**, 113705 (2011).

[16] de Moor, M. *Quantum transport in nanowire networks*. Ph.D. thesis, Delft University of Technology (2019).

[17] van Veen, J. *et al.* Magnetic-field-dependent quasiparticle dynamics of nanowire single-Cooper-pair transistors. *Phys. Rev. B* **98**, 174502 (2018).

[18] Ullom, J. N., Fisher, P. A. & Nahum, M. Measurements of quasiparticle thermalization in a normal metal. *Phys. Rev. B* **61**, 14839–14843 (2000).

[19] Rajauria, S. *et al.* Efficiency of quasiparticle evacuation in superconducting devices. *Phys. Rev. B* **85**, 020505 (2012).

4

Magnetic field compatible circuit quantum electrodynamics with graphene Josephson junctions

J. G. Kroll, **W. Uilhoorn**, K.L. van der Enden, D. de Jong, K. Watanabe, T. Taniguchi, S. Goswami, M. C. Cassidy, L. P. Kouwenhoven

Circuit quantum electrodynamics has proven to be a powerful tool to probe mesoscopic effects in hybrid systems and is used in several quantum computing (QC) proposals that require a transmon qubit able to operate in strong magnetic fields. To address this we integrate monolayer graphene Josephson junctions into microwave frequency superconducting circuits to create graphene based transmons. Using dispersive microwave spectroscopy we resolve graphene's characteristic band dispersion and observe coherent electronic interference effects confirming the ballistic nature of our graphene Josephson junctions. We show that the monoatomic thickness of graphene renders the device insensitive to an applied magnetic field, allowing us to perform energy level spectroscopy of the circuit in a parallel magnetic field of 1 T*, an order of magnitude higher than previous studies. These results establish graphene based superconducting circuits as a promising platform for QC and the study of mesoscopic quantum effects that appear in strong magnetic fields.*

This chapter has been published in *Nature Communications* **9**, 4615 (2018).

A superconducting transmon qubit [1] resilient to strong magnetic fields is an important component for proposed topological [2–4] and hybrid quantum computing (QC) schemes [5, 6]. A transmon qubit consists of a Josephson junction (JJ) shunted by a large capacitance, coupled to a high quality factor superconducting resonator. In conventional transmon devices, the resonator is fabricated from Al and the JJ is fabricated from an Al/AlO$_\mathbf{x}$/Al tunnel junction [1], both of which cease operation above the critical magnetic field of bulk Al, ∼10 mT. Even when considering alternative type II superconductors such as NbTiN or MoRe that can sustain superconductivity beyond $B = 8\,\mathrm{T}$ [7], when subjected to a strong magnetic field the superconductor will experience detrimental effects such as reduction of the superconducting gap, increased quasiparticle generation [8] and the formation of Abrikosov vortices that cause resistive losses in a microwave field. In addition to disrupting the superconductivity, magnetic flux penetrating the JJ produces electron interference effects that reduce the Josephson energy E_J and strongly suppress the transmon energy spectrum. If the transmon is to be used for fast quantum gates, fast charge-parity detection and long range quantum state transfer in QC schemes [3, 9, 10] we are compelled to consider alternatives to conventional Al based JJs. Proximitised semiconducting nanowires, acting as gate-tuneable superconductor-normal-superconductor JJs [11] have been used successfully in a variety of microwave frequency superconducting circuits, allowing for studies of Andreev bound states [12, 13], electrically tuneable transmon qubits [14, 15] and transmons that exhibit substantial field compatibility [16]. Graphene JJs are an attractive alternative as they exhibit ballistic transport, high critical currents [7, 17, 18] and the atomic thickness of the graphene junction greatly reduces flux penetration, protecting the JJ from orbital interference effects that would suppress E_J in high parallel fields. When combined with geometric techniques that protect the superconducting film, such as critical field enhancement [19] and lithographically defined vortex pinning sites [20, 21], the transmon circuit can be protected at magnetic fields relevant to these proposals, which approach and in some cases exceed 1 T [22–24].

In this work we report the integration of ballistic graphene JJs into microwave frequency superconducting circuits to create graphene based transmons. Using dispersive microwave spectroscopy we resolve the characteristic band dispersion of graphene, and observe coherent electronic interference effects that confirm the ballistic nature of our graphene JJs. We perform energy level spectroscopy at $B_{\parallel} = 0\,\mathrm{T}$ to resolve a linewidth of $\simeq$ 400 MHz. Although the large linewidths prevent coherent qubit control, we demonstrate the device is insensitive to the applied magnetic field up to $B_{\parallel} = 1\,\mathrm{T}$.

4.1. Methods

4.1.1. Fabrication

Two separate devices, device A and device B were used throughout the manuscript. For device fabrication, the type II superconductors NbTiN and MoRe were chosen for their high upper critical fields ($B_{c_2} > 8\,\mathrm{T}$) and their compatibility with microwave frequency devices [25, 26]. Resistive losses from Abrikosov vortices at microwave frequencies are mitigated by expelling the vortices via geometric constriction [19, 27] and using artificial pinning sites to trap the vortices that cannot be excluded [20, 21]. To fabricate

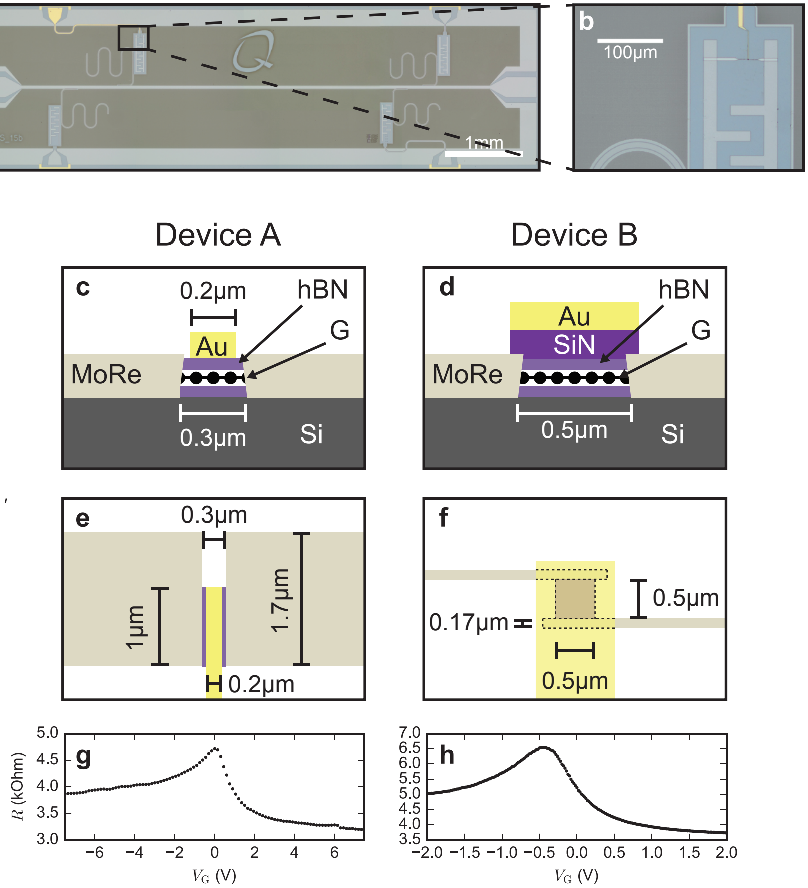

Figure 4.1: **Device structure** **a** Optical image showing multiple CPW resonators frequency multiplexed to a common feedline (device B). **b** Zoomed optical image of the capacitor plates that shunt the Josephson junction, with the gate, junction and contacts visible. **c** Cross sectional diagram showing the geometry of the junction in device A. It is 300 nm in length, with a gate designed to be 200 nm in width. **d** Cross sectional diagram of device B, with the SiN_x/Ti/Au gate giving full coverage of the 500 nm long junction. **e** The junction in device A is 1000 nm wide and contacted by 1700 nm wide MoRe contacts. The 200 nm wide gate can be seen to cover most, but not all of the graphene stack. **f** Device B has a 500 x 500 nm^2 junction that is contacted by thin 170 nm MoRe leads to prevent vortices from forming near the junction. The SiN_x/Ti/Au gate stack is sputtered and designed to give full coverage of the graphene junction. **g** Measurement of the two point resistance R of the contacts and junction for device A at room temperature as the gate voltage V_G is varied. The charge neutrality point can be observed at $V_G = 0$ V. **h** R measurements for device B at room temperature again showing the charge neutrality point, this time offset slightly to $V_G \simeq -0.5$ V. Upon cooling to $T = 15$ mK, the charge neutrality points were observed to shift in both devices.

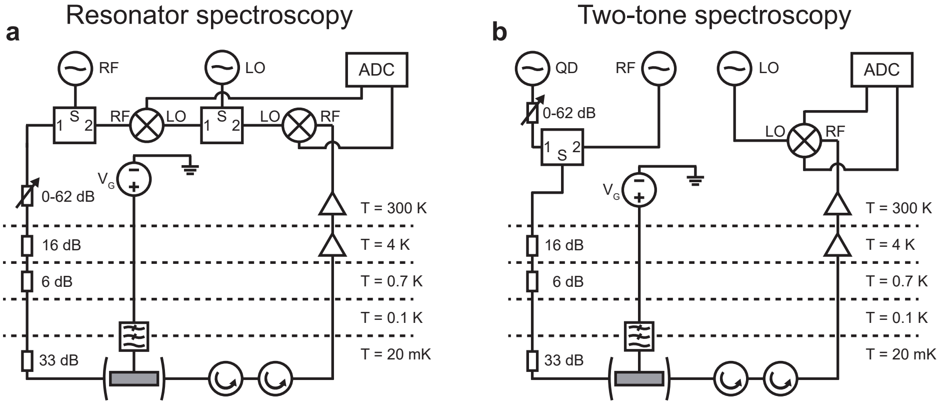

Figure 4.2: **Circuit schematic of the measurement set up. a** Circuit used to perform microwave measurements for resonator spectroscopy and **b** two tone spectroscopy.

the devices 20 nm of NbTiN is sputtered onto intrinsic Si wafers in an Ar/N atmosphere. The resonators, feedline and transmon are reactive ion etched in an SF_6/O_2 atmosphere (Fig. 4.1a,b). In this etching step, an array of artificial pinning sites is also defined. Monolayer graphene is encapsulated between two hBN flakes ($t \simeq 15$ nm each), then deposited between pre-fabricated capacitors using a PMMA based van der Waals pickup method [7]. Contact to the graphene stack is made by etching in a CHF_3/O_2 environment, followed by sputtering MoRe ($t = 80$ nm). Device A was contacted to give a junction length of 300 nm (Fig 4.1c,e). A Ti/Au top gate is then sputtered on top of the stack. The device is then shaped in a CHF_3/O_2 plasma to be 1000 x 300 nm^2 in size. Device B was contacted to provide a junction length of 500 nm (Fig 4.1d,f). The long thin leads were geometrically restricted in two dimensions, making it less favourable for vortices to form, protecting the superconductivity of the contacts proximitising the junction. The junction is then shaped in a CHF_3/O_2 plasma to be 500 x 500 nm^2. A SiN_x/Ti/Au top gate stack is then sputtered to give full junction coverage, giving greater control of μ in the junction. A probe station was used to perform two probe resistance R measurements of the graphene junction and contact resistances at room temperature. Device A (Fig 4.1g) and device B (Fig 4.1h) both show charge neutrality points in the R vs V_G dependences, consistent with graphene junctions.

4.1.2. Characterisation

All measurements were performed in a dilution refrigerator with a base temperature of 15 mK. The samples were enclosed in a light tight copper box, and thermally anchored to the mixing chamber. The two measurement configurations used are depicted in Fig 4.2. Two coaxial lines and one DC line were used to control the sample. The sample was connected to the DC voltage source by a line that was thermally anchored at each stage and heavily filtered at the mixing chamber by low RC, π and copper powder filters. The line used to drive the feedline input was heavily attenuated to reduce noise and thermal excitation of the cavity, allowing the single photon cavity occupancy to be reached.

The output line of the feedline was connected to an isolator (Quinstar QCI-080090XM00) and circulator (Quinstar QCY-060400CM00) in series to shield the sample from thermal radiation from the HEMT amplifier (Low Noise Factory LNF-LNC4-8_C) on the 4K stage. Resonator spectroscopy of device A was performed using circuit **a** to measure the amplitude and phase response of the complex transmission S_{21} as the frequency was varied. Resonator and two-tone spectroscopy of device B was performed using circuit **b**, with a splitter used to combine the readout and excitation tones. This allows the complex S_{21} to be measured, but only at fixed resonator readout frequency otherwise only $|S_{21}|$ can be recorded.

4.2. Results

4.2.1. Dispersive Fabry-Perot oscillations

We begin by performing spectroscopy of the resonator in device A as a function of the input power P_{in} (Fig. 4.3a). Varying the resonator's photon occupation from $\langle n_{\mathrm{ph}}\rangle \simeq 1000$ to $\langle n_{\mathrm{ph}}\rangle = 1$ we observe a dispersive shift $\chi = f_{\mathrm{r}} - f_{\mathrm{bare}}$ in the resonator frequency f_{r} from the high power value f_{bare}. This occurs due to a Jaynes-Cummings type interaction between the harmonic readout resonator and the anharmonic transmon spectrum, with the anharmonicity provided by the Josephson junction [28]. The magnitude of the shift $\chi = g^2/\Delta$ depends on the transmon-resonator coupling g, and the difference $\Delta = f_{\mathrm{r}} - f_{\mathrm{t}}$ between f_{r} and the ground state to first excited state transition frequency $f_{\mathrm{t}} = E_{\mathrm{t}}/h \simeq \sqrt{8E_{\mathrm{J}}E_{\mathrm{C}}}/h$, allowing us to infer E_{J} from χ [1]. Studying χ as a function of gate voltage V_{G} reveals the characteristic band dispersion of graphene (Fig. 4.3b) and allows the voltage at the charge neutrality point (CNP) V_{CNP} to be identified. At negative $V_{\mathrm{G}} - V_{\mathrm{CNP}}$, the chemical potential μ is below the CNP and the graphene is in the p-regime where holes are the dominant charge carrier. Deep into the p-regime, the high carrier density (n_{C}) gives a large E_{J}, placing f_{t} above the resonator and giving χ a small negative value (Fig. 4.3b). As V_{G} approaches the CNP, the Dirac dispersion minimises the density of states reducing E_{J} and f_{t} to a minimum. Since $\chi = g^2/\Delta$, as Δ approaches zero, χ diverges. Once on resonance, the resonator acquires some characteristic of the qubit, significantly broadening the lineshape. Simultaneously, the critical photon number $n_{\mathrm{Crit}} = \Delta^2/4g^2$ collapses [29], moving the measurement into the 'transitionary' regime between high and low photon number as in Fig. 4.3a, causing the anomalous lineshapes visible in Fig. 4.3c near CNP. As V_{G} is increased past the CNP, n_{Crit} and the lineshapes recover, with electrons becoming the dominant charge carrier and E_{J} increasing to a maximum as expected from removal of the n-p-n junction formed by the contacts [7]. The p-regime also experiences periodic fluctuations in E_{J} as a function of V_{G} due to coherent electron interference effects in a Fabry-Perot cavity formed by n-p interfaces at the MoRe contacts [7]. Extracting a line trace (white line Fig. 4.3b) to study the modulation in $|S_{21}|$ with n_{C} (Fig. 4.3c), and performing a Fourier transform (Fig. 4.3d) gives a cavity length of 220 nm in agreement with the device dimensions. The observation of a Dirac dispersion relation in combination with coherent electron interference effects confirm the successful integration of ballistic graphene JJs into a superconducting circuit.

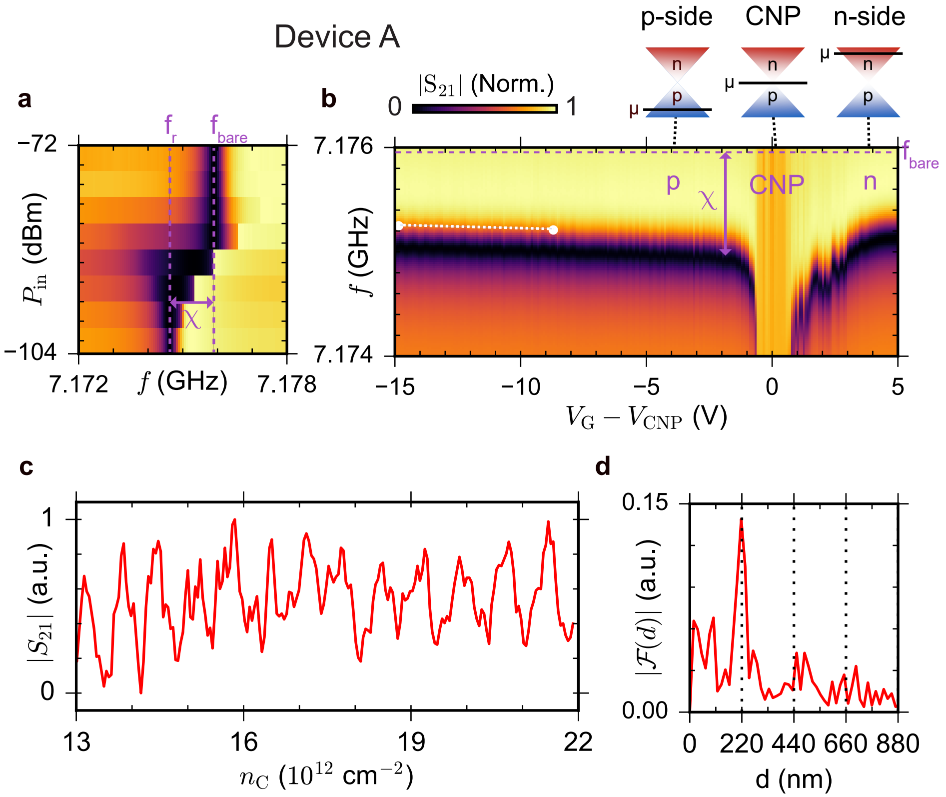

Figure 4.3: **Resonator spectroscopy** as a function of P_{in} and V_{G}. **a** $|S_{21}|$ (Norm.) as a function of input frequency f and input power P_{in}. At single photon occupancy the resonator experiences a frequency shift χ due to repulsion from an energy level above the resonator (device A). **b** At single photon occupancy, $|S_{21}|$ (Norm.) is measured as f and V_{G} are varied, with the voltage at CNP ($V_{\mathrm{CNP}} = 7.8\,\mathrm{V}$) subtracted. Changing V_{G} to tune μ allows the dominant charge carriers to be varied between hole, charge neutral and electron-like regimes. In the p-regime, χ oscillates as V_{G} is varied. We extract the charge carrier density n_{c} **c** from the white linecut to generate a Fourier transform **d** that is consistent with Fabry-Perot oscillations in a cavity of $d = 220\,\mathrm{nm}$.

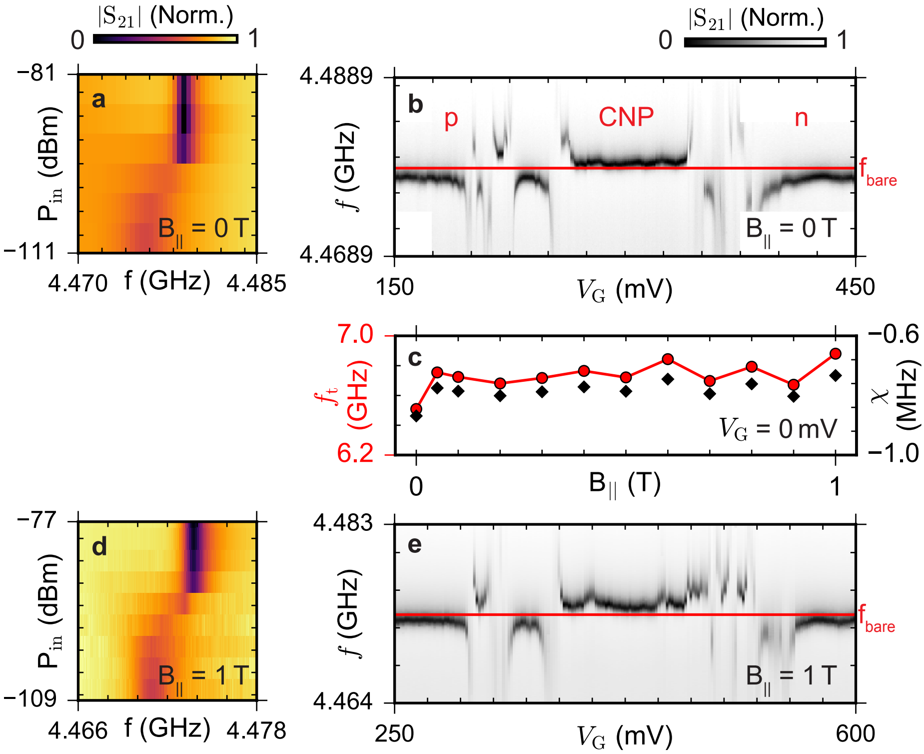

Figure 4.4: **Dispersive shift** as a function of V_G and $B_{\|}$. **a** At $B_{\|} = 0$ T, $|S_{21}|$ (Norm.) versus f again shows a χ indicating the resonator is coupled to the transmon. **b** At $B_{\|} = 0$ T, $|S_{21}|$ (Norm.) versus f and V_G shows the symmetric band dispersion of graphene with additional fluctuations we attribute to UCF. **c** f_t (red circles) extracted from χ (black diamonds) versus $B_{\|}$ at $V_G = 0$ V, showing f_t is not significantly affected. **d-e** Repeating **a** and **b** at $B_{\|} = 1$ T confirms the graphene JJ behaves equivalently to $B_{\|} = 0$ T. The variation observable in b and shift in V_{CNP} between a and c we attribute to slow gate drift.

4.2.2. Insensitivity to applied parallel magnetic field

In device B we repeat measurements of S_{21} as a function of f and P_{in} to again reveal a power shift of the resonator coupling to the transmon (Fig. 4.4a). As we move from the p to the CNP regime, χ is seen to diverge repeatedly as f_t anti-crosses multiple times with f_r (Fig. 4.4b), most likely due to additional coherent electronic interference effects in the form of universal conductance fluctuations (UCF) [14, 30]. This behaviour is repeated moving from the CNP to the n-regime, where E_J is again maximised. We demonstrate the field compatibility of the junction by applying a magnetic field $B_{\|}$ along the length of the junction contacts, parallel to the plane of the film, using the resonator as a sensor for field alignment. Monitoring χ as $B_{\|}$ is varied between 0 and 1 T (Fig. 4.4c) and calculating f_t (using $g = 43$ MHz, extracted from measurements in Fig. 4.5), demonstrates that χ and thus E_J are not significantly affected by the applied $B_{\|}$. The small amount of variation observed is attributed to charge noise induced gate drift which was observed throughout the duration of the experiment. The presence of χ at $B_{\|} = 1$ T (Fig. 4.4d) and

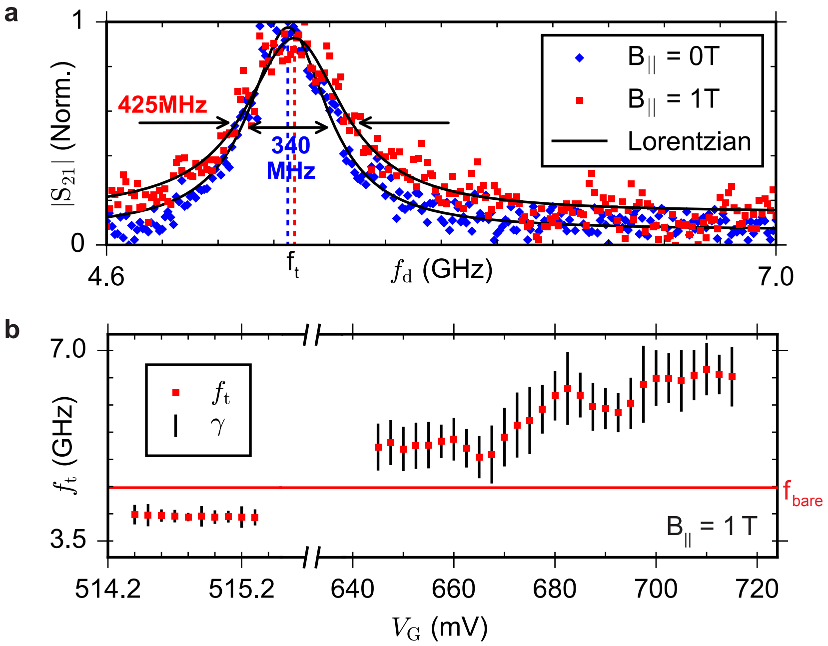

Figure 4.5: **Two tone spectroscopy.** **a** Normalised $|S_{21}|$ at f_r as f_d is varied can be fitted to extract f_t and γ at $V_G = 0\,\text{V}$. At $B_\parallel = 1\,\text{T}$, γ shows a 25% increase compared to $B_\parallel = 0\,\text{T}$. **b** At $B_\parallel = 1\,\text{T}$, f_t and γ are extracted as V_G is varied, demonstrating f_t can be swept over a wide frequency range. Lines bisecting each f_t are not error bars, but represent the extracted γ at each f_t.

it's dependence as a function of V_G (Fig. 4.4e) again reveals the characteristic Dirac dispersion as seen in Fig. 4.4b, with modified UCF and shifted V_{CNP} due to slow gate drift. The insensitivity of f_t to applied field and similarity of device operation at $B_\parallel = 0\,\text{T}$ and 1 T confirm the field resilience of both the graphene JJ and superconducting circuit.

4.2.3. Two tone spectroscopy in high parallel magnetic fields

In order to better understand the microwave excitation spectra of our system we proceed to measure it directly via two-tone spectroscopy [1]. The readout tone is set to f_r whilst a second tone f_d is used to drive the circuit. Excitation of the system results in a state dependent shift of the resonator frequency, and is detected by measuring the change in the complex transmission S_{21} at f_r. At $V_G = 0\,\text{V}$ (p-regime), two-tone spectroscopy at $B_\parallel = 0\,\text{T}$ and 1 T (Fig. 4.5a) can be fitted with a Lorentzian to extract the transmon transition $f_t \simeq 5.2\,\text{GHz}$ and transition linewidth $\gamma \simeq 400\,\text{MHz}$. At $B_\parallel = 1\,\text{T}$, f_t and thus E_J differ only slightly with γ increasing slightly from 350 MHz to 425 MHz. The transmon resonator coupling $g = \sqrt{\chi\Delta} = 43\,\text{MHz}$ is extracted from the observed dispersive shift χ and detuning Δ, and used in the calculation of f_t in Fig. 4.4. We attribute the change in f_t from Fig. 4.4b and the large γ to the dielectric induced charge noise mentioned previously. An estimate of $E_J = 40.2\,\mu\text{eV} = 9.72\,\text{GHz}$ can be provided using the relation $E_t = hf_t \simeq$

$\sqrt{8E_J E_C}$. Performing two-tone spectroscopy in the n-regime while tuning V_G reveals a gate-tunable energy level that is visible above and below the resonator (Fig. 4.5b, V_{CNP} not specified due to gate drift during measurement) that can be fitted to extract f_t and γ, giving a minimum linewidth of 166 MHz (see Fig. 4.6 for the raw data).

4.3. Discussion

The observation of a transition and the inferred high value of E_J in the n and p-regimes (Fig. 4.5a) provides additional confirmation of the electron-hole symmetry expected in graphene. Additional measurement of the higher order two-photon f_{02} transition would allow for exact measurements of E_J and E_C via diagonalisation of the Hamiltonian, enabling investigations into mesoscopic effects of interest in graphene JJs [31, 32]. Importantly, the transition and thus E_J can be varied over a wide frequency range, satisfying a key requirement for implementation into topological QC proposals [3]. If graphene based transmons are to be successfully implemented into these proposals however, the large linewidths that currently prevent measurements of relaxation and coherence lifetimes (T_1, T_2^*) must be reduced. We believe that material improvements to the dielectric materials can achieve this.

In conclusion, we have integrated a graphene JJ into a superconducting circuit to make a graphene based transmon. Additionally, we have achieved operation at $B_{\parallel} =$ 1 T, a magnetic field more than an order of magnitude higher than previous studies [16, 33]. While the broad linewidths prevented the demonstration of coherent qubit control, these results establish graphene based microwave circuits as a promising tool for topological and hybrid QC schemes, and for probing mesoscopic phenomena of interest at high magnetic fields.

Data availability

The data used to support this study, and the code used to generate the figures are available from a public data repository here https://doi.org/10.4121/uuid:b7340d11-e47e-44eb-a60d-679d758c7160.

Acknowledgments

We thank D.J. van Woerkom for fabrication assistance, M.W.A. de Moor and A. Proutski for helpful discussion and L. DiCarlo, C. Dickel and F. Lüthi for experimental advice and software support. This work has been supported by the European Research Council (ERC), The Dutch Organisation for Scientific Research (NWO), and Microsoft Corporation Station Q.

Author contributions

K.W. and T.T. grew the hBN crystals, J.G.K. and W.U. fabricated the devices and performed dc-transport calibartion measurements, J.G.K., K.L.v.d.E. and D.d.J performed the measurements and J.G.K. and K.L.v.d.E. analysed the measurements. The manuscript was prepared by J.G.K. with K.L.v.d.E., S.G., M.C. and L. P. K. providing input. S.G., M.C. and L.P.K. supervised the project.

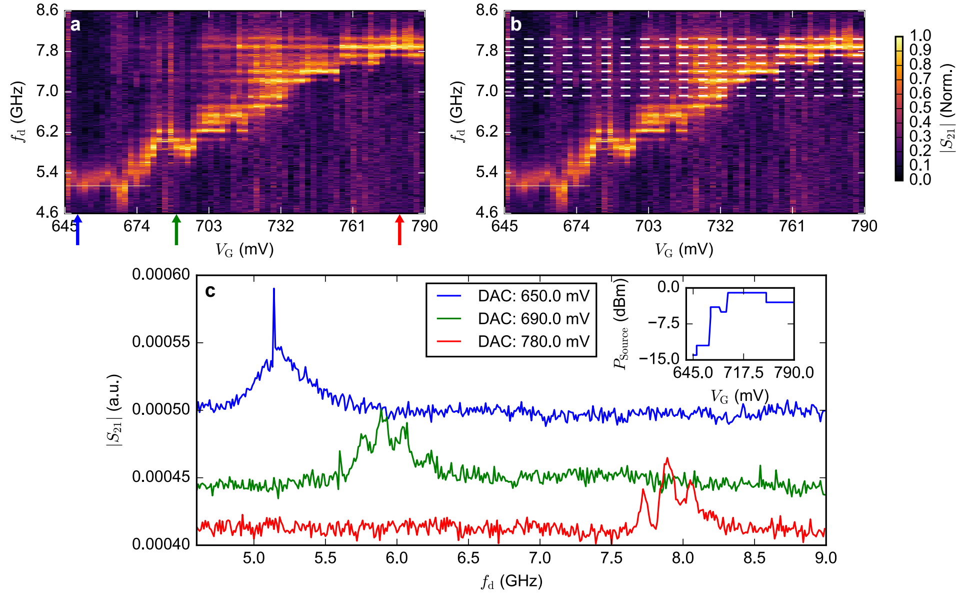

Figure 4.6: **Readout circuit resonance.** **a** Normalised heat map of S_{21} during two-tone spectroscopy as the gate voltage V_G and drive tone f_d is varied. **b** The response of f_t is modulated by background resonances due to a standing wave in the readout circuit, as evidenced by the white lines. **c** Line traces showing $|S_{21}|$ at several V_G values (corresponding to linecuts at coloured arrows in **a**. The sharp resonance at 5.143 GHz is due to interference effects from an additional $\lambda/4$ resonator multiplexed to the common feedline. The inset demonstrates that above ~ 670 mV the higher power required to drive the transition excites additional modes in the circuit, giving the modulation in response as seen in **a**. Above 720 mV the resonances become so extreme that it is difficult to analyse the data reliably, so they are excluded from the main text.

4.4. Supplementary material

4.4.1. Readout circuit resonance

Normalised heatmap of $|S_{21}|$ during two-tone spectroscopy of the transmon energy level f_t as the gate voltage V_G is varied (Figure 4.6a). A sharp peak (dip) at 5.143 GHz (5.640 GHz) is visible due to resonant driving of additional $\lambda/4$ resonators multiplexed to the same feedline. The drive is provided to the transmon indirectly, through the coupled resonator. As the detuning $\Delta = f_\mathrm{t} - f_\mathrm{r}$ is increased, the amount of drive power required to excite the transition at f_t also increases due to the filtering effect of the resonator (Figure 4.6c inset) and low relaxation time T_1. Above 5.7 GHz the drive power becomes so high that an additional resonant mode in the circuit is excited, modulating the two-tone response of S_{21}. We attribute these oscillations to a standing wave ($\Delta f = 160$ MHz, $\lambda = 1.25$ m) in the coaxial cables caused by an impedance mismatch at the device (Figure 4.6b). The resonance was only observable whilst near f_t and at very high power, making a simple background subtraction difficult. Above ~720 mV the very high power required to drive the transition causes many resonances, complicating the analysis. Due to this, data above this point was excluded from the analysis in the main text.

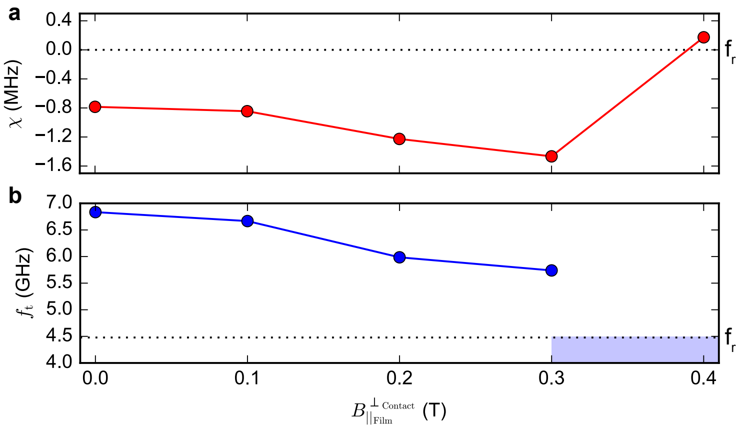

Figure 4.7: **Lead alignment.** **a** Dependence of dispersive shift χ with respect to field $B^{\perp\text{Contact}}_{\parallel\text{Film}}$ applied perpendicular to the length of the junction contacts, but parallel to the film. **b** Extracting f_t from χ shows that as $B^{\perp\text{Contact}}_{\parallel\text{Film}}$ is applied the E_J reduces significantly. As f_t approaches f_r, χ increases until f_t passes through f_r resulting in the sign change of χ. Above $B^{\perp\text{Contact}}_{\parallel\text{Film}} = 0.4\,\text{T}$ the dispersive regime is no longer valid, meaning f_t cannot be accurately estimated. These results imply that the E_J of the junction is only protected if B is applied along the length of the junction contacts.

4.4.2. Lead orientation

During measurement it was found that the orientation of the field with respect to the leads was of key importance. Initially the field was applied along the main axis of the 6-1-1 T vector magnet; parallel to the film and perpendicular to the junction contacts ($B^{\perp\text{Contact}}_{\parallel\text{Film}}$). Despite careful alignment the Josephson energy (E_J) was found to significantly reduce at only ~ 400 mT. In Fig. 4.7b as $B^{\perp\text{Contact}}_{\parallel\text{Film}}$) is increased, E_J reduces, causing the transmon transition to also reduce (as $f_\text{t} \simeq \sqrt{8E_\text{J}E_\text{C}}$). As f_t approaches the resonator the dispersive shift χ increases in magnitude, eventually switching sign as f_t passes through f_r (Fig. 4.7a). In contrast, applying the field parallel to the film and along the long axis of the leads (see Fig. 4.1c) the junction is able to retain a stable E_J up to $B^{\parallel\text{Contacts}}_{\parallel\text{Film}} = 1\,\text{T}$ (Fig. 4.4c).

4.4.3. DC characterisation of graphene JJs

To characterise the performance of graphene JJs in magnetic field and better understand how the junction width W affects E_J, multiple JJs of varying width W between 100 nm and 700 nm were fabricated on doped Si substrates with a thermal oxide dielectric layer. Fig. 4.8a shows a false coloured SEM of a typical graphene junction, with Fig. 4.8b showing a diagram of the cross section. Figure 4.8c shows the numerically calculated differential resistance, $\text{d}V/\text{d}I$, for a typical junction ($W = 500$ nm) as a function of applied DC current as the carrier density in the graphene is tuned using the global back gate. For each trace, the DC current is swept from negative to positive applied current. The dark blue regions show the regions where the junction is superconducting, i.e. $\text{d}V/\text{d}I = 0\,\Omega$. At positive values of applied current, the junction switches from the superconducting to

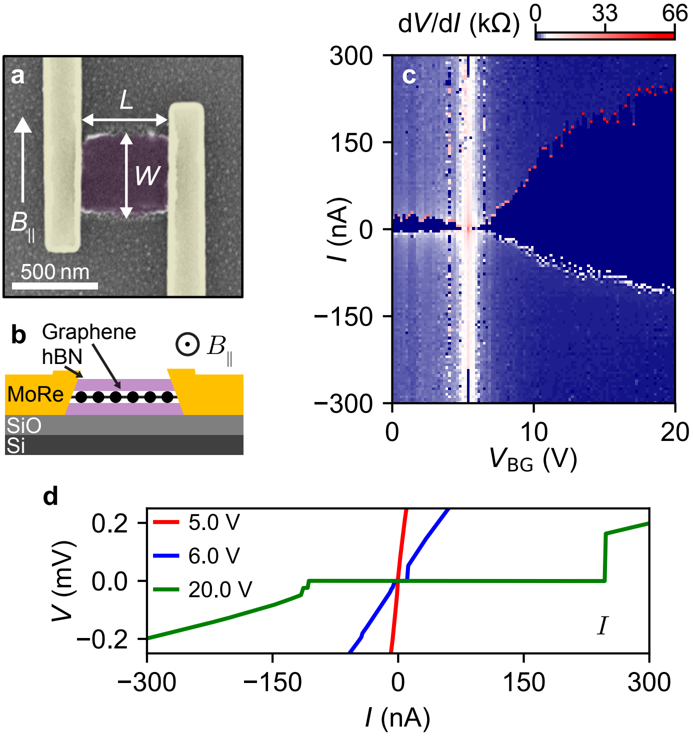

Figure 4.8: **DC characterisation of graphene JJs.** **a** Scanning electron microscope image and **b** schematic cross-section of a ballistic edge-contacted graphene Josephson junction encapsulated in a hexagonal boron nitride (hBN) stack. Device areas are defined for fixed length $L = 500\,\mathrm{nm}$, while the width W is varied from 100 nm - 700 nm. The external magnetic field $B_{\parallel}$ is applied parallel to the junctions plane and leads. The lead area is kept narrow to minimize vortex penetration into the junction. **c** Measured $\mathrm{d}V/\mathrm{d}I$ versus I and V_{BG} in a 500x500 nm junction. **d** V versus I traces at different V_{BG} showing the asymmetric I_{R} and I_{S} and rapid decay of R_{N} from CNP.

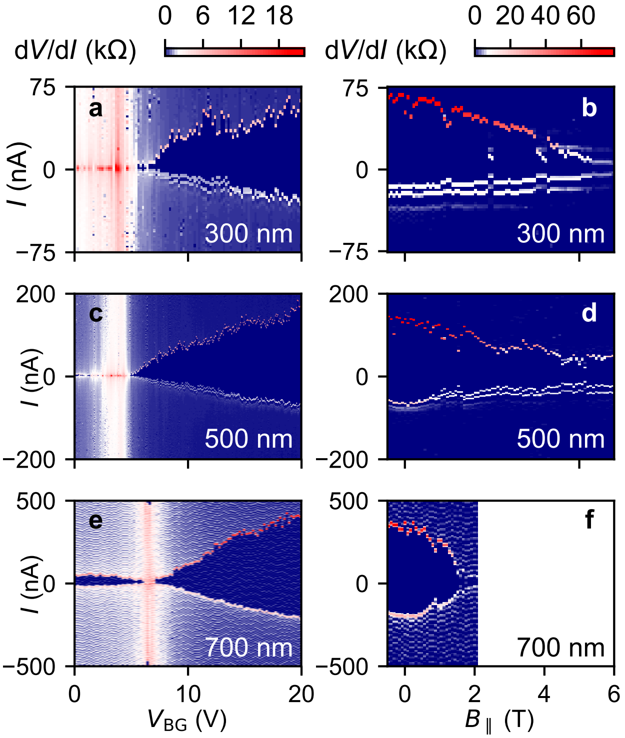

Figure 4.9: **Josephson coupling dependence.** Differential resistance as a function of applied current for increasing back gate voltage for junction widths of **a** 300 nm **b** 500 nm and **c** 700 nm measured at $B_{\parallel} = 0$ T. Both I_S and I_R increase with V_{BG} as the carrier density is increased. **d-f** Differential resistance as a function of applied current for increasing parallel magnetic field $B_{\parallel}$ at $V_{BG} = 20$ V.

the normal state at a switching current I_S, while at negative values of the bias current, the device transitions from the normal to superconducting state at a retrapping current I_R. As I_S tends to occur near but slightly below I_C we can then use this to estimate the E_J of the junction using the relation $E_J = I_C\Phi_0/2\pi \simeq I_S\Phi_0/2\pi$. We note that I_S is always larger than I_R, although the junctions appear to be in the intermediate damping regime. This hysteretic behavior could therefore be explained by heating effects. To emphasise the difference in normal resistance at different backgate voltages line cuts at charge neutrality and maximum backgate voltage are shown in Figure 4.8d.

In total 11 junctions were measured, with the junctions fabricated on 3 different graphene flakes to check for consistency and reproducibility. Fig. 4.9 shows the differential resistance for junctions of widths $W = 300$ nm, 500 nm, and 700 nm taken with respect to gate and parallel magnetic field. Smaller junctions of $W < 300$ nm did not show a notable supercurrent, most probably due to disorder at the edge of the graphene flake. All devices showed the Dirac point occurring between $V_{BG} = 2$ - 5 V, indicating positive (n-type) doping. Magnetic field scans were taken at back gate voltage of $V_{BG} = 20$ V and show that the junctions were able to retain high I_C up to high $B_{\parallel}$. In particular, the 300 nm and 500 nm

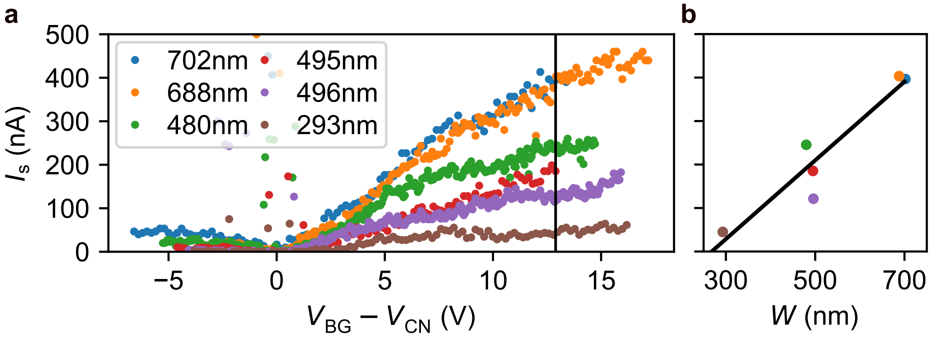

Figure 4.10: **JJ dimension characterization.** **a** Extracted I_S versus $V_{BG} - V_{DP}$ for different W. **b** Width dependence of switching current at relative backgate voltage of $V_{BG} - V_{DP} = 14.3$ V. A linear fit shows a cutoff for W of 260 nm below which no supercurrent can be sustained due to edge scattering.

junctions retain up to $\sim 2/3$ of their E_J up to 2 T with a monotonic reduction, making them very effective as field resilient JJs.

As targeting a specific E_J can be very important depending on the application, a study of I_S versus V_{BG} for different W is presented in Fig. 4.10a. In Fig. 4.10b I_S of each junction is measured at the same V_{BG} after compensating for the Dirac point V_{DP}. Assuming each 2DEG has equal coupling to the backgate, an equivalent voltage should correspond to an equivalent carrier density. Assuming a linear dependence on W, I_S can be seen to reach 0 nA at $W \sim 260$ nm, implying that edge scattering effects in graphene JJs becomes so extreme that supercurrents can no longer be sustained.

References

[1] Koch, J. *et al.* Charge-insensitive qubit design derived from the Cooper pair box. *Physical Review A* **76**, 042319 (2007).

[2] Hassler, F., Akhmerov, A. R. & Beenakker, C. W. J. The top-transmon: a hybrid superconducting qubit for parity-protected quantum computation. *New Journal of Physics* **13**, 095004 (2011).

[3] Hyart, T. *et al.* Flux-controlled quantum computation with Majorana fermions. *Physical Review B* **88**, 035121 (2013).

[4] Aasen, D. *et al.* Milestones toward Majorana-based quantum computing. *Physical Review X* **6** (2016).

[5] Kubo, Y. *et al.* Hybrid quantum circuit with a superconducting qubit coupled to a spin ensemble. *Physical Review Letters* **107**, 220501 (2011).

[6] Ranjan, V. *et al.* Probing dynamics of an electron-spin ensemble via a superconducting resonator. *Physical Review Letters* **110**, 067004 (2013).

[7] Calado, V. E. *et al.* Ballistic Josephson junctions in edge-contacted graphene. *Nature Nanotechnology* **10**, 761–764 (2015).

[8] Van Woerkom, D. J., Geresdi, A. & Kouwenhoven, L. P. One minute parity lifetime of a NbTiN Cooper-pair transistor: Supplementary Information. *Nature Physics* **11**, 547–550 (2015).

[9] Kurizki, G. *et al.* Quantum technologies with hybrid systems. *Proceedings of the National Academy of Sciences* **112**, 3866–3873 (2015).

[10] Ristè, D. *et al.* Millisecond charge-parity fluctuations and induced decoherence in a superconducting transmon qubit. *Nature Communications* **4**, 1913 (2013).

[11] Doh, Y. *et al.* Applied physics: Tunable supercurrent through semiconductor nanowires. *Science* **309**, 272–275 (2005).

[12] Van Woerkom, D. J. *et al.* Microwave spectroscopy of spinful Andreev bound states in ballistic semiconductor Josephson junctions. *Nature Physics* **13**, 876–881 (2017).

[13] Hays, M. *et al.* Direct Microwave Measurement of Andreev-Bound-State Dynamics in a Semiconductor-Nanowire Josephson Junction. *Physical Review Letters* **121**, 047001 (2018).

[14] De Lange, G. *et al.* Realization of microwave quantum circuits using hybrid superconducting-semiconducting nanowire Josephson elements. *Physical Review Letters* **115**, 127002 (2015).

[15] Larsen, T. W. *et al.* Semiconductor-nanowire-based superconducting qubit. *Physical Review Letters* **115**, 127001 (2015).

[16] Luthi, F. *et al.* Evolution of nanowire transmon qubits and their coherence in a magnetic field. *Physical Review Letters* **120** (2018).

[17] Allen, M. T. *et al.* Observation of electron coherence and Fabry-Perot standing waves at a graphene edge. *Nano Letters* **17**, 7380–7386 (2017).

[18] Chtchelkatchev, N. M. & Burmistrov, I. S. Conductance oscillations with magnetic field of a two-dimensional electron gas superconductor junction. *Physical Review B* **75**, 214510 (2007).

[19] Stan, G., Field, S. B. & Martinis, J. M. Critical field for complete vortex expulsion from narrow superconducting strips. *Phys. Rev. Lett.* **92**, 97003–97004 (2004).

[20] Bothner, D., Gaber, T., Kemmler, M., Koelle, D. & Kleiner, R. Improving the performance of superconducting microwave resonators in magnetic fields. *Applied Physics Letters* **98**, 102504 (2011).

[21] Kroll, J. *et al.* Magnetic-Field-Resilient Superconducting Coplanar-Waveguide Resonators for Hybrid Circuit Quantum Electrodynamics Experiments. *Phys. Rev. Applied* **11**, 064053 (2019).

[22] Deng, M. T. *et al.* Majorana bound state in a coupled quantum-dot hybrid-nanowire system. *Science* **354**, 1557–1562 (2016).

[23] Suominen, H. J. *et al.* Zero-Energy Modes from Coalescing Andreev States in a Two-Dimensional Semiconductor-Superconductor Hybrid Platform. *Physical Review Letters* **119**, 176805 (2017).

[24] Zhang, H. *et al.* Quantized Majorana conductance. *Nature* **556**, 74–79 (2018).

[25] Megrant, A. *et al.* Planar superconducting resonators with internal quality factors above one million. *Applied Physics Letters* **100**, 113510 (2012).

[26] Singh, V., Schneider, B. H., Bosman, S. J., Merkx, E. P. J. & Steele, G. A. Molybdenum-rhenium alloy based high- Q superconducting microwave resonators. *Applied Physics Letters* **105**, 222601 (2014).

[27] Samkharadze, N. *et al.* High-Kinetic-Inductance Superconducting Nanowire Resonators for Circuit QED in a Magnetic Field. *Physical Review Applied* **5**, 044004 (2016).

[28] Reed, M. D. *et al.* High-fidelity readout in circuit quantum electrodynamics using the jaynes-cummings nonlinearity. *Physical Review Letters* **105** (2010).

[29] Schuster, D. I. *Circuit Quantum Electrodynamics*. Ph.D. thesis, Yale University (2007).

[30] Lee, P. A. & Stone, A. D. Universal conductance fluctuations in metals. *Physical Review Letters* **55**, 1622–1625 (1985).

[31] Nanda, G. *et al.* Current-phase relation of ballistic graphene Josephson junctions. *Nano Letters* **17**, 3396–3401 (2017).

[32] Kringhøj, A. *et al.* Anharmonicity of a superconducting qubit with a few-mode Josephson junction. *Physical Review B* **97**, 060508 (2018).

[33] Ku, J., Yoscovits, Z., Levchenko, A., Eckstein, J. & Bezryadin, A. Decoherence and radiation-free relaxation in Meissner transmon qubit coupled to Abrikosov vortices. *Physical Review B* **94**, 165128 (2016).

5

A semiconductor nanowire Josephson junction laser

W. Uilhoorn, J. G. Kroll, D. de Jong, D. J. van Woerkom, P. Krogstrup, L. P. Kouwenhoven, M. C. Cassidy

We demonstrate a microwave laser made from a proximitized semiconducting nanowire strongly coupled to a multi-mode superconducting coplanar waveguide cavity. A small dc voltage bias applied to the nanowire Josephson junction results in photon emission when the voltage bias is equal to a multiple of the fundamental cavity frequency, via the ac Josephson effect. Analysis of the real time emission statistics shows a maximum coherence time of 60 µs, *at a photon occupancy of* $\sim$*1000 photons. The electrical tunability of the photon emission provided by the proximitized semiconducting nanowire allows for fast control of the laser emission, paving the way for on-chip control and readout of quantum devices.*

5.1. Introduction

Engineered superconducting circuits have made rapid progress in simulating atomic systems at microwave frequencies [1–3] and form a promising platform for a scalable system for quantum information processing [4, 5]. The compact size of these circuits compared to the relatively large size of the artificial atoms allows for strong coupling rates to be achieved, and makes them easy to integrate into complex device architectures. One of the simplest artificial atoms that can be considered is a single Josephson junction (JJ), a weak link connecting two bulk superconducting electrodes. The Josephson coupling energy of this weak link is $E_J = \frac{\hbar I_C}{2e}$, where I_C is the critical current and $2e$ the Cooper pair charge. For a single superconductor-insulator-superconductor (SIS) junction, E_J is fixed by device fabrication, but can be tunable if two SIS JJs are arranged in parallel in a SQUID geometry. Recently, it has been shown that a highly efficient microwave laser, or maser can be made by strongly coupling a JJ to a high-Q superconducting cavity [6, 7]. In this work, a split JJ structure was used, and the Josephson coupling was tuned by an external magnetic flux. Although this allowed for the investigation of the device performance under a broad range of Josephson couplings, it makes the system unsuitable for fast controlled laser pulses and makes the laser sensitive to flux noise. Lasing from other nanoscale systems in the microwave regime has relied on tunneling via superconducting [8, 9] and semiconducting islands [10], where the finite charging energy has led to linewidth broadening and emission blinking due to charge noise.

Superconductor-normal-superconductor (SNS) Josephson junctions formed in proximitized semiconductors are key materials for a range of emerging technologies. Recent advances in materials have allowed the epitaxial growth of a superconductor on semiconductor materials [11, 12] which has resulted in strongly proximitized devices that display a hard induced superconducting gap and significant supercurrents that can be tuned locally by an external electrostatic gate [13]. These devices have been incorporated into microwave circuits to form hybrid transmon qubits [14, 15] where the Josephson coupling, and so qubit frequency is controlled by a local gate and form the basis for many topological quantum computing schemes [16–18].

In this Letter we demonstrate a microwave laser made from a proximitized InAs-Al nanowire strongly coupled to a multi-mode superconducting coplanar waveguide cavity. A small DC voltage bias applied to the nanowire JJ results in photon emission when the voltage bias is equal to a multiple of the fundamental cavity frequency, via the ac Josephson effect. Using an external gate, we can control the Cooper pair tunneling rate through the junction, and hence tune the emission intensity of the laser. Analysis of the real time emission statistics shows coherence times exceeding 60 µs, a four-fold improvement over the SIS JJ laser [6].

5.2. Device design

Figure 7.1a shows an optical image of the device. The laser is made from a proximitized semiconducting InAs-Al nanowire Josephson junction embedded into a half-wave superconducting coplanar waveguide (CPW) resonant cavity (f_{cavity} = 5.4818 GHz). The cavity is made strongly asymmetric, with the rate of photon emission out of the input port ($k_{\text{i}} \approx$ 1.5 MHz) roughly an order of magnitude less than the rate of photon emission

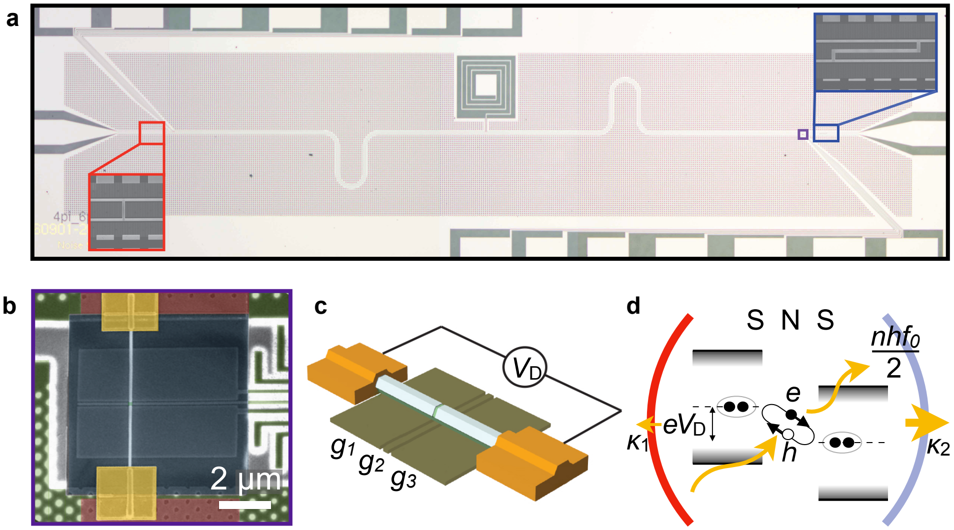

Figure 5.1: **Nanowire Josephson junction laser.** **a** Optical microscope image of the nanowire JJ laser. The device consists of a NbTiN CPW half-wave resonator with fundamental frequency $f_{\text{cavity}} = 5.4818$ GHz, together with an InAs-Al nanowire JJ located at the electric field anti-node of the cavity. A DC bias is applied directly across the nanowire JJ via a spiral inductor located at the electric field node of the resonator. Insets: Asymmetric coupling capacitances ensure that the microwave photons leave predominantly via the output port of the cavity. **b** Scanning electron micrograph image and **c** schematic of the InAs-Al nanowire Josephson junction. Metallic gates g_1 and g_3 control the electrochemical potential in the proximitized nanowire, while the Josephson coupling is tuned by gate g_2. **d** Schematic representation of the working principle. Cooper pair transport between two superconducting condensates (dashed lines) offset by eV_D is provided by ABS channels under exchange of energy with the cavity. Superconducting gap edges are depicted by smoothed solid line, representing subgap states softening the superconducting gap as generally present in proximitized structures.

out the output port ($k_o \approx 15$ MHz), ensuring the microwave photons leave predominantly via the output port. A spiral inductor is placed at the electric field node for applying a voltage bias across the nanowire JJ. Tuning of the electrochemical potential in the nanowire is made possible by a series of electrostatic bottom gates that are isolated from the nanowire by a thin layer of SiN_x (Figure 7.1b,c). Two outer gates, g_1 and g_3, control the chemical potential in the nanowire underneath the superconductor, while a central gate g_2 tunes the Josephson coupling (See Supplementary Information). The device is packaged in a light-tight enclosure that suppresses unwanted free-space cavity modes, and then measured in a dilution refrigerator with a base temperature of ~20 mK. The bandwidth from 3 GHz to 8 GHz of the high-electron-mobility transistor (HEMT) amplifier installed in the dilution refridgerator limits the emission measurements to the fundamental cavity frequency. We apply a voltage bias to the nanowire using an on-board voltage divider circuit that reduces the associated frequency noise of the emitted photons. Measurements of the emission spectrum at the output of the cavity were performed both by using standard heterodyne measurement techniques and with a spectrum analyzer.

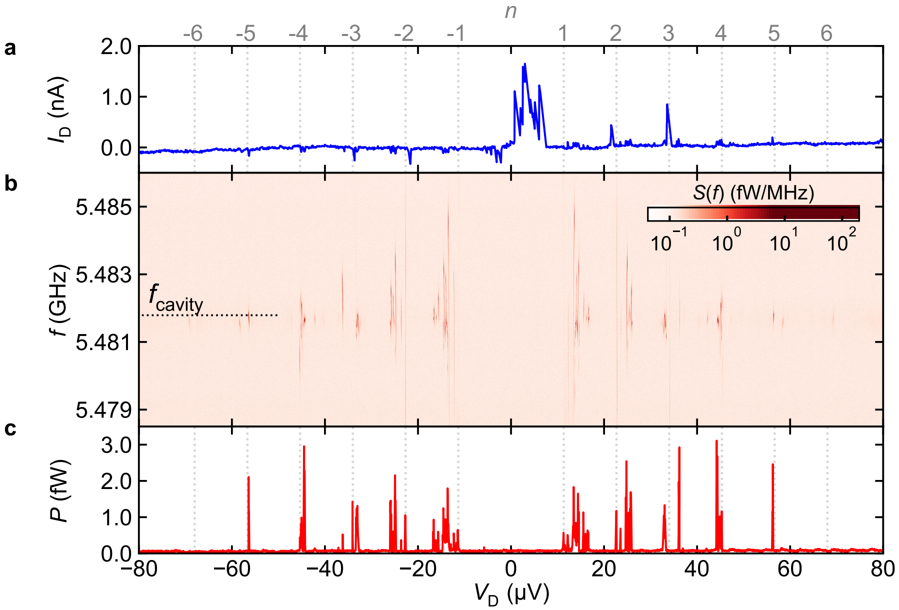

Figure 5.2: **Emission and lasing.** **a** Current I_D flowing through the nanowire JJ as a function of voltage bias V_D when g_2 is close to pinch off. Dashed vertical lines indicate the predicted voltages for stimulated emission. **b** Power spectral density of the freely emitted signal measured at the cavity output. **c** Integrated power spectral density across the frequency span in b.

5.3. Results

5.3.1. Josephson radiation spectrum

The device is tuned into the tunneling regime by pinching off gate g_2, while keeping g_1 and g_3 fixed at a small positive voltage. We measure the current flowing through the device, I_D (Figure 5.2a) and record the power spectral density $S(f)$ of the emitted free-running radiation (Figure 5.2b) around the fundamental resonant frequency of the cavity. As predicted, at voltage biases equal to a multiple of the fundamental cavity frequency, we observe a burst of microwave radiation from the cavity corresponding to an increase in the Cooper pair tunneling rate across the junction. The frequency and voltage span over which the emission of individual harmonics are spread decrease with higher harmonics, indicating a decrease in coupling strength due to the decreasing non-linearity of the JJ (see Supplementary Information). Nontheless, the integrated emission intensifies with increased voltage bias (Figure 5.2c), since the parametric down-conversion results in the creation of multiple photons at the fundamental frequency of the cavity per single Cooper pair tunneling event. The mixing required for this down-conversion process arises from the non-linearity of the Josephson junction, similar to the recently demonstrated SIS JJ laser [6], and shows chaotic behavior as expected for a driven non-linear coupled oscillator system [7]. Unlike the SIS JJ laser, where the emission intensity increases all the way up to the superconducting gap Δ, here the emission intensity is

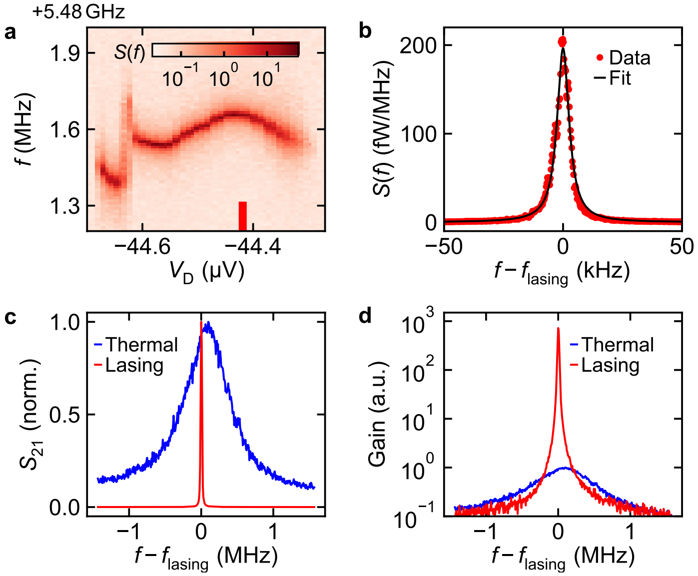

Figure 5.3: **Linewidth and Gain.** **a** Zoom in of $S(f)$ vs V_D around the $n = 4$ emission peak. **b** Line cut at $V_D = -44.42$ μV with Lorentzian fit. **c** Emission linewidth narrowing and **d** gain for the device when lasing and not lasing.

quenched from $n = 5$. The increasing subgap tunneling current at higher bias voltages observed in the dc transport confirms that the quenching of the coherent radiation is a result of the excitation of quasiparticles across the junction (See Supplementary Information).

A zoom-in of the emission at $n = 4$, where the emitted power is the strongest, is shown in Figure 5.3a. Analysis of the emission spectrum at $V_D = -44.42$ μV (Figure 5.3b) shows a time-averaged Lorentzian spectrum with a full width half max $\Delta f = 6.1$ kHz, providing a lower bound for the phase coherence time of $\tau_{\text{coh}} = 1/\pi\Delta f = 52$ μs. To quantify the amplification characteristics we apply an input signal to the cavity using a network analyzer, and measure almost three orders of magnitude linewidth narrowing (Figure 5.3c) and almost three orders of magnitude gain when the device is lasing in injection locked-state compared to when it is biased at an off-resonant point (Figure 5.3d).

5.3.2. Laser coherence

To gain a further insight into the emission properties of the SNS JJ laser, we study the emission statistics in real time. For each of the emission peaks, we sample the in-phase and quadrature components of the output field at a sampling rate of 1 GHz using a heterodyne demodulation setup. IQ histograms for each of the emission peaks show signals coherent in amplitude with a slipping phase over the time of the 0.432 s long measurement (Figure 5.4a). Higher emission amplitudes are observed at higher modes, as a single tunneling event results in multiple photons. We attribute the deviations from a monotonically increasing trend in emission amplitude to the combination of the variation of

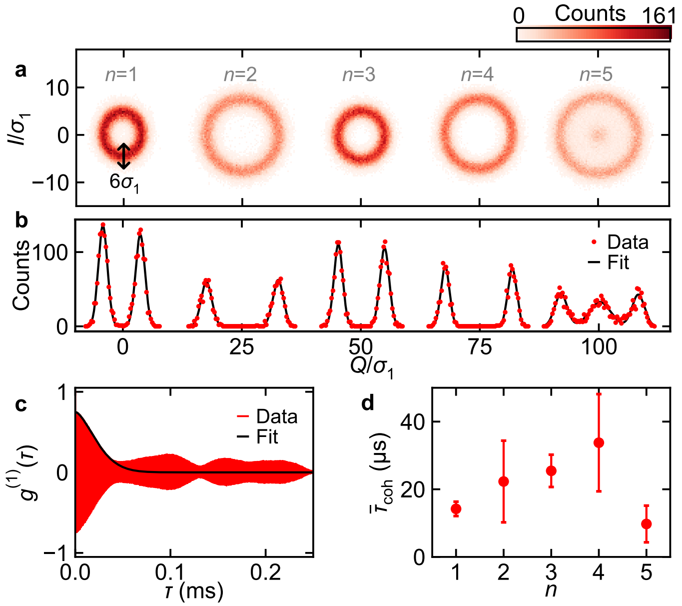

Figure 5.4: **Laser Coherence.** **a** IQ histograms of the nanowire laser output emission at voltage bias points corresponding to emission harmonics $1 \leq n \leq 5$. Each histogram contains 9e4 datapoints and is offset by $Q = 25$⊠ for visibility. **b** Linecuts of the histograms at $I/\sigma_1 = 0$ are well-fitted by Gaussian distributions. **c** The first 0.25 ms of a 1 ms long autocorrelation at $n = 4$ (red), with an exponential decaying fit (black) corresponding to $\tau_{\mathrm{coh}} = 28.89 \pm 0.01$ μs. **d** Average coherence times based on the exponential fits performed on the autocorrelations of the raw time domain data at each emission point.

the coupling within individual emission modes and the hysteretic behaviour of the voltage bias making it difficult to accurately tune the system. All five emission peaks show equal standard deviation of the emission amplitude, implying the noise is dominated by our set-up. While the first four emission peaks show a clear Gaussian donut structure indicating coherent emission, the IQ histogram of the 5th emission peak shows an additional peak centered at (I,Q) = (0,0), corresponding to thermal rather than coherent emission. Analysis of the raw time series data for each of the emission peaks allows us to directly extract the phase coherence time τ_{coh} by performing an autocorrelation on the time domain data. The first 0.25 ms of a typical autocorrelation of the $n = 4$ peak is shown in Figure 5.4b, where the exponential decaying fit corresponds to $\tau_{\mathrm{coh}} = 28.89 \pm 0.01$ μs. For each mode ten 1 ms long autocorrelation measurements were recorded at a rate of 1 GHz and fitted (See Supplementary Information). We see that the average laser coherence time increases with the number of photons associated with a single Cooper pair tunneling event up to $\bar{\tau}_{\mathrm{coh}} = 34 \pm 14$ μs with a maximum recorded $\tau_{\mathrm{coh}} = 67.44 \pm 0.01$ μs at the $n = 4$ peak, and then rapidly drops as the laser emission is quenched by quasiparticle tunneling (Figure 5.4c).

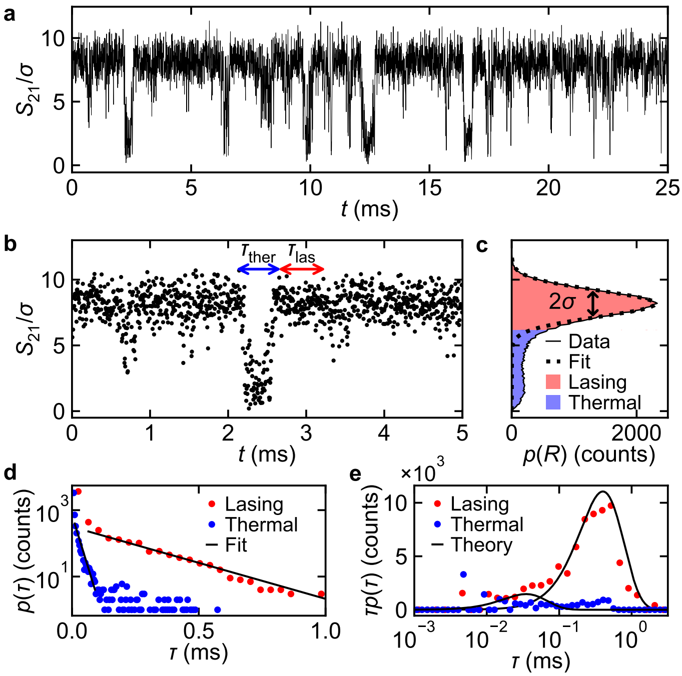

Figure 5.5: **Quasiparticle poisoning.** **a-b** Laser emission amplitude S_{21}/σ as a function of time at the $n = 5$ emission peak. τ_{las} is the time the laser spends on, and τ_{therm} the time the laser spends turned off. Each point represents an integration of the demodulated emission amplitude amplitude for 48 µs. **c** Histogram of the full 432 ms long dataset, fitted by a Gaussian distribution for the lasing state (dashed line). Coloured areas show the thresholding according to $\frac{R-2\sigma}{\sigma}$ with R the avergage radius of the emission in the lasing state. **d** Histograms of times spent in the lasing state and off state allow us to extract characteristic timescales for the quasiparticle poisoning and unpoisoning process, $\overline{\tau}_{\text{lasing}} = 200 \pm 10$ µs and $\overline{\tau}_{\text{thermal}} = 17 \pm 2$ µs respectively. **e** Weighted histogram of the dwell times $\tau p(\tau)$ showing the temporal statistics for both states. Comparison with theoretical predictions (solid black) confirm Poisson statistics solely for the dwell times in the lasing state.

5.3.3. Quasiparticle dynamics

The emission blinking seen at the $n = 5$ emission peak provides a unique opportunity for studying quasiparticle poisoning dynamics in an open SNS JJ system where charging energy has been almost completely quenched. Quasiparticle poisoning in such a system is relevant for topological quantum computing schemes that rely on turning charging energy on and off, where parity is destroyed by the tunneling of a quasiparticle across a SNS JJ. Quasiparticle tunneling across the junction absorbs microwave photons from the cavity, but does not generate photons as the energy is dissipated into the continuum. In the SIS JJ laser, this excitation and resultant damping process only occurred at $V_D \gtrsim \Delta$, a measure of the hardness of the superconducting gap. In a SNS junction, however, the finite density of states within the gap allows for this excitation to occur with quasiparticles of much lower energy than Δ. We are able to directly monitor the quasiparticle poisoning of the device in real time, by studying the dynamics of the laser emission around the $n = 5$ emission peak. Figure 5.5a shows a representative time trace of the amplitude S_{21} of the laser emission when biased at $V_D = 56\,\mu\text{V}$. Data was acquired at 1 GS/s after which it was demodulated with an integration time of 48 µs. A histogram of S_{21}/σ shows two overlapping distributions (Figure 5.5c), a Gaussian distribution for the lasing state centered at $R/\sigma = 8.17$ and a distorted Gaussian distributed thermal state due to the non-linear transformation (See Supplementary Information). By applying a threshold at $S_{21}/\sigma = \frac{R-2\sigma}{\sigma}$, we see the laser emits $\sim$ 82 % of the time. Furthermore dwell times for both states, τ_{las} and τ_{ther}, can be extracted (Figure 5.5b). A histogram of the dwell times reveals the characteristic lifetimes of the lasing and poisoned process, exponential fits result in $\bar{\tau}_{\text{lasing}} = 200 \pm 10\,\mu\text{s}$ and $\bar{\tau}_{\text{thermal}} = 17 \pm 2\,\mu\text{s}$. Similar quasiparticle poisoning times have recently been measured in an Andreev qubit device [19]. It should be noted that blinking events (on-off-on) with time scales faster than the integration time are not captured by this analysis. Additionally, the simple thresholding of the overlapping distributions leads to false-positives as well as false-negatives, skewing the histograms slightly towards lower values. Therefore, to enhance the visibility of deviations from an exponential decaying trend, $\tau p(\tau)$ is plotted. Comparison with the theoretically predicted curve given the total number of counts and the average lifetime shows a Poissonian distribution of the dwell times for the lasing state with a fidelity of $F_{\text{lasing}} = 0.954$ (See Supplementary Information). Confirming the quasiparticle tunneling events are uncorrelated quantum processes. The temporal distribution obtained for the thermal state shows a fidelity of $F_{\text{thermal}} = 0.624$ and is therefore not found to be Poissonian. The lack of number of counts prevents the conclusion that the driven process deviates from Poisson statistics.

5.4. Conclusion and outlook

In conclusion, we have demonstrated coherent emission from a gate tunable SNS JJ strongly coupled to a superconducting microwave cavity. Coherence times as high as 60 µs are seen at the $n = 4$ emission peak, still one order of magnitude removed from the coherence times of state of the art superconducting qubits. However, the local and electrical tuning of the Josephson coupling makes this system very suitable for scalable fast-controlled coherent radiation for on-chip qubit control and readout. Future work will concentrate on integrating this nanowire with hybrid superconducting systems, and study of their pulsed characteristics. Recently, a double quantum dot nanowire laser has been able to read out the charge state of another nanowire double quantum dot at the other end of the superconducting cavity [20], demonstrating the immediate applicability of on-chip microwave sources in the readout and control of circuit QED devices.

Acknowledgements

We thank A. Akhmerov and G. de Lange for helpful discussions. This work has been supported by the Netherlands Organisation for Scientific Research (NWO), Foundation for Fundamental Research on Matter (FOM), NanoFront Program, Danish National Research Foundation, European Research Council (ERC) and Microsoft Corporation Station Q.

5.5. Supplementary Information

5.5.1. Fabrication Details

A thin NbTiN film of thickness $d = 20$ nm is first reactively sputtered on a C plane sapphire substrate (Kyocera). The CPW resonator and gate structure are defined via electron beam lithography using CSAR 6200.09 resist, followed by dry etching in a SF_6/O_2 environment. A global SiN_x dielectric ($d = 30$ nm) is deposited using plasma enhanced chemical vapor deposition (PECVD), and then selectively etched away from the device, excluding the region directly above the gates, using a hydrofluoric acid solution. A single InAs-Al nanowire is then deposited on top of the gates and perpendicular to the cavity using a deterministic micromanipulation deposition technique. The Al shell was then wet etched (Transene D) in the region directly above gate g_2, forming a gate tunable Josephson junction. The source and drain contacts to the nanowire were formed by Ar etching the native oxide from the Al shell, then sputtering NbTi/NbTiN for contacting followed by evaporation of a 30 nm Au cap. The short Ar ion mill before metal deposition removes the surface oxide of the nanowire to ensure low-resistance electrical connection. The thin layer of Au is evaporated over the NbTiN contacts to act as a local quasiparticle trap [21]. The sample is diced to its final size of 2×7 mm to exactly fit its enclosure.

5.5.2. Tunability of Josephson coupling

The midde bottom gate g_2 controls the electrostatic environment at the junction, influencing the Andreev bound state (ABS) channels that carry the Cooper pairs across. Hence, the critical current I_C and thus the Josephson coupling $E_J = \frac{\hbar I_C}{2e}$ are varied by g_2. Figure 5.6a shows the IV-response when sweeping the bias voltage from negative to positive voltages and varying g_2 while keeping g_1 and g_3 at 250 mV. By increasing the tunneling barrier, i.e. more negative g_2 voltages, the system is tuned from a quantum dot-like regime into the tunneling regime, $g_2 <$ -2.8 V. The extracted supercurrent I_S is plotted in the right panel, showing a decreasing trend with fewer ABS channels available for Cooper pair transport. Linecuts at the orange and green tags are shown in Figure 5.6b, indicating that there are more dissipation channels in the dot-like regime than in the tunneling regime. The sweeping direction is also revealed by the inaccesible ”shadowed” areas in the dissipative regime. Moreover, a power spectrum was taken while simulta-

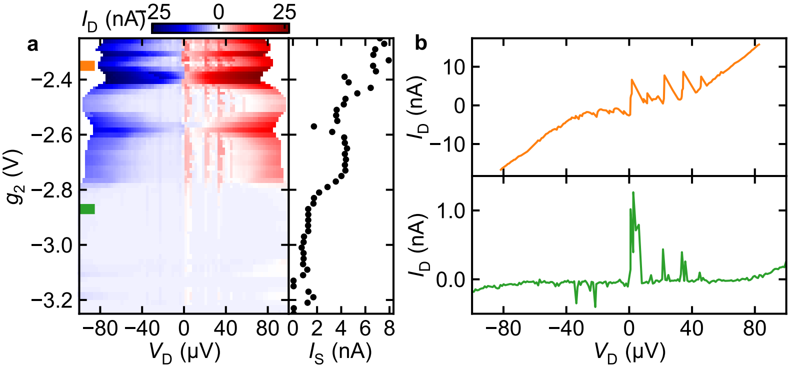

Figure 5.6: **Gate tunable supercurrent. a** Left panel: Current flowing through the nanowire as a function of voltage bias as gate g_2 is tuned close to pinch off. Right panel: Extracted switching current I_S. **b** Linecuts of the quantum dot-like regime (orange) and tunneling regime (green) corresponding to the orange and green tag in a.

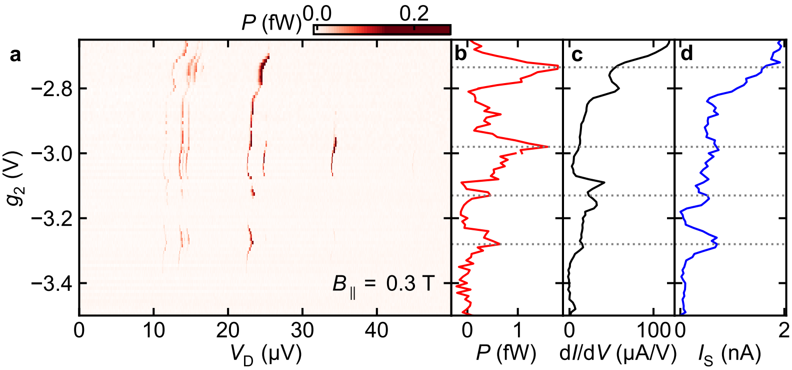

Figure 5.7: **Gate tunable emission. a** Power spectra density as a function of V_D as gate g_2 is varied. **b** Extracted accumulated power. Grey dotted lines are guides for the eye for comparison with the **c** extracted differential subgap conductance and **d** swichting current I_S from simultaneously taken DC measurements.

neously recording I_D (Figure 5.7). Comparing the extracted power of the emission, the differential subgap conductance and the supercurrent indicates emission into the cavity is stimulated when the supercurrent is sufficient whilst having a low enough subgap conductance (Figure 5.7b,c,d). Due to circumstances this measurement was only taken at finite magnetic field aligned along the longitudinal axis of the nanowire.

5.5.3. Overview of emission pulling per harmonic

The emission bursts exhibit a rich behaviour in frequency due to the strong non-linear hybridization of the Josephson radiation with the microwave cavity with $f_{\text{bare}} = 5.4818$ GHz. Figure 5.8 shows zoom ins of the emission responses of the individual fundamental and higher down-converted modes.

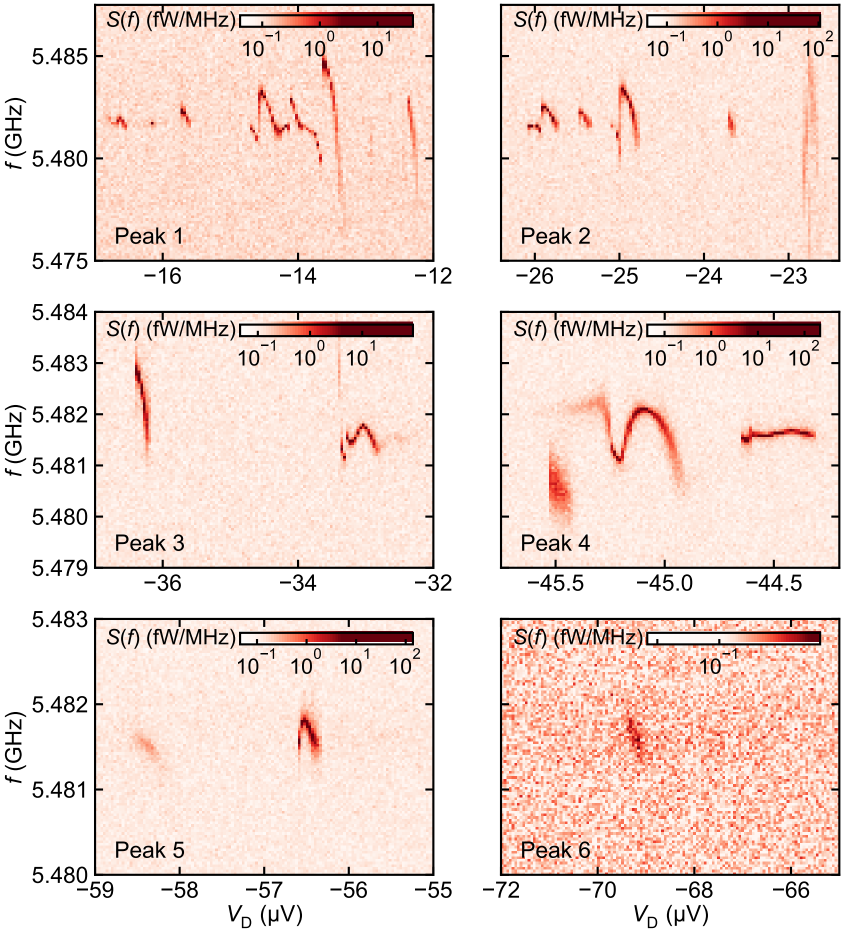

Figure 5.8: **Overview emission peaks.** Zoom in of the emission peaks when the SNS laser is emitting freely into the cavity.

5.5.4. Injection pulling and locking

Having observed coherent microwave radiation through the amplification of stimulated emission at the output of the device allows us to study the injection pulling and locking between two oscillators, in our case the JJ and the microwave resonator. An input tone injected in the microwave resonator pulls the Josephson radiation towards the injected frequency (Figure 5.10) and eventually locks it (Figure 5.9) when the right power is applied with respect to the difference between the two resonance frequencies. Figure 5.10 shows the locking of the two oscillators, as seen by the increase of the loaded quality factor Q_l with increasing injection power P_inj. The linewidth measurement is limited by the network analyzer for $P_\mathrm{inj} > -30\,\mathrm{dB\,m}$, explaining the non-Lorentzian lineshape. Furthermore we demonstrate we can use the device to generate a microwave frequency comb through injection pulling when the injected tone is off-resonant with the Josephson radiation (Figure 5.10a-b), as described by Adler's theory for the synchronization of coupled oscillators [22] and observed in traditional and exotic laser systems [6, 10, 23]. At an input power of $P_\mathrm{inj} > -6.25\,\mathrm{dB\,m}$ we observe a injection locking range Δf of 0.5 MHz (Figure 5.10c). The frequency range over which the device can be injection locked strongly depends on the injected power (Figure 5.10d), given by $\Delta f = \alpha\sqrt{P_\mathrm{inj}}$ [22] with experimentally determined $\alpha = 50\,\mathrm{GHz}/\sqrt{\mathrm{W}}$ and given the attenuation of $-95.7\,\mathrm{dB}$ to the sample.

5.5.5. Quasiparticle excitations in SNS junctions

With the implementation of a semiconducting SNS junction instead of a conventional SIS tunneljunction the transport of Cooper pairs across the junction is now provided by Andreev reflection instead of tunneling processes. Andreev reflection can be sustained over a length scale of the coherence length of the material, while tunneling processes typically occur up to several nanometers. Consequently, the proximitized superconducting gap within a semiconducting junction often shows subgap states in contrast to the conventional SIS case, as shown in Figure 5.11a-b. These subgap states allow for dissipative and incoherent transfer of quasiparticle excitations across the gap when the correct bias voltage is met (Figure 5.11c-d). Generally the number of subgap states increase closer to the gap edge, as seen in [13].

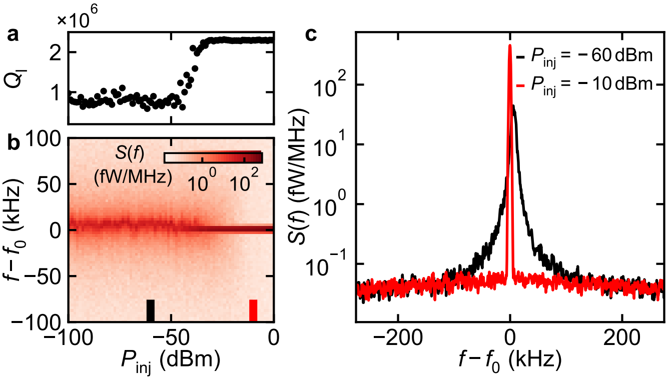

Figure 5.9: **Injection locking.** **a** Extracted quality factor from **b** $S(f)$ with increasing P_inj showing injection locking from −40 dB m. **c** Linecuts before and after injection locking demonstrating measurement limited linewidth narrowing.

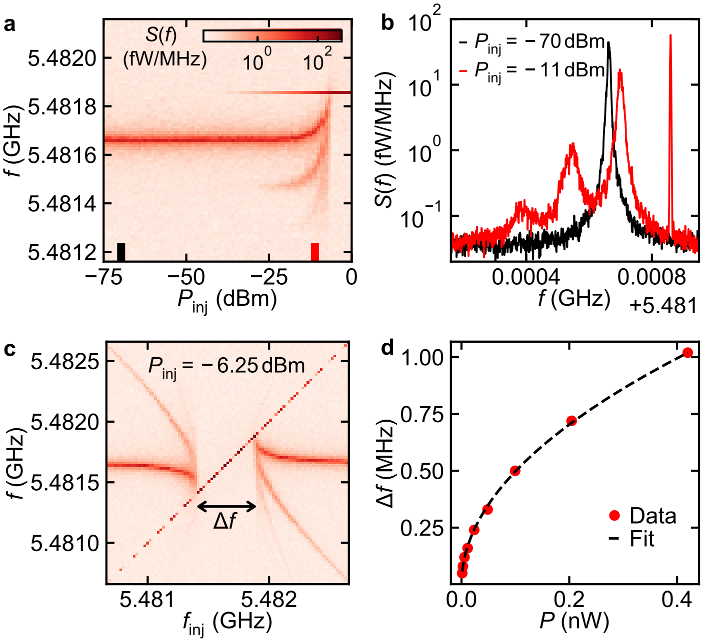

Figure 5.10: **Injection pulling.** **a** Emission $S(f)$ gets pulled towards the injected tone with increasing P_inj creating a frequency comb. Further increase locks the Josephson radiation to the injected frequency. **b** Linecuts showing slight pulling (black) and significant pulling resulting in a frequency comb (red). **c** $S(f)$ as a function of frequency of the injected tone for an input power P_inj =−6.25 dB m showing creation of sidebands and a locking range of 0.5 MHz. **d** Locking range dependence on power at the device, well-fitted by Adler's theory with α = 50 GHz/$\sqrt{\mathrm{W}}$.

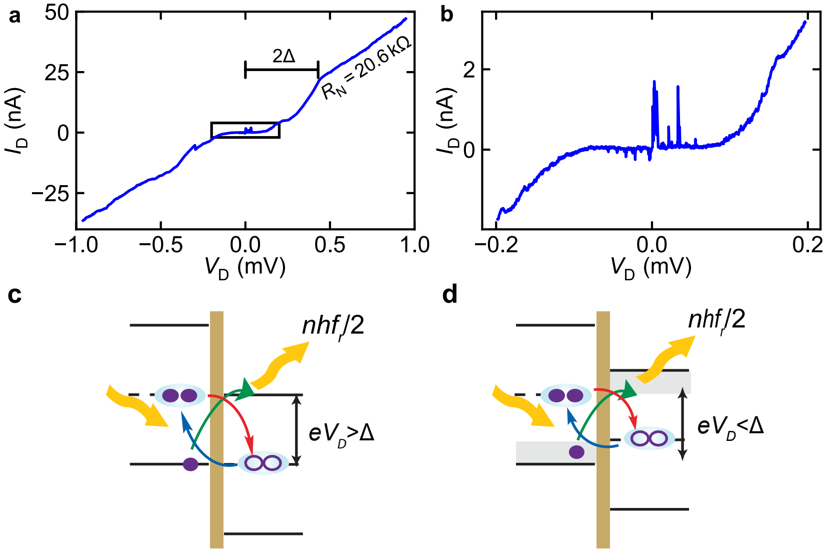

Figure 5.11: **Impact of softgap profile. a** Zoomed out IV-curve featuring soft gap characteristics. The superconducting gap is determined to correspond to $2\Delta = 0.43$ meV and a linear fit gives a outer gap normal resistance of $R_N = 20.59 \pm 0.04$ kΩ. **b** Zoom in showing the onset of the subgap currents and the simultaneous absence of higher order tunneling currents. **c** In a SIS junction made with Al/AlO$_x$/Al, the hard superconducting gap allows for lasing at voltage biases all the way up to the superconducting gap $eV_{\mathrm{cutoff}} = \Delta$. Once the voltage bias exceeds Δ, absorption of radiation at $hf = \Delta$ excites quasiparticles across the junction, preventing further stimulated emission. **d** In a proximitized nanowire, there is a significant density of states that can host quasiparticles within the superconducting gap. This results in a much lower V_{cutoff} than as seen in the SIS junction.

5.5.6. Autocorrelation Analysis

First the voltage bias is set to maximum emission intensity for each emission peak. Then ten 10 ms real-time measurements of the IQ-quadratures of the cavity output signal are recorded with a sampling rate of 100 MHz. Coherence times are extracted by computing the autocorrelation for each 10 ms recording and fitting with an exponential decay of the form:

$$g^{(1)}(\tau) = Ae^{\left(\frac{-\tau}{\tau_{\text{coh}}}\right)^{p}} \tag{5.1}$$

where A is a renormalisation factor, τ_{coh} the coherence time and p relates to the origin of broadening in case of chaotic light. An example of a typical full 10 ms autocorrelation belonging to $n = 4$ is shown in Figure 5.12a and is well-fitted by Equation (5.1) with $\tau_{\text{coh}} = 288.97 \pm 0.03$ µs. The result of all autocorrelation measurements are shown in Figure 5.12b. The average coherence times and corresponding standard deviations for each emission peak are computed from the ten measurements and are shown in the main text. At the start of all measurements we observe a sudden drop of $g^{(1)}(\tau)$ from 1, meaning perfect overlap, to a lower value before an exponential decay is observed. We attribute this to the relatively low signal-to-noise ratio (SNR), which in case of random thermal noise should give an on average constant reduction of the degree of overlap. Figure 5.12c shows the SNR, defined here as the radius R extracted from the IQ histograms with respect to the standard deviation σ of the Gaussian signal. To verify the validity of the additional renormalisation factor we compare the renormalisation factor obtained from the fitted autocorrelations to the SNR (Figure 5.12d). Worth noting is the small standard deviation in A, while the corresponding extracted coherence times show relatively a much bigger spread. Moreover, the fact that the renormalisation factor is proportionally equivalent to the SNR supports the claim that the sudden drop is caused by erratic perturbations due to thermal noise. Interestingly, we also see that the exponent p is showing the same trend as the SNR. A more indepth study of the relation of the exponent p to the corresponding coherence times is shown in Figure 5.12e. We observe a general decrease of p with increasing τ_{coh} for all emission modes. When we exclude the last emission mode from the analysis, since the additional effect of quasiparticle tunneling destructs the measured coherence times, we see p increases with the average emission amplitude $R(n)$ for similar coherence times. Concluding p, describing the degree of chaos, increases with the number of photons in the cavity. Which is determined by the number of photons that accompany a single Cooper pair tunneling event and by the coupling rate at which these tunneling events occur.

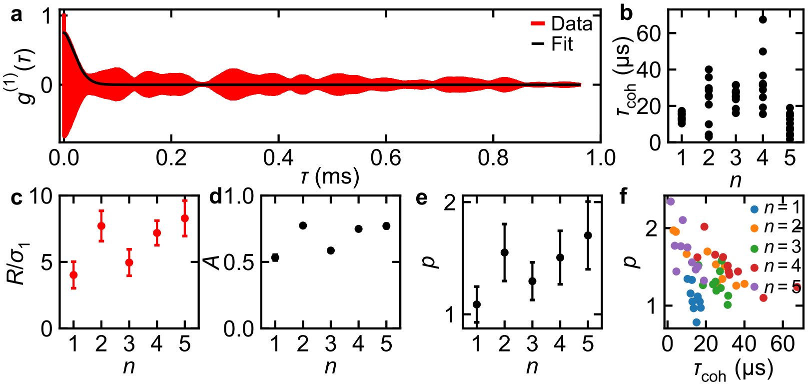

Figure 5.12: **Autocorrelation and fitting parameters.** **a** Example of a typical full-length autocorrelation (red) fitted by an exponential decaying function (black). **b** SNR of the different emission peaks in terms of radius R extracted from the IQ histograms with respect to their respective standard deviation σ. **c** Renormalisation factor A extracted from the exponential decaying fit to the autocorrelation for each emission peak. **d** Exponent p extracted from the exponential decaying fit of the autocorrelations for each emission peak.

5.5.7. Poisson distributed switching process

To investigate the underlying temporal distribution governing the switching process between the lasing and thermal state at peak $n = 5$, the dwell times τ_{lasing} and τ_{thermal} were collected in histograms. The histograms were fitted by an exponential decaying function $p(\tau) = \frac{1}{\bar{\tau}} e^{\frac{-\tau}{\bar{\tau}}}$, with $\bar{\tau}$ the mean time spend in lasing or not lasing state. To enhance the visibility of deviations from an exponential decaying trend each bin is weighted by the respective dwell time, resulting in $\tau p(\tau)$. Following [24] theoretical predictions were computed, using the previously fitted coherence times $\bar{\tau}$ as input parameter and taking into account that the integral of the theoretical prediction should be equal to the total sum of counts in the histogram. To quantify the agreement of the data to the theoretical predictions, the fidelity is calculated via $F = \frac{\Sigma_i \sqrt{M_i P_i}}{\Sigma_i M_i}$. The resulting fidelities for both states were found to be $F_{\mathrm{lasing}} = 0.954$ and $F_{\mathrm{thermal}} = 0.624$.

References

[1] O'Malley, P. J. J. *et al.* Scalable Quantum Simulation of Molecular Energies. *Phys. Rev. X* **6**, 31007 (2016).

[2] Salathé, Y. *et al.* Digital Quantum Simulation of Spin Models with Circuit Quantum Electrodynamics. *Phys. Rev. X* **5**, 21027 (2015).

[3] Kou, A. *et al.* Fluxonium-Based Artificial Molecule with a Tunable Magnetic Moment. *Phys. Rev. X* **7**, 31037 (2017).

[4] DiCarlo, L. *et al.* Demonstration of two-qubit algorithms with a superconducting quantum processor. *Nature* **460**, 240 (2009).

[5] Barends, R. *et al.* Coherent Josephson Qubit Suitable for Scalable Quantum Integrated Circuits. *Phys. Rev. Lett.* **111**, 80502 (2013).

[6] Cassidy, M. C. *et al.* Demonstration of an ac Josephson junction laser. *Science* **355**, 939–942 (2017).

[7] Simon, S. H. & Cooper, N. R. Theory of the Josephson Junction Laser. *Phys. Rev. Lett.* **121**, 027004 (2018).

[8] Astafiev, O. *et al.* Single artificial-atom lasing. *Nature* **449**, 588–590 (2007).

[9] Chen, F. *et al.* Realization of a single-Cooper-pair Josephson laser. *Phys. Rev. B* **90**, 20506 (2014).

[10] Liu, Y.-Y. *et al.* Semiconductor double quantum dot micromaser. *Science* **347**, 285–287 (2015).

[11] Krogstrup, P. *et al.* Epitaxy of semiconductor–superconductor nanowires. *Nature Materials* **14**, 400 (2015).

[12] Gazibegovic, S. *et al.* Epitaxy of advanced nanowire quantum devices. *Nature* **548**, 434 (2017).

[13] Chang, W. *et al.* Hard gap in epitaxial semiconductor–superconductor nanowires. *Nat Nano* **10**, 232–236 (2015).

[14] Larsen, T. W. *et al.* Semiconductor-Nanowire-Based Superconducting Qubit. *Phys. Rev. Lett.* **115**, 127001 (2015).

[15] de Lange, G. *et al.* Realization of Microwave Quantum Circuits Using Hybrid Superconducting-Semiconducting Nanowire Josephson Elements. *Phys. Rev. Lett.* **115**, 127002 (2015).

[16] Plugge, S., Rasmussen, A., Egger, R. & Flensberg, K. Majorana box qubits. *New Journal of Physics* **19**, 12001 (2017).

[17] Hyart, T. *et al.* Flux-controlled quantum computation with Majorana fermions. *Phys. Rev. B* **88**, 35121 (2013).

[18] Karzig, T. *et al.* Scalable designs for quasiparticle-poisoning-protected topological quantum computation with Majorana zero modes. *Phys. Rev. B* **95**, 235305 (2017).

[19] Hays, M. *et al.* Direct Microwave Measurement of Andreev-Bound-State Dynamics in a Semiconductor-Nanowire Josephson Junction. *Phys. Rev. Lett.* **121**, 047001 (2018).

[20] Liu, Y.-Y. *et al.* On-Chip Quantum-Dot Light Source for Quantum-Device Readout. *Phys. Rev. Applied* **9**, 014030 (2018).

[21] van Woerkom, D. J., Geresdi, A. & Kouwenhoven, L. P. One minute parity lifetime of a NbTiN Cooper-pair transistor. *Nature Physics* **11**, 547–550 (2015).

[22] Adler, R. A Study of Locking Phenomena in Oscillators. *Proceedings of the IRE* **34**, 351–357 (1946).

[23] Stover, H. & Steier, W. Locking of laser oscillators by light injection. *Appl. Phys. Lett.* **8**, 91 (1966).

[24] Vool, U. *et al.* Non-Poissonian Quantum Jumps of a Fluxonium Qubit due to Quasiparticle Excitations. *Phys. Rev. Lett.* **113**, 247001 (2014).

6

Offset-charge sensitive gatemon qubits in magnetic field

W. Uilhoorn, J. G. Kroll, A. Bargerbos, C. K. Yang, P. Krogstrup, L. P. Kouwenhoven, B. van Heck, A. Kou, G. de Lange

Gate-tunable hybrid semiconductor-superconductor nanowire Josephson junctions (JJs) hold great potential for superconducting quantum computation. Besides, these structures are particularly suitable for mesoscopic JJ research, as the conduction is carried by only a few near-ballistic modes. Here we perform microwave spectroscopy on such nanowire JJs by integrating them in an offset-charge sensitive transmon configuration, realising gatemons. We use both InAs−Al and InSb−Al nanowires. For the InAs gatemons we find the transparencies of the conduction modes to approach unity, as evidenced by the rapid suppression of the charge dispersion. Additionally, we study the magnetic field compatibility of the InAs-based qubit, using its coherence as the metric. We demonstrate coherent manipulation of the qubit state up to $B_{\parallel} = 0.5\,\mathrm{T}$ *(*$T_1 = 35 \pm 3$ ns *and* $T_2^{\mathrm{Echo}} = 53 \pm 9$ ns*); a regime relevant for topological quantum computation. Finally we develop the first InSb-based gatemon. A qualitative comparison between both materials shows a lower performance for the InSb-based devices. We conject that the origin lies in residual polymers due to the adjusted fabrication process to achieve working InSb−Al devices.*

Part of this chapter has been published by J. G. Kroll, *Magnetic field compatible hybrid circuit quantum electrodynamics* (2019) and a part has been published by A. Bargerbos *et al.* in *Physical Review Letter* **124**, 246802 (2020)

6.1. Introduction

Over the last decades, the conventional superconductor-insulator-superconductor (S-I-S) tunnel Josephson junctions (JJs) have proven to be a crucial element in quantum technologies, by introducing non-linearity in systems at low-loss. The Josephson coupling of a single JJ is fixed during device fabrication. This coupling can be made controllable when placing two JJs in parallel, forming a superconducting quantum interference device (SQUID), and threading the superconducting loop with a magnetic flux.

Today's leading quantum computing platform, the superconducting transmon qubit, is built upon this electrical component. The qubit consists out of an S-I-S JJ connected to a superconducting island, that acts as a shunt capacitor to ground. The ratio between the Josephson coupling E_J and the charging energy of the superconducting island E_C, sets the charge confinement on the island, and thereby the charge sensitivity of the qubit [1]. This charge-insensitive qubit design increased the energy relaxation times by several orders of magnitude, with the current record being $\sim$ 0.3 ms in planar on-chip architectures [2]. Yet the platform remains too noisy, prohibiting upscaling to large-scale quantum processors.

With the emergence of high quality semiconducting JJs, novel transmon qubits have been realised, where the SQUID is exchanged for a single semiconductor JJ, enabling simple voltage-control of E_J [3–9]. This design is suitably called the gatemon. The voltage-control renders the gatemon insensitive to flux noise, and mitigates associated cross-talk between qubits as well as heating issues. Thus providing potential advantages over the conventional transmons in terms of scalability. Gatemons based on hybrid semiconductor-superconductor (SM-SC) nanowire JJs have proven to be viable alternatives with single-qubit fidelities over 99% and two-qubit controlled-phase gates with fidelities around 91% [10].

Furthermore, the advancement of the gatemon provides a novel platform to probe mesoscopic phenomena of semiconductor JJs at high bandwidths. In contrast to their conventional counterpart, the super current in semiconductor JJs is carried by only a small number of highly transmitting modes [11–13], leading to a non-sinusoidal current-phase relation that affects the anharmonicity of the gatemon spectrum [5]. Moreover, gatemons in the charge-sensitive regime make ideal high-bandwidth detectors for investigating near-ballistic single charge transport. But most interest in hybrid superconducting qubits comes from their potential to construct new and exotic qubits, including the Andreev qubit [14, 15], parity-protected qubits based on unusual π-periodic JJs [16, 17], spin-ensemble qubits [18], and qubits based on Majorana zero modes [19]. The hybrid JJ platform is particularly suitable for the two latter proposals, because of its semiconducting nature in combination with their magnetic field compatibility.

Here we develop the gatemon architecture in the offset-charge sensitive (OCS) regime, using a proximitized InAs nanowire [20]. We control the offset-charge n_g with an additional electrode that extends over the length of the nanowire. This enables us to investigate the charge dispersion in the few mode regime. By in-situ tuning of the transparency of the weak-link, using an electrostatic gate, we observe its charge dispersion to decrease by almost two decades in frequency at a rate far exceeding exponential suppression in E_J/E_C. The observed gate dependence of the charge dispersion is modelled by

Table 6.1: Device parameters of the devices presented in this chapter.

	f_{bare} (GHz)	$\kappa/2\pi$ (MHz)	E_C (GHz)
Device A	5.518	4.972	~0.6
Device B	5.201	2.591	~0.6
Device C	5.340	3.207	~ 0.6
Device D	5.351	1.239	~0.6
Device E	5.321	0.997	~0.6

tunnelling through a resonant level, incorporating the effect of imaginary time Landau-Zener tunnelling. This model agrees well with the measured suppression of charge dispersion, suggesting near-unity JJ transparency.

After probing the mesoscopic behaviour of the JJ, we demonstrate the magnetic field compatibility of the device as a whole. A crucial ingredient in the search for Majorana signatures in microwave circuits. We measure the performance of the transmon in magnetic field using the energy relaxation and phase coherence as figure of merit. Coherent manipulation is shown up to $B_\parallel = 0.5\,\text{T}$, exceeding previous transmon records by a factor of three [21–23].

Finally we develop the first gatemon based on InSb, and report on its compatibility in magnetic field. However, the device quality needs to be improved before the material platform could be exploited to search for Majorana features in the microwave regime.

6.2. Methods

6.2.1. Device design

Four separate devices, referred to as device A to D, were used throughout this chapter, all with similar superconducting circuitry but differing in NW materials and electrostatic gate patterns. Figure 6.1a shows a stitched scanning electron microscope image of the general design, where a $\lambda/2$ superconducting coplanar waveguide (CPW) resonator is used to readout a transmon qubit. The frequencies of the fundamental modes and corresponding line widths for all devices are given in Table 6.1. The resonator is rendered resilient to magnetic fields via the fabrication process described in Section 3.1.1. To increase the measured signal collected from the CPW, we design the in- and output ports to be asymmetric, such that the photon emission rate κ_i out of the input port is much less than the emission rate κ_o out of the output port, which connects to the measurement detection setup. Two transmons are capacitively coupled to the resonator both with a coupling strength of $g \simeq 100\,\text{MHz}$, each is placed at one of the two electric field anti-nodes of the resonator's fundamental mode. Figure 6.1b shows the single island configuration of the right transmon with $E_C \simeq 0.6\,\text{GHz}$ (left transmon: $E_C \simeq 1.2\,\text{GHz}$). The Josephson junction (JJ) is made from a semiconductor nanowire with an aluminium epitaxial shell on two facets, previously shown to exhibit hard proximity-induced superconducting gaps [24]. Devices A and B are based on InAs−Al NWs [20], and devices C, D

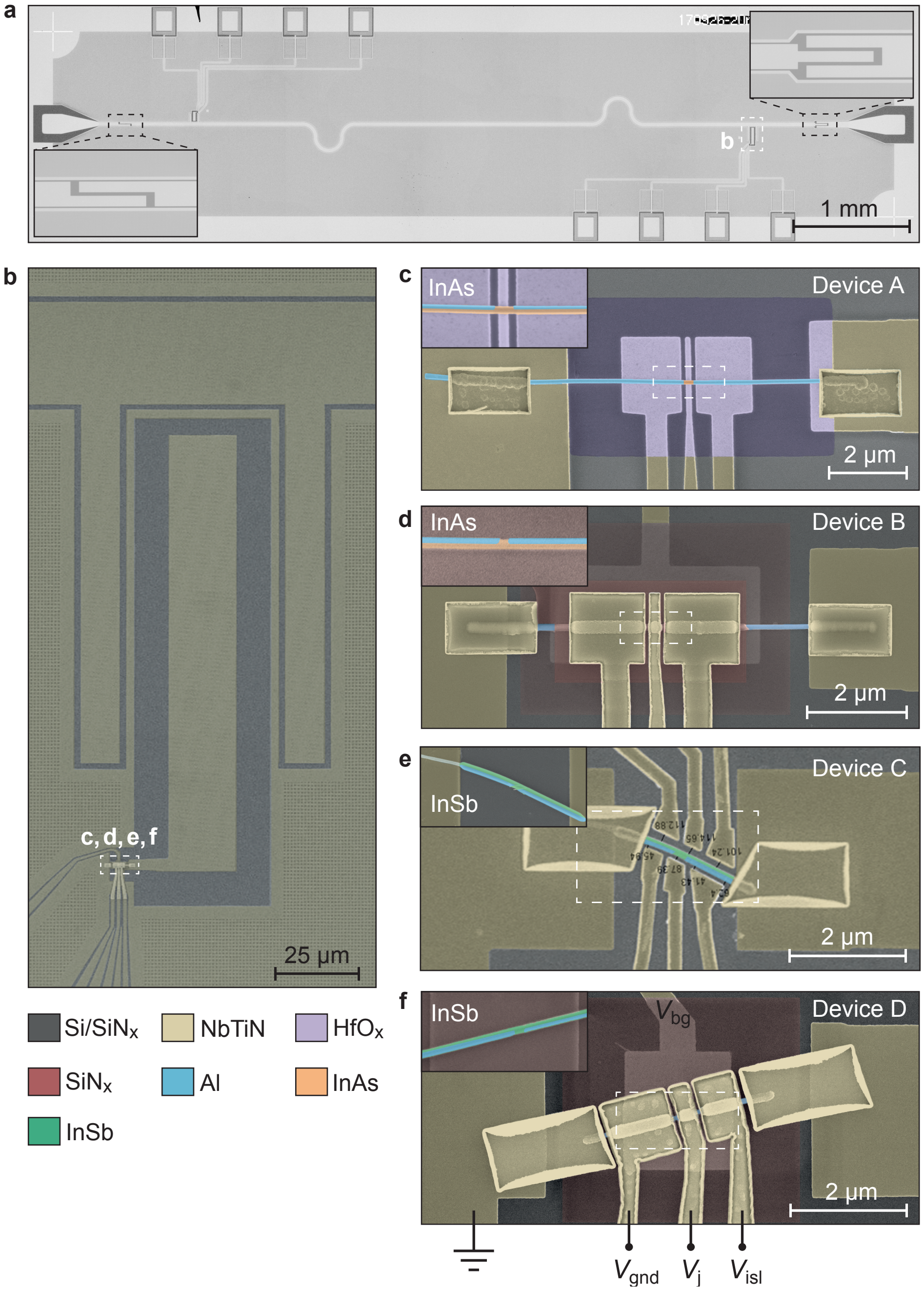

Figure 6.1: **NW transmon designs for InAs and InSb.** Scanning electron microscopy images showing **a** the overview of the 2×7 mm chip showing the $\lambda/2$ CPW resonator. Insets provide a zoom in of the asymmetric capacitive couplers where the output coupler is more strongly coupled then the input coupling. **b** NW transmon qubit with a single capacitor plate configuration that is capacitively coupled to the resonator. Electrostatic gates are designed to control the conduction properties along the NW. **c** Bottomgate and **d** wrapgate design for InAs material. Insets show the NW with partial Al shell and etched JJs.**e** Side gate and **f** wrapgate design for InSb. Insets show the NW with partial Al shell and in-situ evaporated JJs.

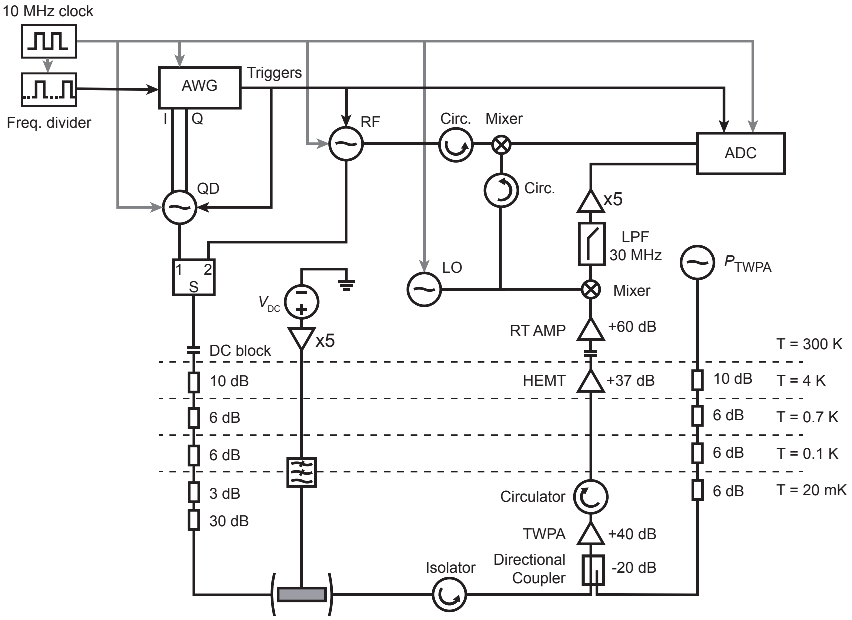

Figure 6.2: **Measurement circuit.** Standard heterodyne measurement techniques are used to measure the complex transmission S_{21} while the sample is tuned via the low noise dc voltages sources.

and E are based on InSb−Al NWs [25]. An in-depth overview on the InAs−Al and InSb−Al platforms is provided in Section 3.1.3. For all devices electrostatic gates are used to manipulate the conduction channels in the NW. On-chip LC-filters on each gate electrode act as low pass filters to suppress microwave dissipation through the capacitively coupled gates [26]. Figure 6.1(c-f) shows the specific gate pattern of the devices. Generally all devices have two plunger gates straddling the JJ, denoted by the voltages V_{isl} and V_{gnd}, controlling the local chemical potential and electric-field tunable superconducting gap in the proximity-induced NW sections [27]. All devices are also equipped with an electrode located at the JJ which is controlled by V_{j}, to alter the Josephson energy E_{J} [28], and with that the qubit frequency f_{01} [3, 4, 21]. For device B, D and E, the plunger and JJ electrodes are fabricated to wrap around the NW as top gates, enhancing their coupling strength to the NW. In this configuration an ancillary back gate, V_{bg}, is added that spans over the NW segments gated by V_{isl}, V_{gnd} and V_{j}. This combination adds another knob to influence the electron density in the NW, and offers the control to lift potential barriers created in the NW due to the finite spacing between the plunger gates and the JJ electrode. To elucidate the design architectures and their differences, an overview of the fabrication steps for each device is shown in Table 6.2.

6.2.2. Measurement setup

All measurements were performed in a dilution refrigerator with a base temperature of 25 mK equipped with a 3-axis vector magnet. The sample was packaged in a copper en-

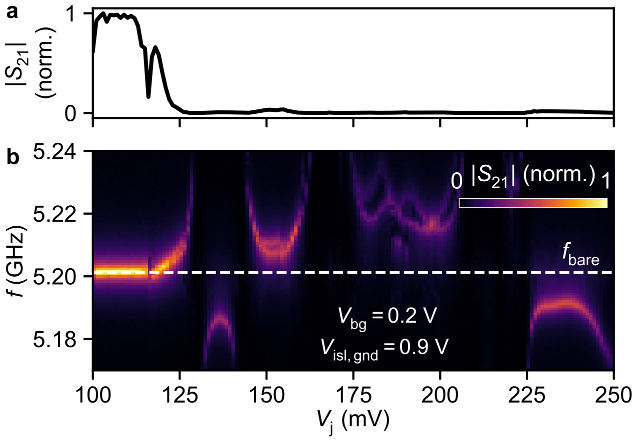

Figure 6.3: **Onset InAs device.** Data obtained from device B. **a** $|S_{21}|$ as function of V_{j} at fixed readout frequency set to f_{bare}, showing the onset of the device around 125 mV. **b** $|S_{21}|$ as a function of readout frequency f versus V_{j}, demonstrating avoided crossings when the transmon is tuned from below to above f_{bare}. With increasing V_{j} we observe non-monotonic behaviour of χ_{01} with multiple anti-crossings, typical for few mode semiconducting NWs.

closing with extra layers of eccosorb material as described in Section 3.2. During the experiments all gate electrodes are set at a constant dc voltage using low noise dc voltage sources, while microwave sources are used to prepare the system's ground and excited energetic states. Microwave spectroscopy is then performed utilizing the heterodyne measurement scheme as depicted in Figure 6.2. The dc voltage lines are thermally anchored at each stage. At the mixing chamber the dc lines are heavily filtered by RC, π and copper powder filters before they connect to the gates via the on-chip LC-filters. The microwave input line is heavily attenuated to reduce noise and thermal excitation of the cavity, enabling single photon occupancy in the cavity. The microwave output line is amplified at three stages, first the signal is amplified at the mixing chamber by a travelling-wave parametric amplifier (TWPA) powered via a directional coupler then by a high electron mobility transistor (HEMT) at 4 K and finally at room temperature. An isolator is placed directly at the output of the sample to shield the sample from thermal noise originating from the amplification circuit. For the same reason a circulator is placed between the HEMT and TWPA. Standard heterodyne measurement techniques are used, where the arbitrary waveform generator (AWG) controls the timing of the measurement sequence and provides the pulses to drive the qubit. The qubit drive (QD) is added to the radio-frequency (RF) readout tone that is presented to the input of the resonator. Both the outgoing signal and the reference arm signal are down converted using a local oscillator and recorded by a fast analogue to digital converter (ADC). The comparison of the two yields the sample response, i.e. the amplitude and phase response of the complex transmission S_{21}. Two circulators placed at the reference arm ensure that the reference arm signal does not leak into the cavity.

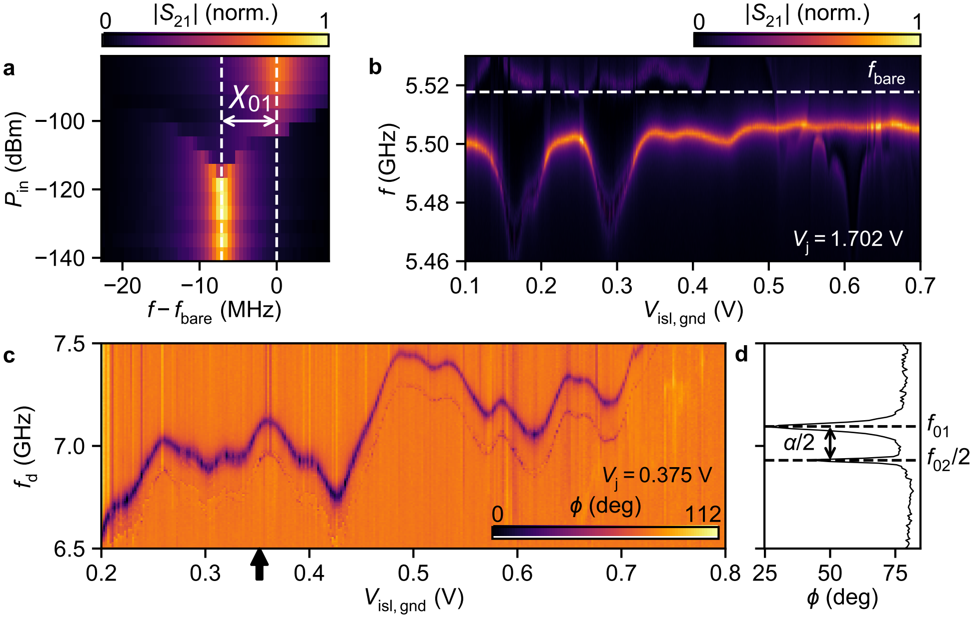

Figure 6.4: **InAs device characterisation.** Data obtained from device A. **a** $|S_{21}|$ as a function of readout frequency f versus P_{in}. As P_{in} is reduced, the resonator experiences a dispersive shift χ_{01} due to the coupling to a transmon transition above f_{bare} at single photon occupancy. **b** $|S_{21}|$ as a function of readout frequency f versus V_{j} shows a non-monotonic behaviour of χ_{01} by changing the JJ properties, demonstrating avoided crossings when the transmon is tuned from below to above f_{bare}. **c** Monitoring ϕ of S_{21} at f_{r} as a function of the qubit drive frequency f_{d} versus the plunger gate voltages $V_{\text{isl,gnd}}$ shows a generally increasing trend for the f_{01} and f_{02} qubit transitions with increasing $V_{\text{isl,gnd}}$ due to cross coupling to the JJ. **d** Linetrace taken at the black arrow in *c* showing the two lowest qubit transitions.

6.3. Results InAs nanowire transmon

Initial characterization of the different nanowire transmon devices showed similar behaviour, concluding that the specific gate design did not significantly affect the working principle of the devices and justifying a collective representation of the datasets.

6.3.1. Qubit characterization

The device is characterised at base temperature and in the absence of an applied magnetic field, where the readout resonator is driven by a continuous wave tone. First we determine the required V_{j} to increase the qubit's transition frequency f_{01}, such that it imposes a partial dispersive shift χ_{01} on the resonator. For this reason we start by probing the response at the bare resonator frequency and vary V_{j}, where the input power P_{in} is set to be sufficient to occupy the resonator with just a single photon ($\langle n_{\text{ph}} \rangle \simeq 1$). Typically we find onset values of $V_{\text{j}} = 100$ mV to 300 mV. Figure 6.3a shows the calibration for device B, where the onset occurs around $V_{\text{j}} \simeq 125$ mV. Similarly, we can perform the measurement while varying the readout frequency f, as shown in Figure 6.3b, revealing an anti-crossing at the onset value of V_{j}. The reproducible, non-monotonic V_{j}-dependence of f_{01} is consistent with mesoscopic conductance fluctuations that have been observed in semiconducting JJs both in direct dc conductance measurements [11, 12] and in microwave devices [3, 4, 6, 29]. Once the onset value is known, we can characterize the remaining responses of the gates on the device. We start with the calibration of the input power P_{in} where we sweep the readout tone f as function of P_{in} to vary $\langle n_{\text{ph}}\rangle$ of the resonator from ~ 1000 to 1 while recording $|S_{21}|$, as shown in Figure 6.4a. Upon low enough $\langle n_{\text{ph}}\rangle$ the resonator hybridizes with the qubit, as displayed by the partial dispersive shift χ_{01} [1]. Due to finite stray capacitance, f_{01} can also be tuned using the plunger gates, as monitored by varying V_{isl} and V_{gnd} simultaneously (Figure 6.4b). Several other anomalous states are observed to couple to the resonator, which may occur due to environmental two-level systems or accidental quantum dot states in the JJ. Finally we perform two-tone spectroscopy to directly probe the qubit's energy transitions as a function of $V_{\text{isl,gnd}}$. Figure 6.4c shows both the ground state to first excited state transition f_{01}, as well as the two-photon transition from the ground state to second excited state $f_{02}/2$. Again showing a reproducible and non-monotonic response. The measured anharmonicity $\alpha = h(f_{12} - f_{01}) \sim$ 400 MHz shows moderate suppression from the expected value of $\alpha \simeq -E_C \simeq -600$ MHz, suggesting that the JJ is in the few mode high transparency limit, which can reduce α to as little as $E_C/4$ [5].

6.3.2. Charge dispersion suppression

The nanowire transmon is designed to be moderately offset-charge-sensitive, having an $E_{\text{J}}/E_C \simeq 14$ when $f_{01} \simeq f_{\text{bare}}$. In this way we can measure the dependence of the qubits ground state to first excited state transition frequency on the offset charge of the island ($f_{01}(n_{\text{g}})$) using two-tone spectroscopy (Figure 6.5a). Each measurement results in two sinusoidal curves shifted by half a period, belonging to qubit transitions for even and odd island fermion-parity. Their simultaneous detection is caused by quasiparticle poisoning on timescales faster than the measurements [30]. We define the qubit frequency f_{01} as the point of charge degeneracy between even and odd island parity and the charge dispersion δf_{01} as the maximal frequency difference between the two parity states, reflecting the maximal energy cost of charging the island with an additional electron. As expected, the charge dispersion decreases with increasing qubit frequency, as measured by varying V_{j} and summarized in Figure 6.5b. We observe $\delta f_{01} = 679$ MHz at $f_{01} = 3.539$ GHz compared to $\delta f_{01} = 39$ MHz at $f_{01} = 4.629$ GHz, as shown by the individual charge dispersion measurements in Figure 6.5a. To gain further insight we plot the δf_{01} versus f_{01} (Figure 6.5c) using the data from Figure 6.5b. The rise in f_{01}, increasing by a factor of 1.35, is accompanied by a strong decrease in δf_{01} by almost two orders of magnitude. We calculate that the rapid decrease cannot be accounted for by the standard SIS transmon model with sinusoidal potential, as shown by the grey solid line in Figure 6.5c.

This leads us to develop a quantitative understanding of the device using a simplified model of the resonant level model [31–34], where two superconducting leads host a resonant level in between, as depicted schematically in Figure 6.5d. We consider the presence of a single spin-degenerate level in the JJ. The level has an energy ϵ_0 relative to the Fermi level, and is coupled to two identical superconductors with superconducting gap Δ via the (spin-degenerate) tunnel rates Γ_{l} and Γ_{r}. The model is a simplification as it does

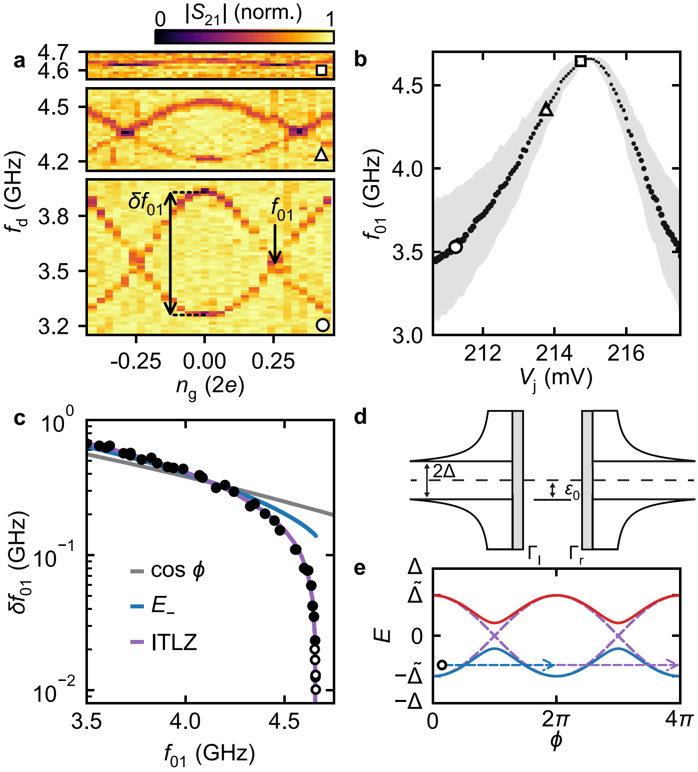

Figure 6.5: **Charge dispersion suppression.** Data obtained from device B. **a** Examples of two-tone spectroscopy measurements taken at V_j, as indicated by the open markers in *b*. $|S_{21}|$ shows the $0 \rightarrow 1$ transition versus the offset charge tuned by V_{isl}, where an oscillation of $2e$ corresponds to $\sim$ 50 mV. **b** Evolution of f_{01} (markers) and δf_{01} (shading and marker size) versus V_j. **c** Same data as in *b* plotted as δf_{01} versus f_{01}. Solid lines show fits using three different models of $U(\phi)$: a standard transmon sinusoidal potential, the negative energy ABS branch of the resonant level model, and with the addition of ITLZ tunnelling between both ABS branches. **d** Schematic illustration of a resonant level coupled to two identical superconducting leads. **e** Energy-phase dependence of the ABS in the resonant level model for $\tilde{D} = 0.9$ (solid) and $\tilde{D} = 1$ (dashed) with $\Gamma = \Delta$. Arrows indicate the available quantum tunnelling trajectories for the two cases.

not include the electron-electron interactions of the quantum dot. The potential of the JJ $U(\phi)$ is determined by the energies of a single pair of spin degenerate Andreev bound states (ABS) as shown in Figure 6.5e. Their energies have to be calculated numerically for general parameter values but can be expressed analytically in certain limits [33, 34]:

$$\begin{gathered} E_{\pm}(\phi) = \pm\tilde{\Delta}\sqrt{1-\tilde{D}\sin^2\phi/2} \\ \tilde{D} = \frac{4\Gamma_{\mathrm{l}}\Gamma_{\mathrm{r}}}{\epsilon_0^2+\Gamma^2}, \qquad \tilde{\Delta} = \begin{cases} \Delta, & \text{if } \Gamma \gg \Delta, \epsilon_0 \\ \Gamma, & \text{if } \Gamma \ll \Delta \text{ and } \epsilon_0 \end{cases} \end{gathered} \tag{6.1}$$

where $\Gamma = \Gamma_{\mathrm{l}} + \Gamma_{\mathrm{r}}$. Here the ABS takes on the same form as a superconducting quantum point contact (SQPC) [35], but with an effective superconducting gap $\tilde{\Delta} < \Delta$. The form of the effective JJ transparency $\tilde{D}$ also explicitly reflects a Breit-Wigner type resonant tunnelling process, maximized for equal tunnel rates ($\delta\Gamma = |\Gamma_{\mathrm{l}} - \Gamma_{\mathrm{r}}| = 0$) and particle-hole symmetry ($\epsilon_0 = 0$).

Following this model under the typical assumptions of low to moderate values of $\tilde{D}$ and $\tilde{\Delta} \gg E_C, k_{\mathrm{B}}T$, only the ground state of the JJ is occupied such that charge transfer occurs through E_-, leaving the upper branch unoccupied. In this regime, the charge dispersion is exponentially suppressed in $\tilde{\Delta}\tilde{D}/E_C$, and governed by tunnelling of the phase under the potential barrier of E_- as found in the case of tunnel junctions [1, 36]. When we fit the measured dependence of δf_{01} on f_{01} with a potential considering only the E_- branch of the resonant level model, we observe a slight improvement (solid blue line Figure 6.5c) over the standard sinusoidal potential. However, the model in this limit still does not capture the full charge dispersion suppression.

But when we consider $\tilde{D} \to 1$, the energy gap between the ABS vanishes, and the energy spectrum of the JJ is characterized by a narrowly avoided level crossing at $\phi = \pi$. This allows for imaginary time Landau-Zener (ITLZ) tunnelling [37, 38] and prevents quantum tunnelling trajectories from reaching the energy minimum at $\phi = 2\pi$, as indicated by the arrows in Figure 6.5e. The probability amplitude for the quantum tunnelling trajectory to stay in the lower ABS branch now vanishes linearly with the reflection amplitude $\sqrt{1-\tilde{D}}$ [37, 39]. As a consequence 2π-tunnelling processes are suppressed, and so is the charge dispersion. When $\tilde{D} = 1$, the charge dispersion saturates to a small value defined by tunnelling through a 4π-wide potential barrier given by $\tilde{\Delta}\cos\phi$. This resonant level model including ITLZ tunnelling shows accurate agreement over the whole range including the strong charge dispersion suppression (purple solid line Figure 6.5c) and confirms the requirement for transparencies close to unity. The data and fit clearly demonstrate reaching the diabatic regime of ITLZ tunneling. In order to fit the data we assumed that V_{j} only alters ϵ_0, while $\Gamma_{\mathrm{l}} = \Gamma_{\mathrm{r}}$ are held constant. Furthermore, we fixed $\Delta = 62$ GHz based on temperature dependence measurements of the quasiparticle poisoning time as presented in Figure 7.6. We find that $\Gamma = 23$ GHz, which gives an effective gap $\tilde{\Delta} = 16$ GHz at the point of maximal suppression. The numerical details of the procedure are described in [40].

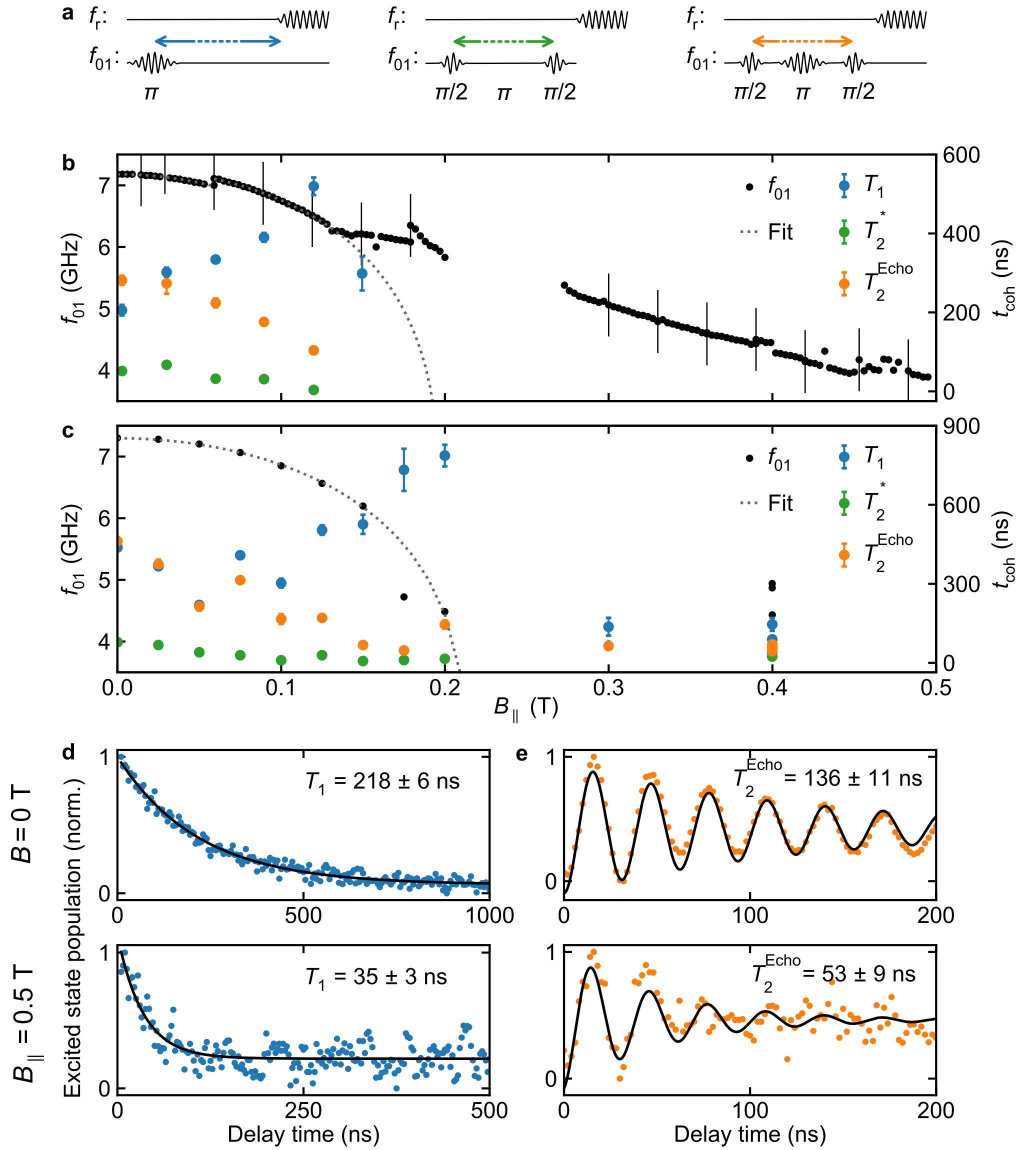

Figure 6.6: **Qubit coherence at magnetic field.** Data obtained from device A. **a** Pulse sequences used to perform a T_1 (left), T_2^* (middle) and T_2^{Echo} (right) measurement. Color-coded arrows represent the variable delay time of each measurement. **b** Magnetic field dependence of f_{01} (left axis) and coherence times T_1, T_2^* and T_2^{Echo} (right axis) at $V_j = 0.375$ V, $V_{\text{isl,gnd}} = 0.3$ V. Minimal magnetic field realignment was required at the stitch points indicated by vertical lines on the f_{01} measurements. **c** Same as in *b* at $V_j = 1.8$ V and $V_{\text{isl,gnd}} = 0.4$ V. **d** Qubit relaxation from the excited state by measuring the qubit state while varying the delay after a π-pulse, as depicted in *a*, yields $T_1 = 218 \pm 6$ ns for $B = 0$ T (top) and $T_1 = 35 \pm 3$ ns for $B_\parallel = 0.5$ T (bottom). **e** Phase coherence of the qubit measured by varying a delay time between two $\pi/2$-pulses with π-pulse in between to cancel slow noise, as depicted in *a*, demonstrates a dephasing time of $T_2^{\text{Echo}} = 136 \pm 11$ ns at $B = 0$ T (top) and $T_2^{\text{Echo}} = 53 \pm 9$ ns at $B_\parallel = 0.5$ T (bottom).

6.3.3. Magnetic field characterisation

For device A, f_{01}, T_1, T_2^* and T_2^{Echo} were tracked as function of $B_\parallel$ (Figure 6.6b,c), on two separate cool downs at two different gate settings. For $B_\parallel < 150\,\mathrm{mT}$, f_{01} drops parabolically with $B_\parallel$ and is well fitted by the reduction of the superconducting gap Δ based on BCS theory [21]:

$$f_{01}\left(B_\parallel\right) \approx f_{01}\left(B_\parallel = 0\,\mathrm{T}\right)\left(1-\left(\frac{B_\parallel}{B_\mathrm{C}}\right)^2\right)^{\frac{1}{4}} \tag{6.2}$$

We note that the critical magnetic field B_C differs for the two different gate settings, consistent with an electric-field tunable proximity-induced superconducting gap in the NW [27]. We find a typical value of $B_\mathrm{C} \sim 0.2\,\mathrm{T}$, which is much higher than the previously recorded values in transmon studies [21–23]. We attribute this enhancement to the thin and partial shell, covering only two facets of the nanowire. At higher magnetic fields the qubit frequency deviates from the trend predicted by BCS theory. Instead, we find that f_{01} decreases linearly for $B_\parallel > 0.125\,\mathrm{T}$ (Figure 6.6b). We hypothesize that this behaviour is caused by the supercurrent interference in few-mode nanowires due to the orbital effect of the magnetic field [41].

Figure 6.6a depicts the pulse sequences utilized to measure the energy relaxation time T_1, the coherence times T_2^* and T_2^{Echo}. The π-pulse, to excite the qubit, is calibrated through a Rabi oscillation measurement. Surprisingly, we find T_1 to increases with $B_\parallel$. Correlating the increase of T_1 with the observed enhancements of the parity lifetime presented in Chapter 7, suggests that the contribution of quasiparticle induced energy relaxation is significant [1, 42–46].

For T_2^*, we find a rather constant phase coherence time with increasing magnetic field. However, for T_2^{Echo}, where the Hahn-echo protocol reverses slow frequency dephasing, we observe a decrease with increasing $B_\parallel$. This suggests that there is a fast frequency dephasing mechanism that becomes more dominant at finite magnetic field.

Figure 6.6d shows typical T_1 measurements at $B = 0\,\mathrm{T}$ and at $B_\parallel = 0.5\,\mathrm{T}$, the highest magnetic field where we were able to perform pulsed measurements. Figure 6.6e shows the corresponding T_2^{Echo} measurements. The lifetimes are four orders of magnitude lower than the current records of transmons. But we like to stress that these sample were not optimized towards this end, but are optimized to be magnetic field compatible in the offset charge sensitive regime. The coherent manipulation up to $B_\parallel = 0.5\,\mathrm{T}$ is an achievement on its own considering previous experiments [21–23]. Subsequent results from our collaborators in similar devices [47] demonstrate narrow line widths and qubit coherence at $B_\parallel = 1\,\mathrm{T}$ for one of their devices, while for several other devices also reporting coherence up to $B_\parallel \sim 0.5\,\mathrm{T}$. The magnetic field compatibility of our devices demonstrates that the platform is well suited to probe magnetic field sensitive research, such as the investigation of ABSs in magnetic field and the pursuit of detecting topological features using spectroscopic techniques (see Section 2.4.5).

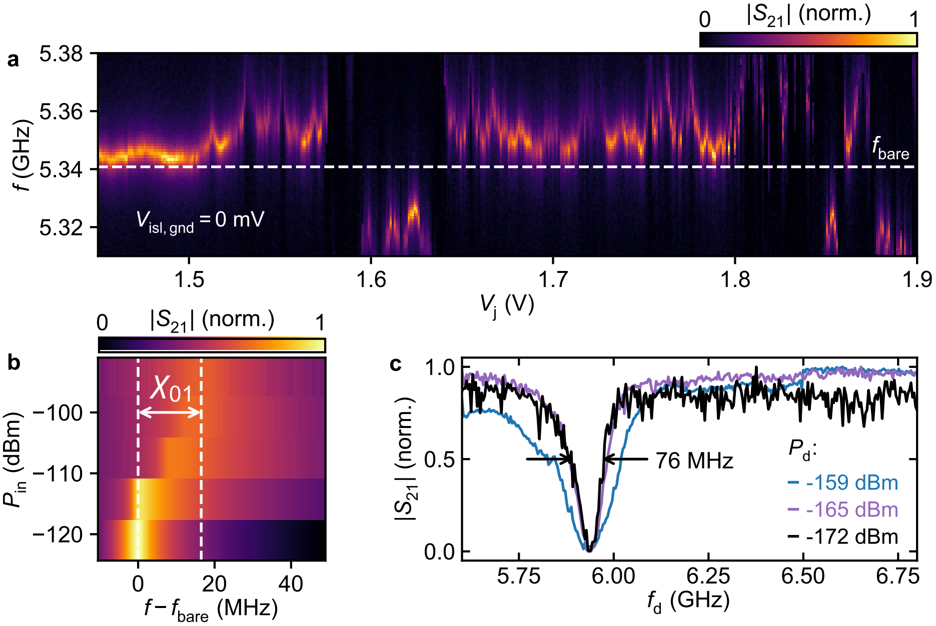

Figure 6.7: **InSb device characterisation.** Data obtained from device C. **a** $|S_{21}|$ as a function of readout frequency f versus V_j shows the non-monotonic behaviour of χ_{01}, demonstrating that the transmon can be tuned from below to above f_bare. **b** $|S_{21}|$ as a function of readout frequency f versus P_in. As P_in is reduced, the resonator experiences a dispersive shift χ_{01} due to the coupling to a transmon transition below f_bare at single photon occupancy. **c** Monitoring $|S_{21}|$ at $f_\mathrm{r} = 5.323$ GHz as a function of the qubit drive frequency f_d versus the qubit drive power P_d shows linewidth broadening and a minimum qubit linewidth of 76 MHz at the lowest drive power.

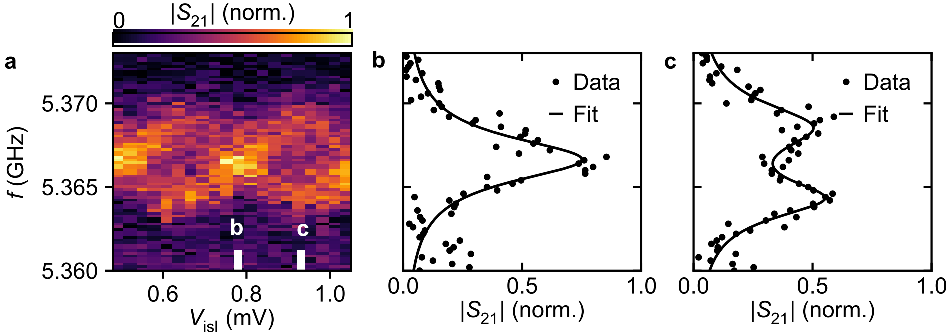

Figure 6.8: **InSb charge dispersion.** Data obtained from device D. **a**. Line trace at charge degeneracy fitted with a Lorentzian lineshape and **b** at maximum charge dispersion fitted with a double Lorentzian lineshape.

6.4. Results InSb nanowire transmon

6.4.1. Qubit characterisation

After having investigated the InAs−Al nanowire gatemons extensively, the nanowire material was switched for InSb−Al [25], requiring the development of room temperature fabrication techniques (see Section 3.1.3). Similar to its InAs−Al counterpart we show that the qubit frequency can be tuned by varying V_{j} when $\langle n_{\mathrm{ph}}\rangle \simeq 1$ (Figure 6.7a). For the particular side gate configuration of device C, we notice that the average threshold voltage to impose a partial dispersive shift χ_{01} on the resonator is roughly an order of magnitude higher, consistent with smaller capacitive coupling due to the increased distance between the gates and the nanowire. The power dependence of χ_{01} shows that the shift only occurs at a single photon occupancy in the cavity, verifying the coupling to a two-level system (Figure 6.7b). Using two-tone spectroscopy the f_{01} transition of the qubit can be probed directly, as shown by Figure 6.7c. Upon reducing the drive power, the qubit linewidth saturates at 76 MHz, while higher drive powers cause linewidth broadening. The saturated linewidth provides a lower boundary for the qubit's phase coherence of 2 ns. However, time domain measurements were unsuccessful in all InSb-based devices.

Also the InSb gatemons were designed to be offset-charge sensitive. However, only device D showed charge dispersion inherited by the resonator (Figure 6.8). Which we attribute to the inferior device quality.

Despite the device quality, we are able to observe dispersive shifts of the resonator at finite magnetic fields, as shown in Figure 6.9 for $B_{\parallel} = 0.4$ T. Demonstrating the magnetic field compatibility of the platform and showing great promise for future devices when better device quality is achieved.

6.4.2. Device instability in time

Attempts to coherently control the qubit with pulsed measurements were unsuccessful, motivating us to investigate the origin of these limitations. Figure 6.10a shows the

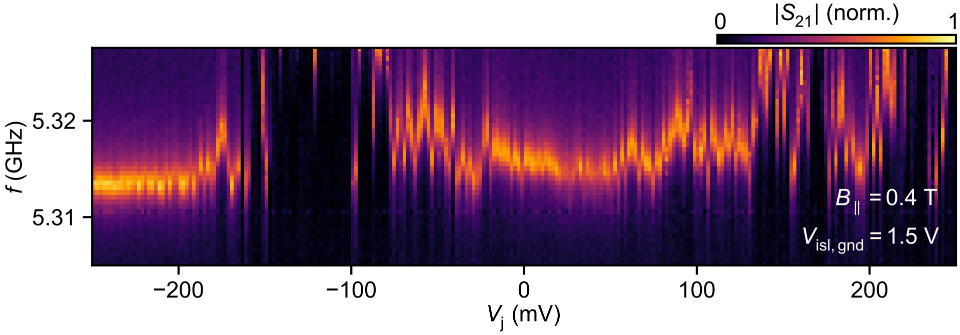

Figure 6.9: **InSb magnetic field compatibility.** Data obtained from device E. $|S_{21}|$ as a function of readout frequency f versus V_j demonstrating qubit response at $B = 0.4\,\mathrm{T}$.

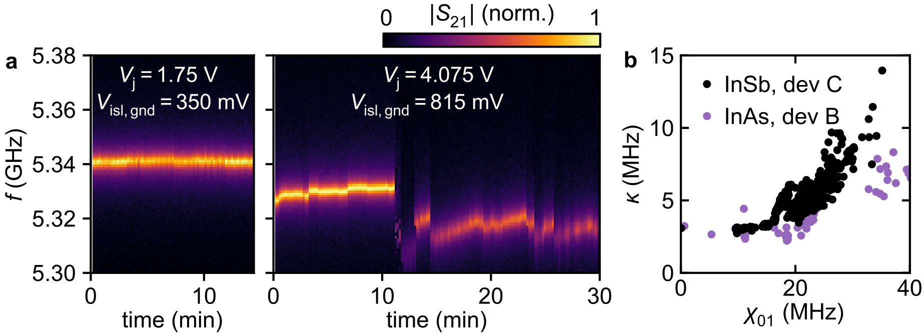

Figure 6.10: **Losses InSb transmon.** Data obtained from device C. **a** Monitoring $|S_{21}|$ as a function of readout frequency f over time. Stability of the system when the qubit is tuned far away from the resonator (left) and close to the resonator (right). **b**. Linewidth κ versus χ_{01} extracted from *a (right panel)* compared to extracted values for a nominally identical InAs device.

resonator response over time when measuring $|S_{21}|$ at fixed gate settings in the regime where the qubit frequency is tuned far from the resonator (left) and where the qubit is tuned to be close by the readout resonator frequency (right). A stable resonator response is measured when the qubit is not imposing a shift on the resonator, however when the qubit is tuned close to the resonator f_r jumps erratically. We extract the resonator linewidth κ and χ_{01} by fitting each trace with a Lorentzian line shape. The relation shows higher losses when the resonator state becomes dressed with the transmon state. Comparison to data extracted from the InAs-based device B shows similar κ at $\chi_{01} = 0\,\mathrm{MHz}$, but shows lower κ at finite χ_{01}. We conclude that the InSb qubit is too lossy and unstable to coherently control and manipulate and further improvement in fabrication or material growth has to be done. With the biggest difference with respect to the InAs device fabrication being the maximum processing temperature of 20 °C, we suspect resist residues to be responsible for the complications in the device performance.

6.5. Conclusion and outlook

In summary, we developed a semiconductor OCS gatemon using InAs and InSb proximity-induced semiconductor nanowires. Additional gates that extend over the length of the nanowire allow for the control of n_g and μ over a large range. Both device platforms demonstrate to be magnetic field compatible up to strong magnetic fields. In particular for the InAs devices the qubit showed coherent manipulation and qubit coherence could be maintained up to $B_\parallel = 0.5$ T, an order of magnitude larger than in previous nanowire transmons. The natural magnetic field compatibility of these devices set the stage for detection and manipulation of Majorana zero modes [19, 38, 48].

The linewidth of the InAs OCS gatemons allowed a more in-depth study of the suppression of charge dispersion in highly transparent JJs. We developed a model that describes the suppression of Coulomb oscillations in weak-links with near-unity transparencies. Here the scaling law of the suppression of the charge dispersion is dictated by ITLZ tunnelling between ABSs and agrees with the observed suppression rate. Independent research paralleling our own reports similar spectroscopic measurements on a full-shell gatemon with a dc transport lead [49]. The vanishing of charging effects has implications for the design of hybrid circuits incorporating ballistic JJs [7, 29, 50–53], and in particular for future gatemons [3–5, 8, 21]. The guaranteed and rapid vanishing of charge sensitivity for $\tilde{D} \to 1$ while the anharmonicity remains finite places much less stringent requirements on E_C compared to other transmon implementations, allowing for faster qubit manipulation and strongly reducing the qubit's physical footprint.

6.6. Supplement

6.6.1. Overview fabrication steps

To provide an overview of the differences between the devices, the fabrication steps are listed in Table 6.2.

Table 6.2: Fabrication flow of the devices specifying the slight differences in fabrication steps. Green highlighted cells indicate executed fabrication steps, while red cells indicate the absence of this fabrication step.

Fabrication step	Details	Device A 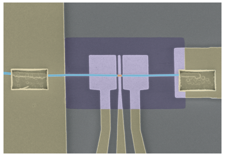	Device B 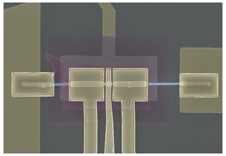	Device C 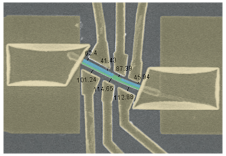	Device D, E 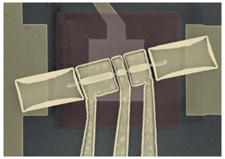
Wafer preparation	Nitric acid clean				
Superconducting components	20 nm sputtered NbTiN, shaped by RIE in SF_6/O_2	Cutter and plunger gates	Global gate	No gates	Global gate
Dicing					
Bottom dielectric		7 nm ALD HfO_x	30 nm PECVD SiN_x	🟥	30 nm PECVD SiN_x
Nanowire deposition		InAs-Al, Optical	InAs-Al, Optical	InSb-Al, SEM	InSb-Al, SEM
Al etch	Transene D wet etch	JJ and contact windows	JJ and contact windows	Predefined JJ during growth	Predefined JJ during growth
Contacts	Sputtered NbTiN, typically 150-200 nm			In intervals of 20 s	In intervals of 20 s
Top dielectric	30 nm sputtered SiN_x	🟥		🟥	
Top gates	Sputtered NbTiN, typically 150-200 nm	🟥		🟥	Using the top dielectric resist
Dicing					

References

[1] Koch, J. *et al.* Charge-insensitive qubit design derived from the Cooper pair box. *Phys. Rev. A* **76**, 042319 (2007).

[2] Place, A. P. M. *et al.* New material platform for superconducting transmon qubits with coherence times exceeding 0.3 milliseconds. *Nature Communications* **12**, 1779 (2021).

[3] de Lange, G. *et al.* Realization of Microwave Quantum Circuits Using Hybrid Superconducting-Semiconducting Nanowire Josephson Elements. *Phys. Rev. Lett.* **115**, 127002 (2015).

[4] Larsen, T. W. *et al.* Semiconductor-Nanowire-Based Superconducting Qubit. *Phys. Rev. Lett.* **115**, 127001 (2015).

[5] Kringhøj, A. *et al.* Anharmonicity of a superconducting qubit with a few-mode Josephson junction. *Phys. Rev. B* **97**, 060508 (2018).

[6] Kroll, J. G. *et al.* Magnetic field compatible circuit quantum electrodynamics with graphene Josephson junctions. *Nature Communications* **9**, 4615 (2018).

[7] Wang, J. I.-J. *et al.* Coherent control of a hybrid superconducting circuit made with graphene-based van der Waals heterostructures. *Nature Nanotechnology* **14**, 120–125 (2019).

[8] Serniak, K. *et al.* Direct Dispersive Monitoring of Charge Parity in Offset-Charge-Sensitive Transmons. *Phys. Rev. Applied* **12**, 014052 (2019).

[9] Pita-Vidal, M. *et al.* Gate-Tunable Field-Compatible Fluxonium. *Phys. Rev. Applied* **14**, 064038 (2020).

[10] Casparis, L. *et al.* Gatemon Benchmarking and Two-Qubit Operations. *Phys. Rev. Lett.* **116**, 150505 (2016).

[11] van Woerkom, D. J. *et al.* Microwave spectroscopy of spinful Andreev bound states in ballistic semiconductor Josephson junctions. *Nature Physics* **13**, 876–881 (2017).

[12] Goffman, M. F. *et al.* Conduction channels of an InAs-Al nanowire Josephson weak link. *New Journal of Physics* **19**, 092002 (2017).

[13] Spanton, E. M. *et al.* Current–phase relations of few-mode InAs nanowire Josephson junctions. *Nature Physics* **13**, 1177–1181 (2017).

[14] Zazunov, A., Shumeiko, V. S., Bratus', E. N., Lantz, J. & Wendin, G. Andreev Level Qubit. *Phys. Rev. Lett.* **90**, 087003 (2003).

[15] Chtchelkatchev, N. M. & Nazarov, Y. V. Andreev Quantum Dots for Spin Manipulation. *Phys. Rev. Lett.* **90**, 226806 (2003).

[16] Doucot, B. & Loffe, L. B. Physical implementation of protected qubits. *Reports on Progress in Physics* **75**, 072001 (2012).

[17] Larsen, T. W. *et al.* Parity-Protected Superconductor-Semiconductor Qubit. *Phys. Rev. Lett.* **125**, 056801 (2020).

[18] Imamoğlu, A. Cavity QED Based on Collective Magnetic Dipole Coupling: Spin Ensembles as Hybrid Two-Level Systems. *Phys. Rev. Lett.* **102**, 083602 (2009).

[19] Ginossar, E. & Grosfeld, E. Microwave transitions as a signature of coherent parity mixing effects in the Majorana-transmon qubit. *Nature Communications* **5**, 4772 (2014).

[20] Krogstrup, P. *et al.* Epitaxy of semiconductor–superconductor nanowires. *Nature Materials* **14**, 400–406 (2015).

[21] Luthi, F. *et al.* Evolution of Nanowire Transmon Qubits and Their Coherence in a Magnetic Field. *Phys. Rev. Lett.* **120**, 100502 (2018).

[22] Sabonis, D. *et al.* Destructive Little-Parks Effect in a Full-Shell Nanowire-Based Transmon. *Phys. Rev. Lett.* **125**, 156804 (2020).

[23] Kringhøj, A. *et al.* Andreev Modes from Phase Winding in a Full-Shell Nanowire-Based Transmon. *Phys. Rev. Lett.* **126**, 047701 (2021).

[24] Chang, W. *et al.* Hard gap in epitaxial semiconductor–superconductor nanowires. *Nature Nanotechnology* **10**, 232–236 (2015).

[25] Gazibegovic, S. *et al.* Epitaxy of advanced nanowire quantum devices. *Nature* **548**, 434–438 (2017).

[26] Mi, X. *et al.* Circuit quantum electrodynamics architecture for gate-defined quantum dots in silicon. *Applied Physics Letters* **110**, 043502 (2017).

[27] de Moor, M. W. A. *et al.* Electric field tunable superconductor-semiconductor coupling in Majorana nanowires. *New Journal of Physics* **20**, 103049 (2018).

[28] Doh, Y.-J. *et al.* Tunable Supercurrent Through Semiconductor Nanowires. *Science* **309**, 272–275 (2005).

[29] Hays, M. *et al.* Direct Microwave Measurement of Andreev-Bound-State Dynamics in a Semiconductor-Nanowire Josephson Junction. *Phys. Rev. Lett.* **121**, 047001 (2018).

[30] Schreier, J. A. *et al.* Suppressing charge noise decoherence in superconducting charge qubits. *Phys. Rev. B* **77**, 180502 (2008).

[31] Glazman, L. & Matveev, K. Resonant Josephson current through Kondo impurities in a tunnel barrier. *JETP Lett* **49**, 659 (1989).

[32] Beenakker, C. W. J. & van Houten, H. Resonant Josephson Current Through a Quantum Dot. *Koch H., Lübbig H. (eds) Single-Electron Tunneling and Mesoscopic Devices. Springer Series in Electronics and Photonics* **31** (1992).

[33] Devyatov, I. A. & Kupriyanov, M. Y. Resonant Josephson tunneling through S-I-S junctions of arbitrary size. *Journal of Experimental and Theoretical Physics* **85**, 189–194 (1997).

[34] Golubov, A. A., Kupriyanov, M. Y. & Il'ichev, E. The current-phase relation in Josephson junctions. *Rev. Mod. Phys.* **76**, 411–469 (2004).

[35] Beenakker, C. W. J. Universal limit of critical-current fluctuations in mesoscopic Josephson junctions. *Phys. Rev. Lett.* **67**, 3836–3839 (1991).

[36] Averin, D. V., Zorin, A. B. & Likharev, K. K. Bloch oscillations in small josephson junctions. *Zh. Eksp. Teor. Fiz* **88**, 692–703 (1985).

[37] Averin, D. V. Coulomb Blockade in Superconducting Quantum Point Contacts. *Phys. Rev. Lett* **82** (1999).

[38] Pikulin, D., Flensberg, K., Glazman, L. I., Houzet, M. & Lutchyn, R. M. Coulomb Blockade of a Nearly Open Majorana Island. *Phys. Rev. Lett.* **122**, 016801 (2019).

[39] Ivanov, D. A. & Feigel'man, M. V. Coulomb effects in a ballistic one-channel S-S-S device. *Physics-Uspekhi* **41**, 197–201 (1998).

[40] Bargerbos, A. *et al.* Observation of Vanishing Charge Dispersion of a Nearly Open Superconducting Island. *Phys. Rev. Lett.* **124**, 246802 (2020).

[41] Zuo, K. *et al.* Supercurrent Interference in Few-Mode Nanowire Josephson Junctions. *Phys. Rev. Lett.* **119**, 187704 (2017).

[42] Lutchyn, R., Glazman, L. & Larkin, A. Quasiparticle decay rate of Josephson charge qubit oscillations. *Phys. Rev. B* **72**, 014517 (2005).

[43] Lutchyn, R. M., Glazman, L. I. & Larkin, A. I. Kinetics of the superconducting charge qubit in the presence of a quasiparticle. *Phys. Rev. B* **74**, 064515 (2006).

[44] Martinis, J. M., Ansmann, M. & Aumentado, J. Energy Decay in Superconducting Josephson-Junction Qubits from Nonequilibrium Quasiparticle Excitations. *Phys. Rev. Lett.* **103**, 097002 (2009).

[45] Catelani, G., Schoelkopf, R. J., Devoret, M. H. & Glazman, L. I. Relaxation and frequency shifts induced by quasiparticles in superconducting qubits. *Phys. Rev. B* **84**, 064517 (2011).

[46] Catelani, G. Parity switching and decoherence by quasiparticles in single-junction transmons. *Phys. Rev. B* **89**, 094522 (2014).

[47] Kringh{oj, A. *et al.* Magnetic-Field-Compatible Superconducting Transmon Qubit. *Phys. Rev. Applied* **15**, 054001 (2021).

[48] Hassler, F., Akhmerov, A. R. & Beenakker, C. W. J. The top-transmon: a hybrid superconducting qubit for parity-protected quantum computation. *New Journal of Physics* **13**, 095004 (2011).

[49] Kringhøj, A. *et al.* Controlled dc Monitoring of a Superconducting Qubit. *Phys. Rev. Lett.* **124**, 056801 (2020).

[50] Chauvin, M. *et al.* Crossover from Josephson to Multiple Andreev Reflection Currents in Atomic Contacts. *Phys. Rev. Lett.* **99**, 067008 (2007).

[51] Bretheau, L., Girit, c. O., Pothier, H., Esteve, D. & Urbina, C. Exciting Andreev pairs in a superconducting atomic contact. *Nature* **499**, 312–315 (2013).

[52] Pekker, D., Hou, C.-Y., Manucharyan, V. E. & Demler, E. Proposal for Coherent Coupling of Majorana Zero Modes and Superconducting Qubits Using the 4π Josephson Effect. *Phys. Rev. Lett.* **111**, 107007 (2013).

[53] Tosi, L. *et al.* Spin-Orbit Splitting of Andreev States Revealed by Microwave Spectroscopy. *Phys. Rev. X* **9**, 011010 (2019).

7

Quasiparticle trapping by the orbital effect in a hybrid superconducting-semiconducting circuit

W. Uilhoorn, J. G. Kroll, A. Bargerbos, S. D. Nabi, C. K. Yang, P. Krogstrup, L. P. Kouwenhoven, A. Kou, G. de Lange

The tunneling of quasiparticles (QPs) across Josephson junctions (JJs) detrimentally affects the coherence of superconducting and charge-parity qubits, and is shown to occur more frequently in magnetic fields. Here we demonstrate the parity lifetime to survive in excess of 50 μs *in magnetic fields up to* 1 T*, utilising a semiconducting nanowire transmon to detect QP tunneling in real time. We exploit gate-tunable QP filters and find magnetic-field-enhanced parity lifetimes, consistent with increased QP trapping by the ungated nanowire due to the orbital effect. Our findings highlight the importance of QP trap engineering for building magnetic-field compatible hybrid superconducting circuits.*

7.1. Introduction

There is wide interest in understanding the dynamics of quasiparticle (QP) excitations in superconducting devices such as those used in astronomy [1], metrology [2], thermometry and refrigeration [3], superconducting quantum devices [4–6], superconducting qubits [7–13], and proposed topological qubits [14]. Despite operation at low temperatures where thermal QPs are exponentially suppressed [15], non-equilibrium QPs continue to plague these applications. In particular for superconducting quantum circuits, the tunneling of QPs may be accompanied by exchange of energy with the circuit, known as quasiparticle poisoning (QPP), and results in the loss of quantum information [7–9, 11, 14]. To prevent such poisoning, QPs can be captured away from sensitive regions of the device by engineering QP traps, which generally rely on a local reduction of the superconducting gap [7, 9, 11, 16]. Hybrid superconductor-semiconductor nanowire (NW) devices provide a novel platform to apply such gap engineering *in situ* [17], enabled by their electric-field-tunable proximity-induced energy gap [18]. Moreover, these hybrid NWs show induced superconductivity at magnetic fields strong enough where they are expected to host Majorana zero modes [19], the basis for topological qubits. In this context, a crucial outstanding question is - how does QPP develop as magnetic field increases?

Recent studies focusing on QPP in superconducting qubits have been based on real-time detection of QPP by detecting parity switching events, utilizing offset-charge sensitive (OCS) transmon qubits [8, 13] and Andreev levels [10, 12], and all performed while being heavily shielded from stray magnetic fields. To date, magnetic field studies of QP dynamics in Josephson junction (JJ) circuits consist only of time-averaged experiments performed below $B < 0.3$ T. These works demonstrated the increase in QPP due to field induced Cooper pair breaking [6, 20]. Recent developments in magnetic field compatible superconducting resonators [21] and advances in semiconducting nanowire-based (NW) JJs enabled novel semiconductor-based superconducting circuits [22–24], that operate in magnetic fields up to 1 T [25, 26]. Such devices enable the investigation of QPP in the unexplored magnetic field parameter space that is essential in topological quantum computing, where a magnetic field as strong as 1 T may be required [19].

In this letter, we study *in-situ* tunable gap engineering, and its effect on QPP at magnetic fields up to 1 T in an InAs NW JJ using an OCS transmon architecture. We utilize local gates to electrically control the superconductor-semiconductor coupling and form gate-tunable QP filters situated on either side of the JJ. When the JJ is protected by the gate-controlled QP filters, we find peaks of enhanced charge-parity lifetimes induced by the magnetic field and centered around odd multiples of $B_{\parallel} \sim 280$ mT. We attribute these enhancements to the formation of quasiparticle traps in the ungated NW segments as a result of a local suppression of the induced gap by orbital effect [27–29], efficiently trapping QPs away from the JJ. Finally we conclude that such devices can be operated at high magnetic field without being limited by QPP, paving the way for implementing proposals for novel superconducting-topological hybrid qubits [30, 31].

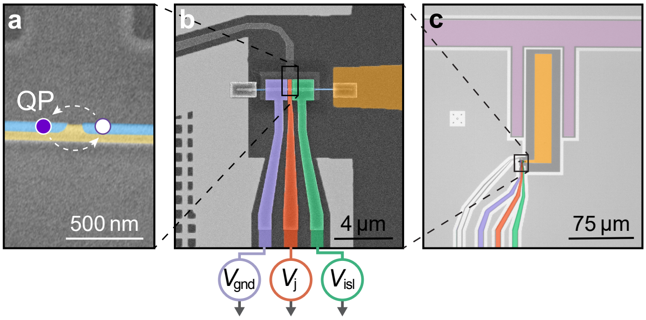

Figure 7.1: **Device overview.** **a** False-colored scanning electron micrograph of a lithographically similar device before top gate fabrication, showing the JJ created from a proximitized InAs NW (yellow) with a two-facet epitaxial Al shell (blue). The purple dot illustrates the tunneling of QP excitations across the JJ. **b** False-colored scanning electron micrograph of the NW contacted to ground at the left and to the capacitor island (orange) at the right. A gate (red) at the junction provides $E_{\mathrm{J}}\left(V_{\mathrm{j}}\right)$ tuning of the qubits frequency. Plunger gates (green, purple) at either side of the JJ control the chemical potential of the proximitized sections of the NW ($V_{\mathrm{isl}}, V_{\mathrm{gnd}}$), while also providing a tuning knob for the offset charge n_{g} (V_{isl}). **c** False-colored optical micrograph of the transmon capacitively coupled to a superconducting transmission coplanar waveguide resonator (pink).

7.2. Device design

Our device is a single-island OCS transmon dispersively coupled to a half-wave resonator, used to read out the state of the qubit [32]. We measure the exact same device as [33]. The transmon is based on a superconducting-semiconducting (SC-SM) Al-InAs NW JJ [Figure 7.1(a)] [34]. The ∼ 100 nm JJ divides the NW in two Al-proximitized InAs sections. One section is connected to a NbTiN ground plane and the other to a NbTiN island, with charging energy $E_C \sim h \times 530$ MHz [Figure 7.1(b)]. The island is capacitively coupled to a superconducting coplanar waveguide resonator for readout with $f_{\mathrm{bare}} = 5.201$ GHz and $\kappa/2\pi = 2.591$ MHz with a coupling strength of $g \sim h \times 81$ MHz [Figure 7.1(c)]. The resonator, ground plane and island are patterned with vortex pinning sites [21]. The carrier density in the semiconducting JJ and adjacent leads are tuned by several electrostatic gates through the field effect [Figure 7.1(d)]. First, we alter the Josephson coupling E_{J} by V_{j} [35], similarly to previous work in the context of SM weak link qubits [22–24]. In addition, the carrier density profile in the SC-SM parts of the leads are tuned by the wrapped plunger gates V_{isl} and V_{gnd}, enabling us to control the proximity effect in the enclosed leads [18, 29, 36]. Lastly, the offset charge n_{g} of the island is predominantly tuned by V_{isl}. We note that tuning n_{g} requires much smaller ranges in voltage (on the order of ∼ 1 mV) than the voltages required to tune the carrier density appreciably (typically requiring ∼ 1 V), providing an effectively independent tuning knob for n_{g}.

7.3. Results

7.3.1. Charge parity dependent resonator mode

We first demonstrate readout of the charge-parity P of the OCS transmon via the superconducting microwave resonator response in absence of an additional qubit drive tone [13]. The E_{J}/E_C-ratio is designed to be $E_{\mathrm{J}}/E_C \sim 14$ when the qubit's ground to

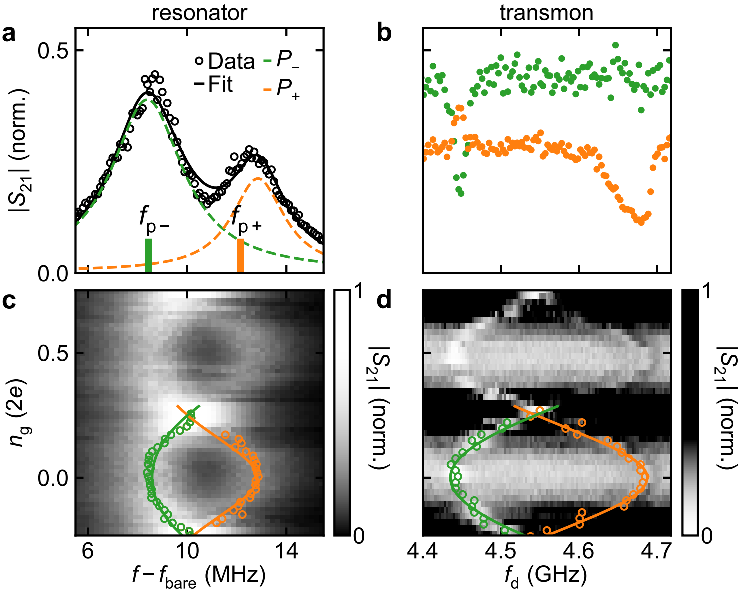

Figure 7.2: **Offset charge dependent resonator-qubit response. a** $|S_{21}|$ of the resonator coupled to an n_g dependent transmon at maximum charge dispersion. The bimodal spectrum is fitted with a double Lorentzian (solid black), and decomposed in the two parity contributions (dashed orange, green). **b** A qubit state dependent resonator shift is observed when driving the qubit by a second input tone f_d while probing the resonator response at a fixed readout frequency. At fixed readout frequency at f_{p-} (f_{p+}), a dip corresponding to the P_- (P_+) branch of the transmon is observed, with P_- (P_+) indicated in green (orange). **c** $|S_{21}|$ versus n_g, revealing the charge modulation directly in the resonator transmission and **d** in qubit spectroscopy probed at $f_p = f_{bare} + 10$ MHz. The extracted peaks (valleys) are fitted using a standard SIS transmon model resulting in $E_J = 7.214$ GHz, $E_C = 0.532$ GHz, $g_c/2\pi = 81$ MHz.

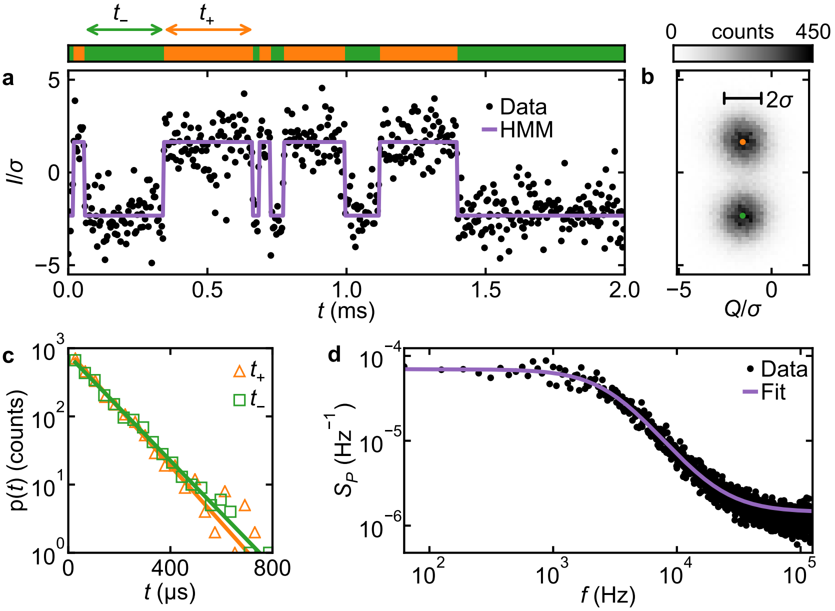

Figure 7.3: **Parity lifetime analysis** of 32 × 16 ms jump traces with $t_{\text{int}} = 4\,\mu\text{s}$. **a** (a) 2 ms snapshot of a single quadrature response in time (black) revealing a charge parity jump trace. Charge parity state assignment and the extraction of dwell times t_+ and t_- (upper panel) is done by applying a hidden Markov model (purple). **b** 2D histogram of the resonator response demonstrating the clustering into two well-separated Gaussian distributions in the IQ-plane; the charge parity states. **c** Histogram of extracted dwell times t_+ and t_-, corresponding to coherence times of $T_+ = 104 \pm 3\,\mu\text{s}$ and $T_- = 108 \pm 4\,\mu\text{s}$ respectively. **d** Average power spectrum density of the 32 independent complex jump traces (black) fitted by a Lorentzian lineshape (purple) corresponding to $T_P = 106.9 \pm 0.7\,\mu\text{s}$ and a detection fidelity of $F = 0.799 \pm 0.002$.

first excited state transition frequency $f_{\text{q}} \sim f_{\text{bare}}$, making the qubit transitions depend strongly on parity and n_{g} [Figure 7.2(b,d)] [32]. As a consequence of the strong dispersive coupling between the OCS transmon and resonator, the resonator frequency f_{res} inherits these same dependencies on P and n_{g} [Figure 7.2]. We verify this by investigating the correspondence between the P-dependent resonator frequencies, $f_{\text{res}-}$ and $f_{\text{res}+}$, and the two qubit parity branches, $f_{\text{q}-}$ and $f_{\text{q}+}$, respectively. The different magnitudes of S_{21} for $f_{\text{res}-}$ and $f_{\text{res}+}$ are only found with the TWPA activated. By matching the probe frequency $f_{\text{p}-}$ ($f_{\text{p}+}$) to $f_{\text{res}-}$ ($f_{\text{res}+}$) we demonstrate selective sensitivity to $f_{\text{q}-}$ ($f_{\text{q}+}$) in two-tone spectroscopy at maximum charge-parity separation ($n_{\text{g}} = 0$) [Figure 7.2 (a,b)]. The even and odd charge-parity branches are observed simultaneously, consistent with the transfer of one or more QPs across the JJ during each 40 ms measurement. Our cQED setup allows us to detect individual parity switching events in real time. The QPP dynamics, and its dependence on electric and magnetic field, is central to this work.

7.3.2. Direct dispersive charge parity detection

We demonstrate our ability to measure QPP in real time. By monitoring S_{21} at a fixed readout frequency, we can directly detect island-parity switching events down to $\sim$ 1 µs resolution by utilizing a near-quantum limited travelling-wave parametric amplifier [37]. To maximize signal to noise, the readout is performed at $n_\mathrm{g} = 0$ with f_p set at the local minimum in between the two parity resonances. Recording a continuous measurement of S_{21} reveals a random telegraph signal [Figure 7.3(a)] as a consequence of the switches in qubit-island parity. The histogram of S_{21} in the complex (I, Q)-plane confirms two well-separated parity states [Figure 7.3(b)], both Gaussian distributed with symmetric widths and populations [See Supplementary Information]. The histogram is built by constructing a connected time series of (I, Q)-shots of S_{21} by binning 32 × 16 ms-long time traces in $t_\mathrm{int} = 4$ µs bins. The equal parity population, as expected with the ground state charge dispersion being two orders smaller than the thermal energy, makes the two parity levels indistinguishable and hinders 'even' and 'odd' state labelling. Instead, we refer to '+' and '-' as unspecified parity labels.

To gain further insight in the poisoning dynamics, we assign a state to every (I, Q)-shot by applying a hidden Markov model (HMM) to the time evolution of (I, Q) [Figure 7.3(a)]. The extracted dwell times t_+ and t_- are found to follow an exponential probability distribution with average dwell times of $T_+ = 104 \pm 3$ µs and $T_- = 108 \pm 4$ µs [Figure 7.3(c)]. The exponential distribution indicates that the switching events result from a Poissonian process. The Poissonian temporal distribution together with the Gaussian distributed parity clusters validates the use of the HMM [See Supplementary Information]. The overlap of the dwell time distributions, both in number of counts and average dwell times, demonstrates the symmetry between the even-to-odd and odd-to-even poisoning processes. This justifies the extraction of a single parity lifetime via Fourier transform analysis [Figure 7.3(d)]; each 16 ms long jump trace is transformed to frequency space separately and subsequently averaged, revealing a power spectral density (PSD) that is well fitted by a Lorentzian [See Supplementary Information]. The typical drop off frequency corresponds to the combined average parity lifetime T_P, where $T_P = 106.9 \pm 0.7$ µs and a parity detection fidelity of $F = 0.799 \pm 0.002$ in the case of $t_\mathrm{int} = 4$ µs, where the uncertainties are extracted errors from the fit.

7.3.3. Electric and magnetic field parity lifetime enhancement

We now use the measurement of QPP dynamics to investigate the response of the device to static electromagnetic field tuning. For these measurements ten individual measurements of T_P are averaged over minute timescales to constitute $\overline{T}_P$. The associated standard deviation in $\overline{T}_P$ captures any excess variation in T_P stemming from temporal fluctuations in the QP density x^0_QP [38, 39]. First, we confirm that the observed QP dynamics result from the presence of non-equilibrium QPs, by measuring the temperature dependence of $\overline{T}_P$ [See Supplementary Information]. At the lowest temperature of $T \approx 25$ mK the extracted $x^0_\mathrm{QP} \approx 10^{-7}$, which corresponds to a thermal QP distribution with an effective temperature of $T^\mathrm{QP}_\mathrm{eff} \approx 193$ mK. These numbers are typically encountered [4, 8, 9, 16, 39], and are linked to stray radiation impacting the device due to imperfect shielding [13, 40, 41].

We take advantage of the semiconducting nature of the NW to electrostatically mod-

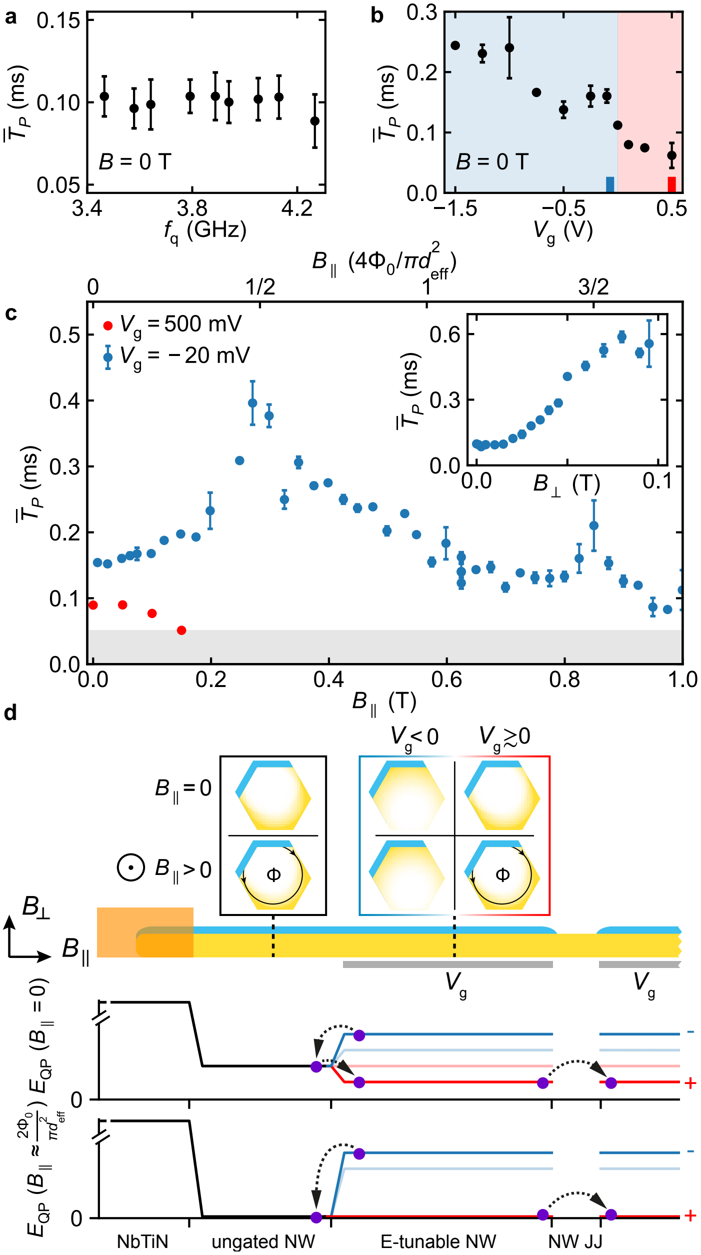

Figure 7.4: **Parity lifetime dependence. a** $\overline{T}_P$ versus f_q. **b** $\overline{T}_P$ versus V_g. **c** $\overline{T}_P$ versus $B_\parallel$ corresponding to the plunger settings marked by the ticks in *b*. $\overline{T}_P$ is not resolvable below $\overline{T}_P < 50\,\mu s$ (grey area). Inset: $\overline{T}_P$ versus $B_⊥$. **d** Schematic illustrating the charge density profile in the NW, and its dependence on V_g. The plunger gates locally alter the charge density distribution from ring-shaped for $V_g \gtrsim 0$ to charge confinement at the superconducting Al shell for $V_g < 0$. The minimal QP excitation energy E_{QP} is sketched for $B_\parallel = 0$ (upper graph) and $B_\parallel \approx \frac{2\Phi_0}{\pi d_{eff}^2}$ (bottom graph), the latter being the field required to thread an effective circular area with half a flux quantum. At this field the orbital effect suppresses the proximity-induced gap. Setting $V_g < 0$ breaks the ring-shaped electron density, nullifying the orbital effect and restoring the proximity-induced gap in the gated section. The field-dependent E_{QP} allows for *in situ* QP trap engineering, as illustrated by the purple dots.

ify the charge-carrier density in the JJ and its leads [18, 29, 36]. First we verify that f_q does not strongly influence the QP tunneling rate by varying f_q through V_j [Figure 7.4(a)]. We measure a constant $\overline{T}_P$ while changing f_q over almost 1 GHz, corresponding to a 3 mV increase in V_j. This justifies any retuning of f_q amidst a measurement series, a necessary intervention to ensure that f_q stays within a frequency range suitable for parity lifetime readout over large field ranges. We then investigate the gate dependence of $\overline{T}_P$ by varying both plunger gate voltages $V_\mathrm{g} = V_\mathrm{isl} = V_\mathrm{gnd}$ simultaneously [Figure 7.4(b)]. For $V_\mathrm{g} \gtrsim 0$ we observe a decrease in $\overline{T}_P$, while for $V_\mathrm{g} < 0$ we find $\overline{T}_P$ to rise quickly initially and more than doubles upon further decreasing V_g.

The connection between x^0_QP at the JJ and the proximity effect in the leads can be further explored by applying a magnetic field [Figure 7.4(c)]. For this we are able to operate the device as a charge parity detector up to $B_\parallel = 1$ T, where $B_\parallel$ is oriented along the NW. For $V_\mathrm{g} \gtrsim 0$ we observe a decay of $\overline{T}_P$ with $B_\parallel$ [See Supplementary Information], indicating increased x^0_QP near the JJ as associated with the closing with magnetic field of the proximity-induced gap in the gated parts of the leads. At $V_\mathrm{g} < 0$, we observe a markedly different dependence of $\overline{T}_P$. Upon increasing $B_\parallel$, $\overline{T}_P$ further rises and exhibits clear peaks at distinct values of $B_\parallel$. The transition point at $V_\mathrm{g} = 0$ V that divides these two regimes suggests that the device behaviour hinges on the energy potential landscape for QPs E_QP set by the profile of the proximity-induced gap in the gated and ungated NW sections.

In the case of $V_\mathrm{g} < 0$, $\overline{T}_P$-enhancements indicate the turn-on of magnetic field induced QP trapping away from the JJ. We observe enhancements of $\overline{T}_P$ for distinct values for $B_\parallel$. We attribute these to the orbital effect of the magnetic field, that occurs when the ring-shaped electron density in the cross-sectional area of the leads are threaded by magnetic flux, leading to the suppression of the proximity-induced gap [Figure 7.4(d)] [26, 27]. Such ring-shaped electron density profile is a manifestation of charge accumulation at the InAs NW surface for $V_\mathrm{g} \geq 0$ [29]. However, in the NW sections leading up to the JJ we can locally interrupt the accumulation by applying $V_\mathrm{g} < 0$, preventing such gap suppression. The larger-gap sections obstruct QPs trapped in the ungated regions from reaching the JJ and thus acts as QP filters [17]. The situation reverses upon setting $V_\mathrm{g} \gtrsim 0$, which activates the gap suppression and QP trapping right next to the JJ, decreasing $\overline{T}_P$ as x^0_QP increases. From the peak positions we estimate an effective diameter of $d_\mathrm{eff} = \sqrt{2\Phi_0/\pi B} \approx 69$ nm, suggesting an accumulation layer of about 13 nm based on the measured NW diameter of 95 ± 5 nm and consistent with simulations [36]. Lastly, we apply an out of plane field $B_{\perp}$ [Figure 7.4(c) inset]. We now observe an even more dramatic dramatic increase of $\overline{T}_P$ at much more moderate fields, starting from $B_{\perp} > 10$ mT. While we expect orbital effects to play a role as well for perpendicular orientation, we cannot rule out QP trapping in vortex cores induced in the NbTiN contacts [9, 16], whose presence is also evidenced by the broadening of the resonator lineshape [21]. The resonator broadening prevented exploring higher ranges for $B_{\perp} > 100$ mT.

7.4. Conclusion and Outlook

In conclusion, we have realized an OCS InAs-Al NW transmon that operates up to magnetic fields of 1 T, establishing a real-time charge-parity switching detector at strong magnetic fields. We demonstrated a more than twofold increase in charge-parity lifetime by applying a local electrostatic potential and a global magnetic field, thereby controlling the minimal QP excitation energy in the leads of the JJ. At negative gate voltages a QP filter forms at the JJ, trapping QPs away from the JJ. The orbital effect suppresses the proximity-induced gap at half integer magnetic flux threading of the nanowire, increasing the efficiency of the QP traps and yielding magnetic field dependent parity lifetime enhancements. At positive voltages and finite fields QPs are trapped at the JJ, resulting in significant drop in parity lifetime. The demonstrated increase in parity lifetime via electric and magnetic field induced *in situ* gap engineering, provides a realistic solution to QPP by non-equilibrium QPs, important for quantum computation with both topological and superconducting qubits.

Acknowledgements

We thank K. Peterson, A. Kringhøj, L. Casparis, T. Larsen, B. van Heck, D. Pikulin, T. Karzig, F. Rybakov, E. Babaev, K. Serniak, and B. Nijholt for the open and stimulating discussions, J. van Veen for depositing the NW and W. D. Oliver lab for providing a traveling wave parametric amplifier.

This work was supported by the Netherlands Organisation for Scientific Research (NWO/OCW) as part of the Frontiers of Nanoscience (NanoFront) program, Microsoft Corporation Station Q and the European Research Council.

7.5. Supplementary information

7.5.1. Validation of hidden Markov model

As discussed in the main text, the assignment of a charge parity state to a data point is done by the use of a hidden Markov model (HMM) [39]. To validate the use of a HMM to our data set, we show the two levels are normally distributed in the (I, Q) space [Figure 7.5(a)] and that the quantum jumps follow a Poisson distribution in time. Deviation from a Gaussian distribution can indicate too long averaging per data point, not only averaging out noise but also averaging out the sharp jumps. Secondly, the HMM is only applicable to Markovian processes; uncorrelated subsequent events that follow a Poissonian distribution in time. The exponential distribution shown in the main text verifies Poissonian behavior for shorter dwell times. By plotting the weighted histogram $tp(t)$, we confirm the Poissonian behavior for longer dwell times [Figure 7.5(b)]. The weighted histograms also allow us to determine the fidelity of the state assignment by comparing to the theoretical model given the extracted event rate and total number of events. We find fidelities of $F_{-} = 0.996$ and $F_{+} = 0.997$.

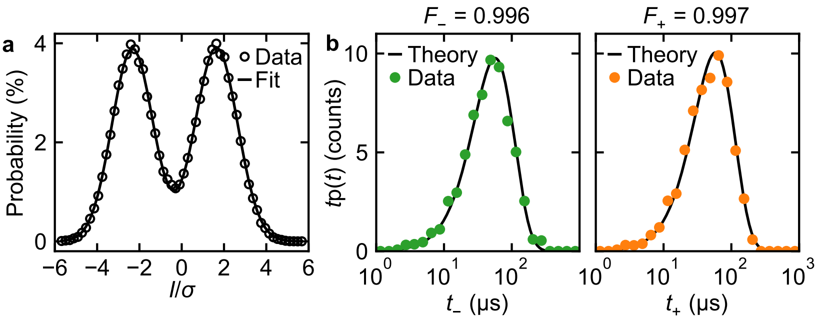

Figure 7.5: **Temporal quantum jumps distribution.** **a** histogram projected on the I-quadrature (open black dots) fitted by a double Gaussian distribution (solid black). **b** Histogram of dwell times weighted by the dwell times in the charge parity state P_- (left panel, green) and P_+ (right panel, orange), in perfect agreement with the theoretical predicted Poisson distribution (solid black). The fidelities F_- and F_+ are extracted from the deviation of the data from the theoretical prediction.

7.5.2. Parity lifetime extraction from power spectrum density

By use of the HMM we have shown symmetric transition dynamics, i.e. equal lifetimes and fidelities for the charge parity states. This allows us to extract a combined charge parity lifetime T_P with a combined detection fidelity F by fitting the averaged power spectral density (PSD). F determines the detection error probability $(1-F)/2$, an uncorrelated noise process masking the random telegraph signal (RTS). The transformation to the frequency domain is computationally beneficial, besides the SNR of the PSD can be increased while preserving high frequency information by averaging Fourier transforms of consecutive non-integrated time traces. The PSD of a RTS is described by a Lorentzian lineshape [8]:

$$S_P = F^2 \frac{4\Gamma_P}{(2\Gamma_P)^2 + (2\pi f)^2} + (1-F^2)t_{\mathrm{int}} \tag{7.1}$$

where $\Gamma_P = 1/T_P$ is the average parity jump rate, F the detection fidelity and t_{int} the integration time.

7.5.3. Temperature dependence evaluation at zero and finite magnetic field

To investigate whether the main source of QPs are of non-thermal origin we measure the temperature dependence of $\overline{T}_P$, both at $B_\parallel = 0$ mT and at $B_\parallel = 290$ mT [Figure 7.6]. $\overline{T}_P$ is determined from the Lorentzian fit of the frequency spectrum and we average 10 measurements to provide a standard deviation. We assume that the QPP rate Γ_P is proportional to the QP density x_{QP} and follow [42]. x_{QP} is taken as the QP density normalized by the density of Cooper pairs in thermal equilibrium and consists of two independent contributions:

$$x_{\mathrm{QP}} = x^0_{\mathrm{QP}} + \sqrt{\frac{2\pi k_{\mathrm{B}}T}{\Delta}} e^{-\frac{\Delta}{k_{\mathrm{B}}T}} \tag{7.2}$$

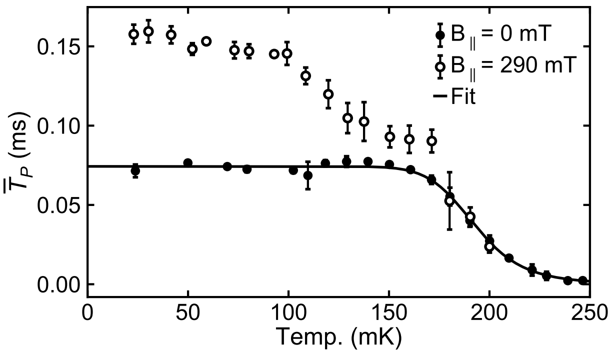

Figure 7.6: **Temperature dependence of** T_P at $B_\parallel$ = 0 mT (solid dots) and and $B_\parallel$ = 290 mT (open dots). The fit to the theoretical model shows a non-equilibrium QP to Cooper pair ratio of $x^0_{\mathrm{QP}} \approx 1 \times 10^{-7}$, equivalent to an effective temperature of $T^{\mathrm{QP}}_{\mathrm{eff}} \approx$ 193 mK.

Here the first term covers the temperature independent contribution and the second term describes the temperature dependent contribution determined by scattering and recombination processes of QPs localized near the gap edge [15]. The data is well-fitted by the model with $x^0_{\mathrm{QP}} \approx 1{\times}10^{-7}$, equivalent to an effective temperature of $T^{\mathrm{QP}}_{\mathrm{eff}} \approx$ 193 mK, and Δ = 257 ± 16 µeV. Our result is similar to previously recorded QP ratios of $x^0_{\mathrm{QP}} \approx 10^{-8}$ to 10^{-5} [4, 9, 16, 39, 42, 43]. Furthermore, Δ is consistent with DC measurements for thin aluminium films of 7 nm to 10 nm [44, 45], indicating a near-perfect proximitized superconducting gap. To gain further insight at finite magnetic field we repeated the measurement at $B_\parallel$ = 290 mT [Figure 7.6]. A similar drop off around ~190 mK shows the device is still plagued by the same source of non-equilibrium QPs. However, the cascading drop off can not be described by the theoretical model and therefore leads us to believe that the mechanism for $\overline{T}_P$-enhancement depends on temperature as well with a characteristic temperature that lies below 190 mK.

7.5.4. Additional magnetic field data

To demonstrate that the parity lifetime enhancement is a reproducible feature and is independent of the sweep direction, we repeated the measurement using different gate settings and sweep directions [Figure 7.7]. For completeness, all gate settings, readout frequency and available qubit frequency data are plotted along side. The decreasing f_{q} with $B_\parallel$ shows the necessity of retuning some parameters during a measurement run, since the readout of T_P is only possible in the range where f_{q} =3.2 GHz to 4.9 GHz. We show here both the raw data and the averaged data, where averaging only has been applied to identical gate settings. We observe an enhancement in $\overline{T}_P$ for all three runs with the maximum at $B_\parallel \simeq$ 283 mT.

Additional plunger settings are investigated to verify the difference between positive and negative V_{g} [Figure 7.8]. The magnetic field alignment at each increment is time consuming. To save time, measurements of T_P are taken by first sweeping over different gate settings before increasing $B_\parallel$. The measurement order results in a more capricious

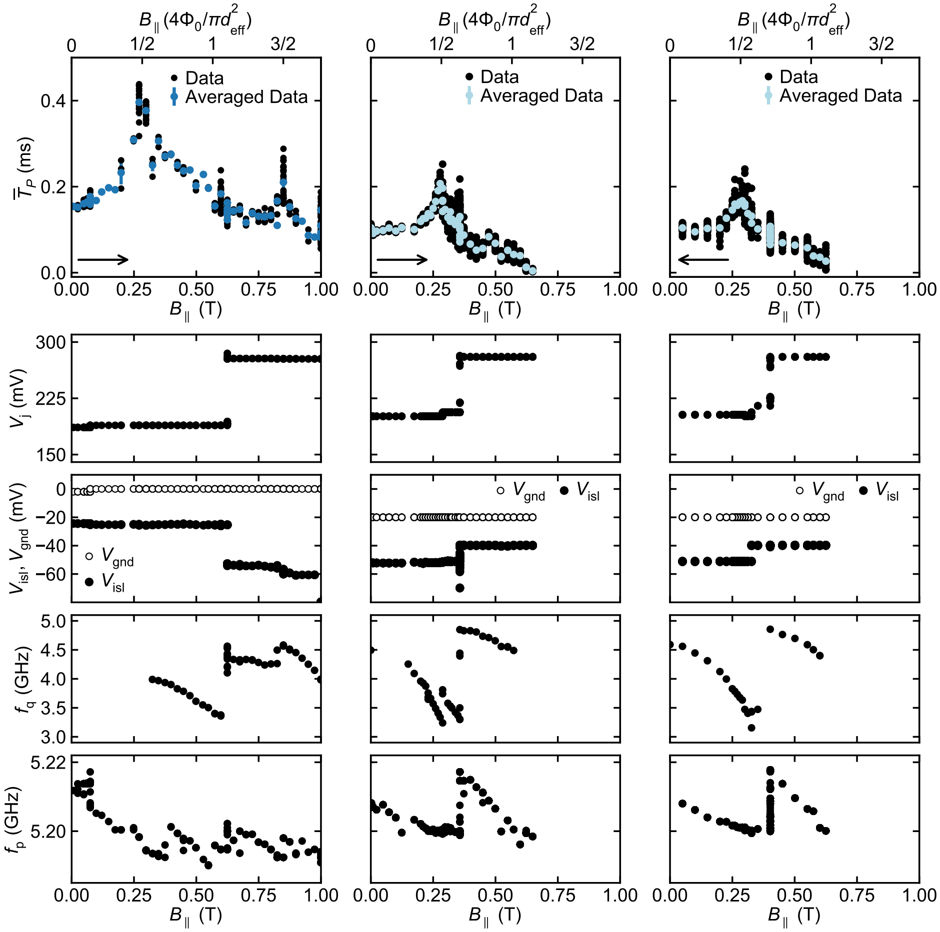

Figure 7.7: Overview of three measurement runs showing the in-plane magnetic field evolution of $\overline{T}_P$. The arrow in the bottom left corner indicates the sweep direction of the magnetic field. The corresponding gate settings V_{j}, V_{isl} and V_{gnd}, readout frequency f_{p} and qubit frequency f_{q} are plotted below. The gate settings had to be retuned within a measurement run to stay within the detection range which is limited to f_{q} =3.2 GHz to 4.9 GHz.

data set since the sweeping of gate voltages is prone to hysteresis. Around 280 mT, we observe an enhancement of $\overline{T}_P$ for all $V_\mathrm{g} < 0\,\mathrm{V}$, while we observe an impairment of $\overline{T}_P$ for $V_\mathrm{g} > 0\,\mathrm{V}$. The magnetic field value where the enhancement of $\overline{T}_P$ is observed seems identical. Contrarily, the value at which $\overline{T}_P$ dips is observed to depend on the magnitude of the positive voltage applied to the plunger gates. These observations suggest that the origin of the $\overline{T}_P$-enhancement is not located at the gated NW sections, while the phenomenon behind the $\overline{T}_P$-dips does occur at the gated NW sections.

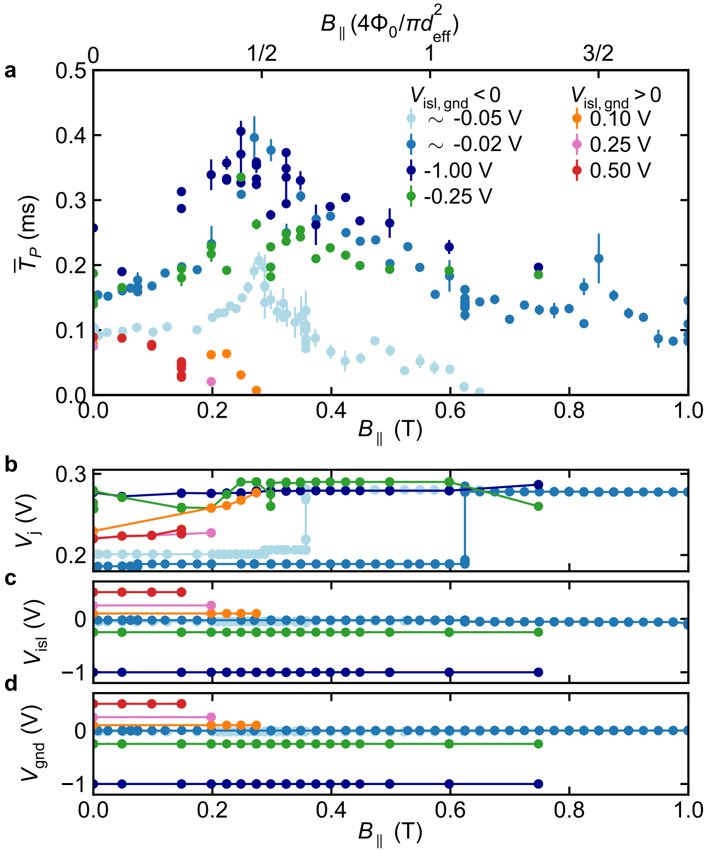

Figure 7.8: (a) $\overline{T}_P$ versus $B_{\parallel}$ for different gate settings. Corresponding (b) V_j, (c) V_{isl} and (d) V_{gnd}. Two markedly different trends have been measured, depending on the sign of the plunger gates V_{isl} and V_{gnd}. The top horizontal axis shows the magnetic flux penetration of the NW assuming $\Phi_0/2 = 283$ mT.

References

[1] Day, P. K., LeDuc, H. G., Mazin, B. A., Vayonakis, A. & Zmuidzinas, J. A broadband superconducting detector suitable for use in large arrays. *Nature* **425**, 817–821 (2003).

[2] Pekola, J. P. *et al.* Hybrid single-electron transistor as a source of quantized electric current. *Nature Physics* **4**, 120–124 (2008).

[3] Giazotto, F., Heikkilä, T. T., Luukanen, A., Savin, A. M. & Pekola, J. P. Opportunities for mesoscopics in thermometry and refrigeration: Physics and applications. *Rev. Mod. Phys.* **78**, 217–274 (2006).

[4] Aumentado, J., Keller, M. W., Martinis, J. M. & Devoret, M. H. Nonequilibrium Quasiparticles and $2e$ Periodicity in Single-Cooper-Pair Transistors. *Phys. Rev. Lett.* **92**, 066802 (2004).

[5] de Visser, P. J. *et al.* Number Fluctuations of Sparse Quasiparticles in a Superconductor. *Phys. Rev. Lett.* **106**, 167004 (2011).

[6] van Woerkom, D. J., Geresdi, A. & Kouwenhoven, L. P. One minute parity lifetime of a NbTiN Cooper-pair transistor. *Nature Physics* **11**, 547 (2015).

[7] Sun, L. *et al.* Measurements of Quasiparticle Tunneling Dynamics in a Band-Gap-Engineered Transmon Qubit. *Phys. Rev. Lett.* **108**, 230509 (2012).

[8] Ristè, D. *et al.* Millisecond charge-parity fluctuations and induced decoherence in a superconducting transmon qubit. *Nature Communications* **4**, 1913 (2013).

[9] Wang, C. *et al.* Measurement and control of quasiparticle dynamics in a superconducting qubit. *Nature Communications* **5**, 5836 (2014).

[10] Janvier, C. *et al.* Coherent manipulation of Andreev states in superconducting atomic contacts. *Science* **349**, 1199–1202 (2015).

[11] Riwar, R.-P. *et al.* Normal-metal quasiparticle traps for superconducting qubits. *Phys. Rev. B* **94**, 104516 (2016).

[12] Hays, M. *et al.* Direct Microwave Measurement of Andreev-Bound-State Dynamics in a Semiconductor-Nanowire Josephson Junction. *Phys. Rev. Lett.* **121**, 047001 (2018).

[13] Serniak, K. *et al.* Direct Dispersive Monitoring of Charge Parity in Offset-Charge-Sensitive Transmons. *Phys. Rev. Applied* **12**, 014052 (2019).

[14] Karzig, T., Cole, W. S. & Pikulin, D. I. Quasiparticle Poisoning of Majorana Qubits. *Phys. Rev. Lett.* **126**, 057702 (2021).

[15] Kaplan, S. B. *et al.* Quasiparticle and phonon lifetimes in superconductors. *Phys. Rev. B* **14**, 4854–4873 (1976).

[16] Taupin, M., Khaymovich, I. M., Meschke, M., Mel'nikov, A. S. & Pekola, J. P. Tunable quasiparticle trapping in Meissner and vortex states of mesoscopic superconductors. *Nature Communications* **7**, 10977 (2016).

[17] Ménard, G. C. *et al.* Suppressing quasiparticle poisoning with a voltage-controlled filter. *Phys. Rev. B* **100**, 165307 (2019).

[18] de Moor, M. W. A. *et al.* Electric field tunable superconductor-semiconductor coupling in Majorana nanowires. *New Journal of Physics* **20**, 103049 (2018).

[19] Lutchyn, R. M. *et al.* Majorana zero modes in superconductor–semiconductor heterostructures. *Nature Reviews Materials* **3**, 52–68 (2018).

[20] van Veen, J. *et al.* Magnetic-field-dependent quasiparticle dynamics of nanowire single-Cooper-pair transistors. *Phys. Rev. B* **98**, 174502 (2018).

[21] Kroll, J. G. *et al.* Magnetic-Field-Resilient Superconducting Coplanar-Waveguide Resonators for Hybrid Circuit Quantum Electrodynamics Experiments. *Phys. Rev. Applied* **11**, 064053 (2019).

[22] de Lange, G. *et al.* Realization of Microwave Quantum Circuits Using Hybrid Superconducting-Semiconducting Nanowire Josephson Elements. *Phys. Rev. Lett.* **115**, 127002 (2015).

[23] Larsen, T. W. *et al.* Semiconductor-Nanowire-Based Superconducting Qubit. *Phys. Rev. Lett.* **115**, 127001 (2015).

[24] Luthi, F. *et al.* Evolution of Nanowire Transmon Qubits and Their Coherence in a Magnetic Field. *Phys. Rev. Lett.* **120**, 100502 (2018).

[25] Pita-Vidal, M. *et al.* Gate-Tunable Field-Compatible Fluxonium. *Phys. Rev. Applied* **14**, 064038 (2020).

[26] Kringhøj, A. *et al.* Magnetic-Field-Compatible Superconducting Transmon Qubit. *Phys. Rev. Applied* **15**, 054001 (2021).

[27] Büttiker, M. & Klapwijk, T. M. Flux sensitivity of a piecewise normal and superconducting metal loop. *Phys. Rev. B* **33**, 5114–5117 (1986).

[28] Zuo, K. *et al.* Supercurrent Interference in Few-Mode Nanowire Josephson Junctions. *Phys. Rev. Lett.* **119**, 187704 (2017).

[29] Winkler, G. W. *et al.* Unified numerical approach to topological semiconductor-superconductor heterostructures. *Phys. Rev. B* **99**, 245408 (2019).

[30] Pekker, D., Hou, C.-Y., Manucharyan, V. E. & Demler, E. Proposal for Coherent Coupling of Majorana Zero Modes and Superconducting Qubits Using the 4π Josephson Effect. *Phys. Rev. Lett.* **111**, 107007 (2013).

[31] Ginossar, E. & Grosfeld, E. Microwave transitions as a signature of coherent parity mixing effects in the Majorana-transmon qubit. *Nature Communications* **5**, 4772 (2014).

[32] Koch, J. *et al.* Charge-insensitive qubit design derived from the Cooper pair box. *Phys. Rev. A* **76**, 042319 (2007).

[33] Bargerbos, A. *et al.* Observation of Vanishing Charge Dispersion of a Nearly Open Superconducting Island. *Phys. Rev. Lett.* **124**, 246802 (2020).

[34] Krogstrup, P. *et al.* Epitaxy of semiconductor–superconductor nanowires. *Nature Materials* **14**, 400 (2015).

[35] Doh, Y.-J. *et al.* Tunable Supercurrent Through Semiconductor Nanowires. *Science* **309**, 272–275 (2005).

[36] Antipov, A. E. *et al.* Effects of Gate-Induced Electric Fields on Semiconductor Majorana Nanowires. *Phys. Rev. X* **8**, 031041 (2018).

[37] Macklin, C. *et al.* A near–quantum-limited Josephson traveling-wave parametric amplifier. *Science* **350**, 307–310 (2015).

[38] Grünhaupt, L. *et al.* Loss Mechanisms and Quasiparticle Dynamics in Superconducting Microwave Resonators Made of Thin-Film Granular Aluminum. *Phys. Rev. Lett.* **121**, 117001 (2018).

[39] Vool, U. *et al.* Non-Poissonian Quantum Jumps of a Fluxonium Qubit due to Quasiparticle Excitations. *Phys. Rev. Lett.* **113**, 247001 (2014).

[40] Houzet, M., Serniak, K., Catelani, G., Devoret, M. H. & Glazman, L. I. Photon-Assisted Charge-Parity Jumps in a Superconducting Qubit. *Phys. Rev. Lett.* **123**, 107704 (2019).

[41] Vepsäläinen, A. P. *et al.* Impact of ionizing radiation on superconducting qubit coherence. *Nature* **584**, 551–556 (2020).

[42] Serniak, K. *et al.* Hot Nonequilibrium Quasiparticles in Transmon Qubits. *Phys. Rev. Lett.* **121**, 157701 (2018).

[43] Martinis, J. M., Ansmann, M. & Aumentado, J. Energy Decay in Superconducting Josephson-Junction Qubits from Nonequilibrium Quasiparticle Excitations. *Phys. Rev. Lett.* **103**, 097002 (2009).

[44] Chubov, P. N., Eremenko, V. V. & Pilipenko, Y. A. Dependence of the critical temperature and energy gap on the thickness of superconducting aluminum films. *JETP* **55**, 752 (1968).

[45] Court, N. A., Ferguson, A. J. & Clark, R. G. Energy gap measurement of nanostructured aluminium thin films for single Cooper-pair devices. *Superconductor Science and Technology* **21**, 015013 (2007).

8

Conclusion and outlook

This chapter summarizes per chapter the important achievements and conclusions, discusses points of improvement, proposes future experiments. Furthermore, scalability prospects are reviewed, as ultimately the scalability will determine the large-scale applicability of the devices. Currently this is an issue for all the hybrid Josephson junction-devices in this thesis. Both the graphene and semiconductor nanowire platforms are fabricated using methods that require intensive manual labour. The manual labour does not only result in long manufacturing lead times per device, but also causes larger variability between devices. With this in mind, we discuss viable roadmaps for the upscaling of graphene and nanowire-based superconducting circuits.

8.1. Magnetic-field-compatible graphene transmon

Conclusion

We demonstrated the first integration of a graphene JJ in a superconducting cavity to form a graphene-based transmon. The spectrum of the qubit exhibits the characteristic electronic properties of the underlying ballistic graphene JJ, such as Fabry–Pérot oscillations in the p-doped region, and large voltage tunability of the supercurrent which translates to a frequency bandwidth of over 4 GHz. We achieved operation of the device up to $B_\parallel = 1\,\mathrm{T}$, showing a 25% increase in transition linewidth. This opens up the study of mesoscopic effects in hybrid JJs in strong magnetic fields. The main technological achievement is our novel and selective stack transfer technique. By first isolating the intended van der Waals stack, we ensure an isolated transfer onto the superconducting circuitry, preserving the high quality factor of our superconducting resonators.

Future experiments

Future applications require higher quality graphene-based transmon devices, that allow for coherent manipulation of the qubit state. We believe that the coherence of the devices is currently limited by dielectric losses and the coupling to the topgate. In future devices this can be easily optimized in the device design and fabrication process of the electrostatic gate.

To reduce dielectric losses one could exploit a bottomgate design that uses the bottom hBN flake as gate dielectric, following the work of [1]. In case of bad adherence of hBN to the metallic surface of the bottom gate, one could also use graphite as the bottom gate by adding an extra graphite flake to the stacked heterostructure. This approach would add a fabrication step in order to electrically contact the graphite to a bondpad. Furthermore, measurements should be performed to determine the effectiveness of the shaping of the JJ as a measure to reduce the amount of dielectrics. While the etching process reduces the amount of hBN, it is unknown whether the reactive ion etch causes surface defects in the Si wafer, which could be more detrimental than the crystalline hBN.

Lastly, the gate electrode could act as a loss channel. To mitigate this, the gate could be made from superconducting material and on-chip low-pass filters can be implemented at the bondpad [2], similar to the nanowire transmon designs in later chapters.

Sufficiently phase coherent devices would enable the study of voltage sweet spots created by Fabry–Pérot oscillations, where the phase coherence is enhanced due to reduced sensitivity to charge induced dephasing when $|\partial f_{01}/\partial V_{\mathrm{g}}| \simeq 0$ [3]. The magnetic field compatibility would enable quasiparticle poisoning studies in magnetic field, similar to Chapter 7. The adaptability of the dimensions of the graphene-based junction enables studies correlating junction width and junction length with the coherence time and quasiparticle poisoning rate.

Finally, this work opens up the study of vdW-based transmons, as similar methods can be applied for other vdW materials and more complex heterostructures. The versatile electronic properties of such heterostructures provides a wide platform for novel solid-state quantum computing platforms.

Scalability

A big drawback is the scalability of encapsulated graphene Josephson junction devices. The encapsulation of exfoliated graphene with hBN enabled ballistic transport through the self-cleansing process at the hBN-graphene interface [4]. The hydrocarbon surface contamination assembles into large pockets, yielding pristine graphene areas in between the pockets. Currently the growth of hBN cannot be done in a scalable fashion, as the crystal flakes are created through mechanical exfoliation and the heterostructures are assembled via the equally manually intensive dry polymer-based pick-up and transfer technique. Even though recent growth procedures at atmospheric pressure allow for large-area single crystalline hBN flakes, up to 1 mm [5], the fabrication process still relies on these non-scalable techniques. An alternative route that does allow for wafer scale processing is by utilizing CVD-grown graphene [6]. It remains to be seen whether the integration with microwave circuitry would result in sufficient device quality for coherent devices.

8.2. Nanowire Josephson junction laser

Conclusion

We achieved strong coupling between a proximitized InAs nanowire Josephson junction and high-Q superconducting microwave CPW, resulting in a voltage-controlled on-chip microwave generator. We observe emission at the cavities fundamental frequency when biasing the Josephson junction to multiples of $V_D = hf_{\text{cavity}}/2e$ up until $n = 6$. We investigated the coherence of the Josephson radiation and its down-converted higher orders at the cavities fundamental mode, and find continuous masing up until the fourth emission peak. The fifth peak switches between a masing and a thermal state. We attribute the switches to the dissipative and incoherent process of quasiparticle tunnelling, consistent with the observed increase in the subgap conductance. We find a masing lifetime of 200 ± 10 µs, interleaved by off-time intervals that last on average 17 ± 2 µs. As a metric for device quality we extract the coherence times for each emission peak, and find increasing coherence times for every higher order down-converted emission peak. This is consistent with the notion of an additional coherent photon per stimulated emission round trip. Contrarily, at the fifth emission peak we observe a collapse of the coherence, in agreement with the switches between the masing and thermal state. Furthermore, we show that the system obeys standard laser techniques as injection locking, demonstrating a gain of almost three orders of magnitude, and injection pulling, creating a frequency comb. Lastly, we demonstrate that the system is operational in in-plane magnetic fields up to 0.3 T.

Future experiments

A d.c. powered on-chip microwave source could be of great practical value for microwave applications, as it omits the need for external microwave generators that puts a thermal load on the cryostat and also is known to inject high energetic radiation through the thermal link that it creates between base and room temperature. Therefore, this on-chip voltage-to-frequency converter could provide an alternative solution to the scalability problem of superconducting qubits. Furthermore, phase and high repetition rate stabilized mode locked lasers enable frequency comb generation used in metrology. In order to realise this, the coherence of the platform has to be improved and the generation of fast and short pulses should be demonstrated. Future experiments could therefore focus on coherence limitations, such as voltage bias noise. But could also focus on increasing the non-linearity of the system. As E_J in semiconducting nanowire JJs is smaller than what can be accomplished with conventional SIS JJs, the non-linearity can only be increased by reducing the capacitance of the transmission line resonator. An alternative approach is to enhance the electromagnetic field intensity in the cavity through coupling multiple junctions to the cavity. Here, the participation of each JJ depends on the placement with respect to the electric field anti-nodes of the cavity.

Another future experiment would be to study the response function of the system on the gate voltage controlling E_J, when connecting a fast d.c. line. To accurately determine the pulse width, without any distortion of the amplification chain, on-chip interferometric intensity auto-correlations should be performed right at the end of the cavity.

To date, experiments only have measured the emission and down-converted emission at the fundamental mode of the cavity. However, the length of the waveguide could be set to fit multiple higher order cavity modes within the accessible bandwidth of the measurement setup. This would allow for the direct measurement of higher harmonics, which benefits the general understanding of the system.

Finally, after obtaining a full understanding of the system, having studied the interplay of higher order modes, together with the advances in pulse generation and manipulation, the semiconducting Josephson laser could be integrated with a superconducting qubit, to accomplish the first on-chip d.c. controlled superconducting qubit. A different coupling experiment could be the junction-junction back-action when coupling two Josephson lasers at opposite ends of a single resonator cavity.

More thorough descriptions on discussed future experiments can be found in [7].

8.3. Magnetic-field-compatible nanowire transmon

Conclusion

We demonstrate an offset-charge-sensitive gatemon operating in magnetic fields up to 1 T, with coherent control up to 0.5 T. Besides the Josephson coupling, we also design the offset charge n_g to be voltage controlled via additional electrostatic gates that tune the electron density adjacent to the Josephson junction. We use InAs-Al nanowires as a primary platform. The ease in fabrication yields high quality devices enabling the study of the level structure and its charge dispersion via two-tone spectroscopy. We observe rapid anomalous suppression of the charge dispersion with increasing junction transparency, consistent with the suppression of Coulomb blockade by resonant tunneling through highly transmitting Andreev bound states in the Josephson junction. This suppression allows for novel approaches to built charge-insensitive qubits. Finally we developed the first gatemons based on InSb-Al nanowires. Despite the lesser device quality with respect to the InAs-Al devices, we demonstrated proof of concept even in the presence of strong magnetic fields.

Future experiments

The operation of the gatemon in the offset-charge-sensitive regime has direct consequences for the coherence of the device, as the architecture suffers from charge noise. A tradeoff that was specifically chosen in order to be sensitive to the even and odd parity branches, allowing for the detection of parity switches, as shown in Chapter 7, and to a potential anticrossing between the even and odd parity branches. The coherent coupling between the parity branches would be a signature of the presence of Majorana zero modes (MZMs) at the junction. Even though the InAs devices contain all the ingredients for MZMs, no signatures have been observed. A variety of reasons could lie at the origin. The coupling strength between the MZMs could be too small for the bandwidth of the device, $E_\mathrm{M} \lesssim 10$ MHz. The trivial parameter space is large with respect to the topological parameter space [8] and d.c. transport measurements to guide the search are missing. Or simply not enough devices have been measured to observe this feature, as d.c. transport measurements has shown that not all nanowires devices exhibit MZM signatures.

For the InSb version of the gatemon, the device quality needs to be improved significantly in order to carry out similar experiments. We attribute the inferior coherence of this material platform to the fabrication methods required for InSb-Al nanowires, which has proven to be somewhat incompatible with microwave circuits. Due to the thermal instability of the InSb-Al interface, fabrication temperatures have to be kept as low as possible and should not exceed room temperature. We hypothesize that room temperature fabrication leaves residues, as cleaning steps are not as effective at lower temperatures. Despite the pristine and etch-free junction definition and hard induced superconducting gaps, the NWs used for these devices have multiple disadvantages. The placement of the predefined JJ does not allow for accurate placement on bottom gates, and the JJ is usually placed off-centre. But foremost, the growth of the Al shell on the NW growth chip does not allow the nanowires to grow longer than 2 μm to 3 μm. A novel fabrication method deposits an epitaxial Al shell after NW deposition to the device chip by using shadow walls [9]. This method allows for long NWs ($>$ 10 μm), lithographic control of the JJ position and the simultaneous fabrication of electrical contact with existing circuitry. In particular, the elimination of fabrication steps and resist layers after the formation of the fragile semiconductor-superconductor interface promises substantial improvements.

The magnetic field compatibility of the transmon makes the system also particularly suitable for the spin-ensemble qubit design [10]. Here the quantum information is stored in an ensemble of polarized spins that are inductively coupled to a non-linear cavity-transmon system. This collective enhancement of light-matter coupling due to the number of emitters comes at the expense of of the desirable non-linearity of the coupled cavity-emitter system, which can be solved by introducing a transmon. For sufficient polarization of the spins an external magnetic fields of $\sim$ 1 T is required. Our nanowire transmon would therefore be a very suitable choice. Ultimately, the coherence time of a spin ensemble qubit is hypothesised to be much longer than conventional transmon qubits.

The observation of charge dispersion suppression through resonant tunneling opens up research possibilities of exploiting engineered quantum dot levels in the JJ to render the system charge insensitive. Through this architecture one can reduce the footprint of the shunt capacitor, at the cost of additional electrostatic gates to tune the dot. To independently tune f_{01} and the charge dispersion a split JJ could be used, where the dot-JJ quenches the charge dispersion while the other junction governs f_{01}. The ability to tune f_{01} and the charge dispersion independently enlarges the parameter space of the device, which could prove to be instrumental in the search for MZMs.

Scalability

The current fabrication method using vapor-liquid-solid grown nanowires and the subsequent manual transfer from the growth chip to the device chip are incompatible with upscaling. The manual intensity required during these processing steps causes both long manufacturing times per device and a notably wide variability in the junction properties. With the recent demonstration of InAs-based gatemons made from a two-dimensional electron gas (2DEG) [11], a scalable route for wafer-scale fabrication has been shown. The 2DEG platform eliminates both production time and reproducibility issues. However, dielectric losses still need to be improved to compete with conventional transmons. Similarly for InSb-based devices, 2DEGs could provide a solution for wafer-scale processing. To day, the first measurements of ballistic superconductivity in such InSb quantum wells have been reported [12].

An alternative approach, would be to make the aforementioned shadow-wall technique scalable by combining it with on-chip grown nanowires via selective area growth [13, 14].

The work in this chapter showcases the importance of material science, in particular the material specific fabrication processes even for seemingly closely related material systems.

8.4. Quasiparticle trapping in a nanowire transmon

Conclusion

We exploit a nanowire gatemon as a real-time charge-parity switch detector, investigating the quasiparticle poisoning rate at magnetic fields up to 1 T. Through sufficient coupling and charge dispersion the resonator inherits the charge-parity dependency of the qubit, enabling detection of the charge-parity state of the qubit's ground state directly via the resonator response. We study the parity lifetime dependence on electric and magnetic field. We show electric-field-tunable parity lifetimes when varying the applied electric field at the proximity-based nanowire segments that straddle the JJ. Our observations are consistent with the creation of QP filters or traps at the JJ, manipulating the quasiparticle density at the JJ. Depending on the plunger gate settings, we find two different trends when subjecting the device to a magnetic field parallel to the nanowire. At positive plunger gate settings, we observe the parity lifetime to decrease with magnetic field with no detectable parity lifetimes above $\sim$ 0.3 T. Contrarily, at negative plunger gate settings, we find the parity lifetime to survive up to strong magnetic fields, recording parity lifetimes of $\sim$ 0.1 ms at $B_{\|} = 1$ T, and observe parity lifetime enhancement at odd multiples of 280 mT. We attribute these observations to the orbital effect of the magnetic field, which suppresses the proximity-induced gap due to an interference effect. The interference occurs when the electron density profile in the nanowire forms a ring-like shape. This cylindric density is realised at zero and positive plunger gate voltages, but not at negative plunger voltages. Thus the negative plunger voltages protect against the suppression of the proximitiy-induced gap, while at the same time the efficiency of the QP traps at the ungated sections are enhanced through the local gap suppression. Our findings highlight the importance of QP trap engineering in superconducting circuits.

Future experiments

Further measurements can correlate the parity lifetime with the energy relaxation, to quantify the contribution of QP tunneling events on the overall energy decay.

Follow-up research could provide more insight on this specific QP trapping mechanism by studying the efficiency of the QP traps with respect to the length of the ungated nanowire section, being the length of the trap, and the length of the gated nanowire section, being the distance of the QP trap to the JJ. The dependence correlates to the QP diffusion length in the material [15].

Other experiments could study the contribution of phonon-induced Cooper pair breaking as a source for quasiparticle generation. Measurements performed in superconducting microwave circuitry have shown the negative effect of phonons in the substrate on the quasiparticle density [16, 17]. To mitigate phonon-induced Cooper pair breaking, one can down-convert the phonon energy to values below the pair breaking threshold by adding a lower-gap superconductor, one can reduce the phonon density by reducing the volume of the substrate, and one can integrate phononic-shield membranes as substrates. The techniques have proven themselves in superconducting microwave circuits, but comparative measurements and application in superconducting qubits are still outstanding. The offset-charge-sensitive transmon would be an ideal detector for such experiments.

Besides QPP switching events, switching of the Josephson coupling has been observed in the vast majority of the parameter space, where E_J was observed to switch between two E_J values. The switching of E_J results in either three of four distinguishable states in the I, Q-plane. Three separable states are observed when f_{01} moves out of the measurable range for one E_J, causing no sufficient dispersive shift on the resonator. In this case there are two states in the I, Q-plane corresponding to the even and odd parity states belonging to one E_J, and another distribution corresponding to the other E_J where both parity states overlap. Four separable states are observed when f_{01} lies within the bandwidth of our QPP detector for both E_J-values. We attribute the switching of E_J to the occupation of an Andreev bound state by a QP. A hidden Markov model could provide insight in the dynamics of this process.

References

[1] Wang, J. I.-J. *et al.* Coherent control of a hybrid superconducting circuit made with graphene-based van der Waals heterostructures. *Nature Nanotechnology* **14**, 120–125 (2019).

[2] Mi, X. *et al.* Circuit quantum electrodynamics architecture for gate-defined quantum dots in silicon. *Applied Physics Letters* **110**, 043502 (2017).

[3] Luthi, F. *et al.* Evolution of Nanowire Transmon Qubits and Their Coherence in a Magnetic Field. *Phys. Rev. Lett.* **120**, 100502 (2018).

[4] Kretinin, A. V. *et al.* Electronic Properties of Graphene Encapsulated with Different Two-Dimensional Atomic Crystals. *Nano Letters* **14**, 3270–3276 (2014). PMID: 24844319.

[5] Liu, S. *et al.* Large-Scale Growth of High-Quality Hexagonal Boron Nitride Crystals at Atmospheric Pressure from an Fe–Cr Flux. *Crystal Growth & Design* **17**, 4932–4935 (2017).

[6] Calado, V. E. *et al.* Ballistic transport in graphene grown by chemical vapor deposition. *Applied Physics Letters* **104**, 023103 (2014).

[7] Splitthoff, L. J. Non-linear quantum circuits based on gate-tunable josephson junctions (2020). First year proposal, University of Technology Delft, The Netherlands.

[8] Winkler, G. W. *et al.* Unified numerical approach to topological semiconductor-superconductor heterostructures. *Phys. Rev. B* **99**, 245408 (2019).

[9] Borsoi, F. *et al.* Single-shot fabrication of semiconducting-superconducting nanowire devices (2020). ArXiv:2009.06219v1.

[10] Imamoğlu, A. Cavity QED Based on Collective Magnetic Dipole Coupling: Spin Ensembles as Hybrid Two-Level Systems. *Phys. Rev. Lett.* **102**, 083602 (2009).

[11] Casparis, L. *et al.* Superconducting gatemon qubit based on a proximitized two-dimensional electron gas. *Nature Nanotechnology* **13**, 915–919 (2018).

[12] Ke, C. T. *et al.* Ballistic superconductivity and tunable π–junctions in InSb quantum wells. *Nature Communications* **10**, 3764 (2019).

[13] Vaitiekenas, S. *et al.* Selective-Area-Grown Semiconductor-Superconductor Hybrids: A Basis for Topological Networks. *Phys. Rev. Lett.* **121**, 147701 (2018).

[14] Aseev, P. *et al.* Ballistic InSb Nanowires and Networks via Metal-Sown Selective Area Growth. *Nano Letters* **19**, 9102–9111 (2019).

[15] Riwar, R.-P. *et al.* Normal-metal quasiparticle traps for superconducting qubits. *Phys. Rev. B* **94**, 104516 (2016).

[16] Karatsu, K. *et al.* Mitigation of cosmic ray effect on microwave kinetic inductance detector arrays. *Applied Physics Letters* **114**, 032601 (2019).

[17] Henriques, F. *et al.* Phonon traps reduce the quasiparticle density in superconducting circuits. *Applied Physics Letters* **115**, 212601 (2019).

Acknowledgements

Feeling gratitude and not expressing it
is like wrapping a present and not giving it.

William Arthur Ward

The work presented in this dissertation has been a team effort, for which I would like to acknowledge both the direct contributions of my colleagues, but also the indirect contributions in the form of support and encouragement. I have had the fortune to work alongside amazing people who helped me grow as a scientific researcher but also helped me grow on a personal level. It excites me to express my gratitude towards all of you. I hope this tribute will make you smile, just like I am smiling by thinking back of all the good times. And I hope that with my words I can warm your hearts, just like how my heart radiates with gratitude when writing them. I feel honoured and grateful for all the experiences that my PhD provided.

Thank you, **Leo**, for giving me the opportunity to work in such a state-of-the-art lab with such great people. You created a safe learning environment to develop myself and take personal responsibility of my own career, while providing both a critical view as well as mental support. Your leadership style radiates trust, and your expertise, ambition and ability to engage people are inspirational. I hope to find the courage to ask more about your experiences once you won't be my promotor anymore. My Kouwenhoven lab career started with my master thesis project under the supervision of **Maja**, motivating me to continue for a PhD. I want to thank you for teaching me all the practical skills; cleanroom work, cryogenics, measurement techniques and the importance of gate valves(!). But even more so I want to thank you for your tremendous support especially in battling imposters syndrome. I would summarize your supervision style as tough love, a combination that I am very grateful for because it challenged me while providing me with the love to help me rise to the occasions. **Srijit**, thank you for sharing your expertise and enthusiasm about graphene with me. I absolutely did not enjoy the exfoliating process, but I enjoyed the research and that you were my teacher. **Gijs**, thank you for your supervision, for all the comfortable discussions and teaching me so much more about time domain measurements and general Andreev bound state physics. I enjoyed working together a lot and I am grateful for your help with scientific writing. **Angela**, thank you for your guidance, it has been a great pleasure to be part of the topo-cQED group under your supervision. I admire your expertise and leading skills, with which you truly lead by example. With your ambition you empower the group, always focusing on challenging but realistic goals and at the same time keeping an eye on the well being of all individuals.

Equally forming and important were my dear fellow PhD'ers, who provided support, relieve of stress and a safe and harmonious environment. I am extremely grateful to call many of you my friends, and I loved sharing our common passion for physics through critical and illuminating discussions. But as you all might have noticed, I loved sharing the love for life and connection with all of you even more. I remember the moment when I asked my two paranymphs very fondly. I feel honoured to have you both by my side during my defence (in whatever form it may be during covid-19 times), representing how you both have been by my side during my PhD. You both made life in the lab, and outside, so much fun. **James**, I want to thank you for being an incredible lab partner. In particular I want to thank you for calling out when I disappear when I get overwhelmed, and supporting me to overcome my fears in those moments. I treasure all the goofiness you bring to lighten up every situation. And I am proud of what we achieved when we did not have a daily supervisor for a while. I feel like that was our most effective time, apart from one particular hung-over Sunday afternoon in the clean room. **Arno**, I could not have wished for a more wonderful successor as a lab partner. Your background in simulations, patience and eye for detail made you an invaluable lab partner. However, your dry humour is your biggest asset, with which you made me laugh to the point of choking on my drink on numerous occasions. Thank you for all the amazing ”business” trips and for the ginger, but not so much for the salt and the Sarsaparilla.

Damaz, we worked together during our masters, and basically did our PhDs side by side in different subgroups in the Kouwenhoven lab. I learned so much about spin-orbit coupling, coding and discussing papers from you. I really appreciate you, your rational thinking and your thirst for discussion. But mostly, thanks for being my buddy in crime on all our adventures. Let’s have many more! **Francesco** and **Kian**, you two completed the original Majominions. It was so much fun working with both of you and learning together. I’m happy to see you both excel in your PhDs. **Tim**, **Danish**, being your supervisor taught me a lot. I hope it was as enjoyable for you as it was for me. Thank you for having the patience with me to grow as a supervisor. Of all the people I taught some skills you learned the fastest, **Marta**. It always seems you have more hours in a day than others, please share your secret with me. Thanks for all your energy you bring to the lab, you are both the smartest and the funniest girl I know. **Jouri**, you were only part of the cQED subgroup for a little while, but luckily you were part of my whole PhD time. Thanks for teaching me some dc measurement tricks, sharing InSb fabrication recipes, and for all the good times at the tropological island. But mostly, thanks for always being there for me, for letting me crash at your place when needed and for inviting me to be part of your home office with **Anastasia**. **Vukan**, I am happy you found your place in the Kouwenhoven lab. I think it is wonderful how open you communicate, it make me like you instantly. **Lukas S.**, **Lukas G.** and **Jaap**, unfortunately we all didn’t get to work together much, but I hope I still get the chance after I send my thesis to the printer. With you guys I feel confident the subgroup will continue to flourish.

Apart from the people that were part of my subgroup, also my other colleagues from the Kouwenhoven lab had a big contribution to my work life and my development as a scientist. **Michiel**, **Alex** and **Fokko**, thank you for helping me find confidence in myself. Through your support I was able to acknowledge and appreciate my own growth and abilities. Maybe the Friday drinks also helped with that every now and then. **Jasper** and **Daniël**, thanks for rehearsing presentations for March meetings, and equally thanks for the delicious pancakes. **Chris M.**, thanks for not rehearsing presentations (due to the covid-19 pandemic), but Risk was way more fun anyway. **Di**, I'll never forget when we got to go to Station Q. **Nikolai**, thanks for all the enjoyable times at the tropological island. I enjoyed being part of such a big lab, where so much was happening. **Jakob**, **Önder**, **Daniel S.**, **Hao**, **Arjan**, **Jie**, **Sebastien**, **Dominique**, **Avradeep**, **Ting**, **Greg**, **Filip**, **Jiyin**, **Stijn**, **Michael**, **Guan**, **Nicoló**, **Luca**, **Vanessa**, **Alberto**, **Nick**, **Lin**, **Chris P.**, **Qing**, **David van D.**, **Arjen**, thanks for the amazingly motivating, fun and friendly atmosphere in Topo.

I feel grateful to feel so at home when walking down the hallways of QuTech, and that definitely is due to all the wonderful colleagues. Thanks for all the good times, at work, at summer barbeques and at Qutech Uitjes. Especially, **Kenneth**, my favourite Zouk teacher, thanks for your friendship and support. **Chris D.**, **Alessandro**, **Florian** and **Thijs**, thanks for the help in understanding transmons. Thanks to all of those who made QuTech such a great place to work, in particular **Adriaan**, **Nandini**, **Ramiro**, **Stephan**, **Jelmer**, **Udit**, **Anne-Marije**, **Guoji**, **Bas**, **Victoria**, **Heera**, **Josh**. And similarly, thanks to all the colleagues from the Microsoft lab, in particular **Chung Kai**, **David van W.**, **Marina**, **Alexandra**, **Amrita**, **Bernard**, **Kevin**, **John**, **Philippe**, **Wolfgang**.

During my PhD I had the pleasure to collaborate closely with different research groups. The most intense collaboration was with the lab of **Charlie Marcus**, I enjoyed getting to know you better and I always felt so welcome on our visits. **Karl**, thank you for setting up this collaboration. It was a lot of fun and very valuable collaboration, for that I thank the whole team: **Anders**, **Lucas**, **Thorvald**, **Robert**, **Oscar** and **Marina**. From the Erik Bakkers group I thank **Sasa**, **Roy** and **Ghada**, for showing me your lab, for teaching me about the growth process and especially for supplying and depositing many wires for us. , **Elham**, thanks for sharing your spreading your never ending positivity and incredible work ethics. **Peter Krogstrup**, thank you for supplying the highest quality InAs nanowires. **Kenji** and **Takashi**, thank you for growing the boron nitride crystals. I feel also very grateful for the simulations and discussions to interpret data all the way from Microsoft Station Q in Santa Barbara, in particular **Dmitry** and **Torsten**. Similarly, **Filipp Rybakov** and **Egor Babaev**, I would like to thank you for your interest and input in investigating any effect due to Abrikosov vortices in our structures.

I joined QuTech when I was in my bachelor, when the research division was still QT. Over the years I have had the pleasure to see QuTech grow bigger, a very exciting process to be part of. I want to thank the **leadership of QuTech** for making this happen while preserving the intimate atmosphere. In particular, **Michael** and **Csilla**, thank you for taking care of the Topo research group so well. A huge thanks to all the support staff at QuTech and Kavli Nanolab. The amount of work all of you take away for us is incredible and I feel very fortunate that I could always rely on you. I felt all of you went the extra mile to take care of issues I ran into, and always with a smile. **Jenny**, **Simone**, thank you for taking care of all the administrative parts. You made my least favourite part so easy. **Olaf**, **Jason**, **Matt**, **Nico**, **Siebe**, **Jelle**, **Remco**, **Mark**, **Roy**, **Raymond Sr.**, **Raymond Jr.**, **Marijn**, **Jack** and the others from **DEMO**, without all of you taking care of the fridges, PCBs, batteries, gyrators, brackets, measurement modules, noise issues and more, all this research would not have been possible. I truly never experienced an issue that you did not know how to fix. Similarly, a special thanks to the Kavli Nanolab cleanroom staff, **Anja**, **Arnold**, **Charles**, **Eugene**, **Ewan**, **Frank**, **Hozanna**, **Marc**, **Marco**, **Marco** and **Pauline**. I feel so spoiled having had you to rely on that the clean room with all its highly specialized instruments were in the best shape possible.

I always enjoyed working in the clean room a lot. Especially because it was a place to get in touch with people outside my own research group. I thoroughly enjoyed learning about other peoples projects during down times. Thanks to all of you, **Nodar**, **Moritz**, **Rob**, **Felix**, **Nikos**, **Jelmer**, **Udit**, **Christine**, **Iman**, **Simon**, **Richard**, **Yildiz** and many more, who made these hours so enjoyable. **Gaurab**, thank you for teaching me how to contact graphene. I never imagined that waiting to align my sample for an overnight e-beam write would become a life changing moment. There I met you, **Claus**. You gave me the courage to be comfortable with my own emotions, even when they do not align with my ratio. With that you made my life so much richer, for this I will be forever grateful.

Lastly I would like to thank those who I do not have a work related connection with. I am grateful for the invaluable support and I could not wish for better friends. I want to thank **Caspar** for teaching me the skill of studying when my fear of failure prevented me from doing so. **Victor**, thank you for being my study buddy during our studies, and for continuing to cheer for me throughout my PhD, even at times where I struggled to combine it with my social life. Thank you for your amazing friendship. **Oleksiy**, thank you for making me feel confident as a scientist and for convincing me that all the questions I asked you during our master program were smart. **Chris**, thank you for giving me that external push in confidence to pursue a PhD.

Thank you **Julia** and **Elena**, for being amazing flat mates and providing me with a home where I could study but also fully wind down. I would not have endured the corona times without your wonderful company, Elena. Thanks to my friends from high school, **Jet**, **Eva**, **Marius**, **Wessel**, **Robert-Jan**, **Tim**, **Chris** and in particular **Marij** and **Ron**, I am so grateful we have stayed in touch over the years. **Linda** and **Tina**, thank you for making Delft about more than work. Yoga and cinnamon buns haven proven to be essential ingredients to accomplishing my PhD. Tina, I have so much admiration for your perseverance, I have no doubt your promotion will follow soon! **Justin**, thanks for your support, unfortunately from afar. I'm so curious to see your start-up taking off, good luck!

Vanuit het diepste van mijn hart wil ik graag mijn familie bedanken voor jullie onvoorwaardelijke liefde en steun. Ik wil jullie bedanken voor de interesse die jullie tonen, zelfs als het niet jullie eigen interesse is. Dankjulliewel Papa (**Pieter**) en Mama (**Willy**), voor een geweldige opvoeding waarin ik vrij was mijn eigen interesses te ontwikkelen en na te jagen, waarbij ik altijd gewapend was met jullie vertrouwen in mij. Dankjulliewel Opa (**Ferdinand**) en Oma (**Gabriëlla**), mijn tweede thuis, voor jullie onvermoeibare aanmoediging. Jullie zijn het gouden randje van mijn leven. **Anne**, niet alleen de allerbeste zus maar ook mijn vriendin, en **Henrik** bedankt dat jullie deur altijd voor me open staat en bedankt voor alle steun specifiek tijdens de laatste loodjes. Ik kijk uit naar het moment dat we alledrie doctor zijn!

Curriculum Vitæ

Willemijntje Uilhoorn

22-03-1990 Born in Naarden, The Netherlands.

Education

2002–2008 Secondary School
Sint Vituscollege, Bussum, The Netherlands

2008–201 Bachelor of Science, Applied Physics
Delft University of Technology, Delft, The Netherlands
Thesis: Magnetic field dependent decoherence of a NV center
Supervisor: Prof.dr.ir. R. Hanson

2014 Internship
Bragg Institute, Australian Nuclear Science and Technology Organisation, Lucas Heights, Australia
Thesis: Enhanced magnetism in field-cooled $[Ni_{80}Fe_{20}/Mn]_3$ multilayers studied using polarized neutron reflectometry
Supervisor: Dr. S. Callori

2013–2015 Master of Science, Applied Physics
Delft University of Technology, Delft, The Netherlands
Thesis: Microwave frequency measurements of Al/AlO$_x$ SQUIDs
Supervisor: Prof.dr.ir. L. P. Kouwernhoven

2015–2021 PhD. Physics
Delft University of Technology, Delft, The Netherlands
Thesis: Hybrid Josephson junction-based quantum devices in magnetic field
Promotor: Prof.dr.ir. L. P. Kouwenhoven
Promotor: Prof.dr. L. DiCarlo

List of Publications

7. **W. Uilhoorn**, J. G. Kroll, A. Bargerbos, S. D. Nabi, C. K. Yang, L. P. Kouwenhoven, A. Kou, G. de Lange, *Quasiparticle trapping by the orbital effect in a hybrid superconducting-semiconducting circuit*, submitted.

6. **W. Uilhoorn**, J. G. Kroll, D. de Jong, D. J. van Woerkom, P. Krogstrup, L. P. Kouwenhoven, M. C. Cassidy, *A semiconductor nanowire Josephson laser*, in preparation.

5. A. Kringhøj, T. W. Larsen, O. Erlandsson, **W. Uilhoorn**, J. G. Kroll, M. Hesselberg, R. P. G. McNeil, P. Krogstrup, L. Casparis, C. M. Marcus, K. D. Petersson, *Magnetic-field-compatible superconducting transmon qubit*, Physical Review Applied **15**, 054001 (2021).

4. A. Bargerbos, **W. Uilhoorn**, B. van Heck, C. K. Yang, P. Krogstrup, L. P. Kouwenhoven, G. de Lange, A. Kou, *Observation of vanishing charge dispersion of a nearly open superconducting island*, Physical Review Letters **124**, 246802 (2020).

3. J. G. Kroll, F. Borsoi, K. L. van der Enden, **W. Uilhoorn**, D. de Jong, M. Quintero-Peréz, D. J. van Woerkom, A. Bruno, S. R. Plissard, D. Car, E. P. A. M. Bakkers, M. C. Cassiy, L. P. Kouwenhoven, *Magnetic field resilient superconducting coplanar waveguide resonators for hybrid cQED experiments*, Physical Review Applied **11**, 064053 (2019).

2. J. G. Kroll, **W. Uilhoorn**, K. L. van der Enden, D. de Jong, K. Watanabe, T. Taniguchi, S. Goswami, M. C. Cassidy, L. P. Kouwenhoven, *Magnetic field compatible circuit quantum electrodynamics with graphene Josephson junctions*, Nature Communications **9**, 4615 (2018).

1. **W. Uilhoorn**, S. J. Callori, D.L. Cortie, H.-C. Su, Y. Khaydukov, K.-W. Lin, F. Klose, *Enhanced magnetism in field-cooled* $[Ni_{80}Fe_{20}/Mn]_3$ *multilayers studied using polarized neutron reflectometry*, Journal of Physics: Conference Series **711** 012005 (2016).